Intéractions fluide-structure : du battement du drapeau à la nage des poissons

Zhanle Yu

CENTRALE MARSEILLE

École Doctorale : Sciences pour l'ingénieur: Mécanique, Physique, Micro et Nanoélectronique (ED353)

Institut de Recherche sur les Phénomènes Hors Équilibre

THÈSE DE DOCTORAT

pour obtenir le grade de

DOCTEUR de l'ÉCOLE CENTRALE de MARSEILLE

Discipline : Mécanique et Physique des Fluides

Fluid-structure interactions: from the flapping flag to the swimming fish

par

YU Zhanle

Directeur de thèse : Christophe ELOY

Soutenue le 29 Janvier 2016

devant le jury composé de :

Sébastien Michelin	PR, Ecole Polytechnique, Palaiseau	Rapporteur
Christophe Josserand	DR CNRS, Institut d'Alembert, Paris	Rapporteur
Fabien Candelier	MCF HDR, AMU, Marseille	Examinateur
Carlo Cossu	DR CNRS, IMFT, Toulouse	Examinateur
Christophe Eloy	PR, Centrale Marseille	Directeur

Acknowledgment

Foremost, I would like to express my sincere gratitude to my advisor Prof. Christophe Eloy. Thank you for your continuous support in my Ph.D study in the past three years. Thank you for your encouragement, patience and guidance throughout my Ph.D thesis. Your wisdom, suggestions and immense knowledge have greatly contributed to the thesis and helped me round off the PhD research successfully. Your erudition, sagaciousness, and hard working have clearly defined an outstanding scientist that I would strive a life-time to become.

Besides my advisor, I would like to thank the rest of my thesis committee: Prof. Sébastien Michelin, CNRS Res. Dir. Christophe Josserand, CNRS Res. Dir. Carlo Cossu and Associate Prof. Fabien Candelier, for their encouragement, insightful comments and questions.

A special thanks to my family. Words cannot express how grateful I am to my mother and father for all of the sacrifices that you've made on my behalf. Thank you for giving me life and raising me. Thank you for all your love. Without you, I can not imagine how can I finish the Ph.D research successfully, you are always my heroes.

I would like to thank my fellows and friends: Jun Chen, Florine Paraz, Hongliang Zhong, and Wei Zhu. Thank you for your helps in daily life, and I really enjoy the discussions with you.

Finally, I gratefully acknowledge the financial support from China Scholarship Council (N. 201204490206).

Resumé

Introduction

Les interactions fluide-structure sont des phénomènes très répandus dans la nature, l'industrie et la vie quotidienne. Elles peuvent être observées dans de nombreux domaines industriels, notamment l'industrie aéronautique (ailes, turbomachines, aéroacoustique), la production/transmission d'électricité (turbines à vapeur/vent/gaz, échangeurs de chaleur, réacteurs nucléaires, lignes électriques), le génie civil (bâtiments hauts et allongés, ponts suspendus, pompes, vannes) et la technologie sous-marine (câbles de remorquage, *risers* transportant le pétrole). Ces interactions fluide-structure peuvent également se rencontrer dans la nature : interactions plante-vent, nage des poissons ou vol des oiseaux ou des insectes. Parmi les applications de la vie quotidienne, on peut aussi citer, par exemple, la clarinette, le ronflement, et les pages d'un livre dans le vent. Certaines de ces interactions fluide-structure peuvent provoquer des vibrations destructrices (le *flutter* d'une aile d'avion, la vibration des pales de turbines, etc.) ou une catastrophe (le pont de Tacoma en 1940) alors que d'autres s'avèrent utiles (production d'électricité, nage des poissons, etc.).

Dans cette thèse, nous nous concentrons sur deux problèmes d'interaction fluide-structure : le battement du drapeau et la nage des poissons. Ces deux problèmes peuvent être considérés comme l'interaction d'une plaque flexible avec un écoulement à grand nombre de Reynolds. Suivant le rapport d'aspect de la plaque flexible, deux modèles sont généralement utilisés pour modéliser l'écoulement et les forces hydro ou aérodynamique : la théorie du corps élancé (*slender-body theory*) [46] proposée par Lighthill en 1960 lorsque le corps est élancé dans le sens de l'écoulement ou la théorie bidimensionnelle d'une aile instationnaire [77] lorsque le corps est de grande dimension dans la direction perpendiculaire à l'écoulement.

Après avoir décrit l'écoulement autour d'un corps allongé dans le cadre de la théorie des écoulements potentiels, Lighthill [46] a établi que l'écoulement autour de chaque section est équivalent, à l'ordre dominant, à celui autour d'un cylindre infini de même section et de même vitesse. En introduisant le concept de masse ajouté, la théorie du corps élancé de Lighthill [46] donne une formule très simple pour calculer le force par unité de longueur exercée sur un corps allongé par le fluide environnant.

De façon similaire, la théorie d'écoulement potentiel peut être utilisée dans le cadre de la théorie 2D d'une aile instationnaire [77]. En exprimant la déformation du corps comme une somme de polynômes de Chebyshev, la solution de l'équation de Laplace peut être trouvée [40] et ainsi calculer le champ de pression, la portance et le moment exercés sur l'aile.

Pour une plaque mince de rapport d'aspect quelconque, on peut utiliser une approche plus générale, toujours dans le cadre de la théorie des écoulements potentiels. Il s'agit de l'intégrale de la surface portante qui permet de décrire l'écoulement autour d'un corps de géométrie arbitraire. Considérons un système de coordonnées cartésiennes $(OXYZ)$ et un écoulement uniforme, incompressible et irrotationnel d'un fluide parfait avec la densité ρ. La vitesse de l'écoulement U est dans le direction des X positifs. Une surface flexible se déplace avec la pulsation Ω autour du plan de référence $Z = 0$ (Fig. 1). Le déplacement de la surface $h(X, T)$ est supposé suffisamment faible pour que deux hypothèses puissent être

faites : la surface et le sillage peuvent être représentés par leurs projections respectives, S et Σ, dans le plan de référence $Z = 0$; le mouvement de la surface peut être considéré comme une perturbation périodique asymptotiquement petite par rapport à l'écoulement incident.

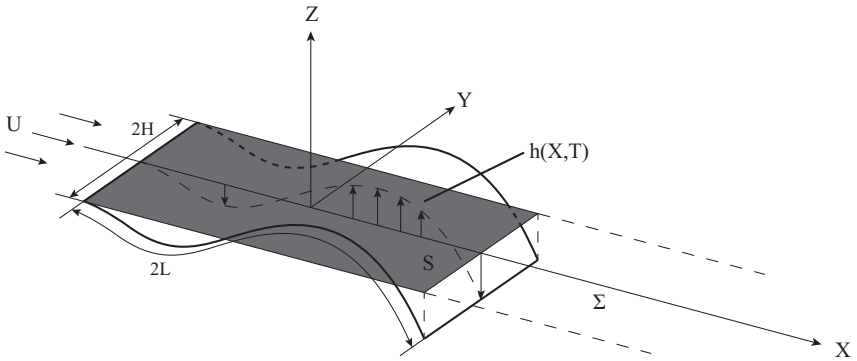

Figure 1 – Schéma du problème de la surface portante.

L'écoulement autour de la surface est gouverné par l'équation de Laplace à trois dimensions avec une condition aux limites de Neumann,

$$\Delta\Phi(P) = 0, \quad \text{avec} \quad \partial_z\Phi(M_0) = \mathrm{W}(M_0), \tag{1}$$

où Φ est le potentiel de vitesse, P un point dans le domaine de l'écoulement, M_0 un point sur la surface, W la perturbation de vitesse induite par le déplacement $h(X, T)$. En introduisant la notation complexe $e^{i\Omega T}$ pour les quantités instationnaires, nous avons

$$\mathrm{W}(M_0) = (i\Omega + U\partial_x)h(M_0). \tag{2}$$

La solution de l'équation de Laplace peut être trouvée grâce à sa fonction de Green [53]. En utilisant la condition aux limites de Neumann, nous obtenons

$$\mathrm{W}(M_0) = \fint_{S+\Sigma} [\Phi](M)F(M, M_0)\mathrm{d}S_M, \tag{3}$$

avec

$$F(M, M_0) = \frac{1}{4\pi|MM_0|^3}. \tag{4}$$

ici, la croix présente sur le symbole d'intégration signifie que nous prenons la partie finie de l'intégrale au sens d'Hadamard [33], M représente un point sur la surface et le sillage, $F(M, M_0)$ est un noyau singulier.

Une fois que le saut de potentiel $[\Phi]$ satisfaisant à Eq. (3) est trouvé, nous pouvons obtenir le saut de pression sur la surface en appliquant l'équation de Bernoulli instationnaire linéarisé :

$$[P](M_0) = -\rho(i\Omega + U\partial_x)[\phi](M_0). \tag{5}$$

Toutefois, à cause de la singularité du noyau $F(|MM_0|)$, il n'y a pas de méthode simple pour inverser l'équation de la surface portante. Dans le chapitre 2, nous allons examiner comment inverser cette équation intégrale en utilisant une méthode numérique appelée "méthode des panneaux" (*vortex panel method*). Dans le chapitre 3, nous allons voir comment l'équation de la surface portante peut être résolue analytiquement en considérant la limite asymptotique des petits rapports d'aspect.

Modèle numérique

Dans cette section, nous allons faire un résumé de chapitre 2 dans lequel l'équation intégrale de la surface portante est résolue numériquement et les résultats numériques obtenus sont comparés avec les résultats théoriques.

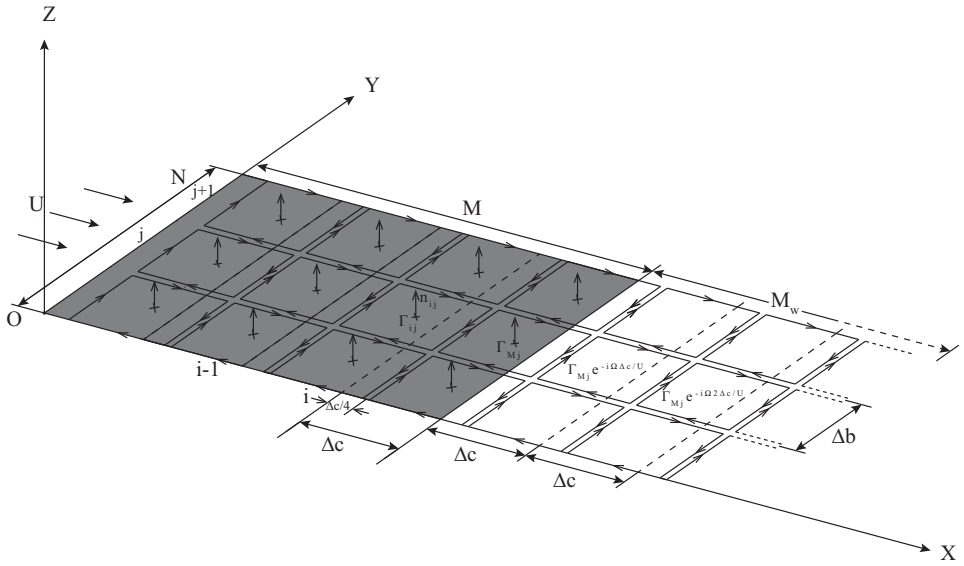

Figure 2 – Le maillage utlisé pour la méthode des panneaux à pulsation fixée.

Considérons le problème de surface portante introduit dans la section précédente (voir Fig. 1). La surface est définie par la fonction harmonique $Z = h(X,Y)e^{i\Omega T}$. Pour réduire le temps de calcul, on propose une méthode de panneaux à fréquence fixée : la couche limite sur la surface et le sillage derrière sont placés dans le plan de référence (voir Fig. 2) ; pour que le saut de pression soit nul dans le sillage et au bord de fuite, la circulation de chaque panneau dans le sillage est définie comme

$$\Gamma_{i,j,T} = \Gamma_{M,j}e^{i\Omega(T-(i-M)\Delta c/U)}, \quad M+1 \le i \le M_{\mathrm{w}}, \quad 1 \le j \le N, \tag{6}$$

ici, l'indice ij indique la position d'un vortex ou un point de collocation. L'objectif de la méthode de panneaux est de satisfaire la condition d'imperméabilité aux points de collocation. Cette condition peut être écrite

$$\mathbf{V}_b \cdot \mathbf{e}_Z + \mathbf{V}_{\mathrm{w}} \cdot \mathbf{e}_Z - \frac{\partial h}{\partial X} U e^{i\Omega T} + \mathbf{V}_B \cdot \mathbf{n}_{k,T} = 0, \quad k = 1, 2, \cdots, M \times N, \tag{7}$$

dans cette écriture, l'indice séquentiel k indique la position d'un point de collocation, $\mathbf{V}_b$, $\mathbf{V}_{\mathrm{w}}$, $\mathbf{V}_B$ sont les vitesses induites respectivement par les vortex sur la surface, les vortex dans le sillage et le mouvement de la surface. L'équation (7) peut être reformulée pour faire apparaître un système linéaire

$$M_a \mathbf{\Gamma} = \mathbf{R}, \tag{8}$$

ici, M_a est la matrice d'influence dont les éléments sont définis à partir de la loi de Bio-Savart et la condition (6), $\mathbf{\Gamma}$ le vecteur contenant les circulations inconnues des vortex de panneaux sur la surface, $\mathbf{R}$ le vecteur dont les éléments représentent la vitesse de perturbation induite par le mouvement de la surface.

Après avoir résolu numériquement l'équation (8), nous obtenons le vecteur $\mathbf{\Gamma}$ duquel la distribution de saut de pression peut être déduite à partir de la relation de Bernoulli instationnaire dans sa version discrète

$$\Delta p_{ij} = \rho \left(U \frac{\Gamma_{i,j} - \Gamma_{i-1,j}}{\Delta c_{ij}} + i\Omega \Gamma_{ij} \right). \tag{9}$$

L'avantage de considérer un mouvement harmonique est que l'inversion du système linéaire (8) ne doit être effectué qu'une fois. Afin de valider le code qui a été développé, nous considérons une surface rectangulaire fixée au bord d'attaque et libre au bord de fuite. Le déplacement est prescrit comme un mode naturel d'une poutre dans le vide.

Les résultats numériques sont tout d'abord comparés à la théorie du corps élancé en choisissant une surface de rapport d'aspect petit, $A = 0.1$, et une fréquence réduite $k = \Omega L/U = 0.5$. Dans la Fig. 3, un très bon accord entre les résultats numériques et théoriques est trouvé. D'autres calculs ont été effectués dans la limite des petits rapports d'aspect (cf. chapitre 2) afin de valider la pertinence de la méthode numérique et de s'assurer que le code ne contient pas d'erreurs.

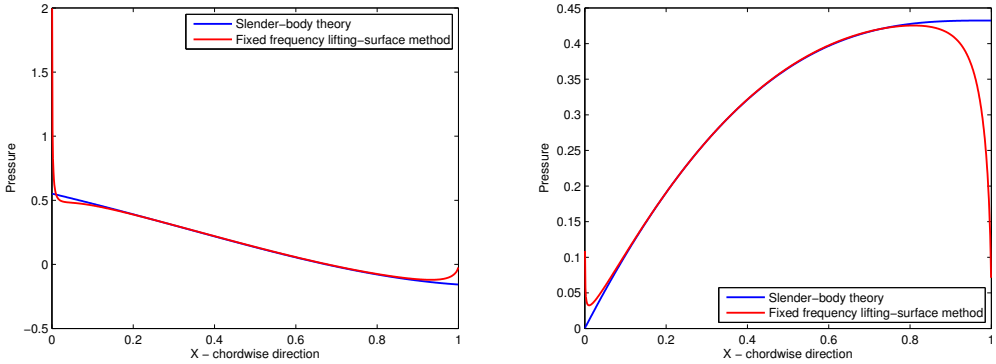

Figure 3 – Parties réelles et imaginaires du saut de pression en fonction de la coordonnée longitudinale x (adimensionnée), pour $A = 0.1$, $k = 0.5$ et le premier mode naturel de poutre.

Des études similaires ont été faites pour une surface de grand rapport d'aspect, $A = 10$, et les résultats numériques obtenus ont été comparé aux résultats théoriques donnés par la théorie 2D d'une aile oscillante [77]. Dans cette limite, nous trouvons aussi un très bon accord (Fig. 4), et les autres études au chapitre 2 valident aussi cette conclusion. Puisque la méthode donne les résultats plus précis, ils serons utilisés comme la référence pour les études prochaines concernant des surfaces de rapport d'aspect intermédiaire.

Modèle théorique

Dans cette section, nous allons faire un résumé du chapitre 3. L'équation intégrale de la surface portante sera d'abord résolue analytiquement en appliquant la méthode des raccordements de développements asymptotiques (*Matched Asymptotic Expansion* ou MAE) dans la limite des petits rapports d'aspect.

Considérons le problème présenté précédemment (voir Fig. 1). Après introduction de variables adimensionnées et la reformulation de l'éq. (3), nous obtenons

$$\mathrm{w}(x,y) = \frac{A}{4\pi} \fint_{-1}^{1} I(x,\epsilon) \mathrm{d}\eta, \quad \text{avec} \quad I(x,\epsilon) = \fint_{-l^*_{LE}(\eta)}^{\infty} \frac{[\phi](\xi,\eta)}{[(x-\xi)^2 + \epsilon^2]^{3/2}} \mathrm{d}\xi, \tag{10}$$

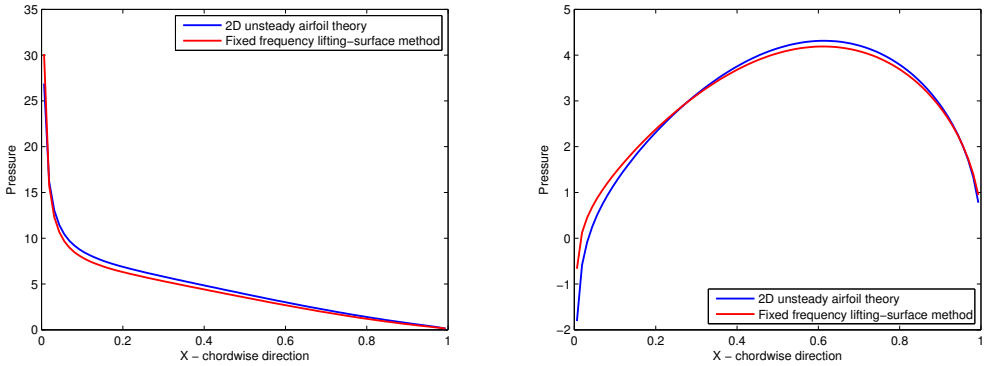

Figure 4 – Parties réelles et imaginaires du saut de pression en fonction de x, pour $A = 10$, $k = 0.5$ et le premier mode naturel de poutre.

avec $\epsilon = A(\eta - y)$, $A =$ envergure/allongement $\ll 1$, (x, y) représentent les coordonnées d'un point sur la surface, (ξ, η) un point sur la surface ou dans son sillage, $\xi = -l^*_{LE}$ le bord d'attaque local, w le downwash adimensionné (c'est-à-dire la vitesse induite par le déplacement de la plaque) et $[\phi]$ le saut de potentiel de vitesse adimensionné.

Nous introduisons ensuite une longueur intermédiaire δ [23, 31, 37] telle que $\epsilon \ll \delta \ll 1$ et séparons l'intégrale en deux parties : l'intervalle intérieur $|x - \xi| \leq \delta$ et l'intervalle extérieur $|x - \xi| > \delta$. En utilisant la définition de la partie finie de l'intégrale d'Hadamard et en négligeant les termes en ϵ^2/δ^2, nous obtenons une série de Puiseux

$$\begin{aligned} I(x,\epsilon) =& \frac{I_{-2}[\phi](x,\eta)}{\epsilon^2} \\ &+ I_0 \partial_x^2[\phi](x,\eta) + \oint^{\infty}_{-l^*_{LE}(\eta)} \frac{[\phi](\xi,\eta)}{|x-\xi|^3} \mathrm{d}\xi \\ &+ \epsilon^2 \left(I_2 \partial_x^4[\phi](x,\eta) - \oint^{\infty}_{-l^*_{LE}(\eta)} \frac{3[\phi](\xi,\eta)}{2|x-\xi|^5} \mathrm{d}\xi \right) + \cdots \end{aligned} \tag{11}$$

avec

$$I_{-2} = 2, \qquad I_0 = -1 - \ln\frac{|\epsilon|}{2}, \qquad I_2 = \frac{5}{48} - \frac{\ln 2}{8} + \frac{\ln|\epsilon|}{8}. \tag{12}$$

Maintenant, $[\phi]$ est décomposé comme une série

$$[\phi](x,y) = [\phi_0](x,y) + [\phi_1](x,y) + [\phi_2](x,y) + \cdots \tag{13}$$

dans laquelle $[\phi_i](x, y)$ est asymptotiquement petit par rapport au terme précédent. En considérant les éqs. (10), (11) et (13), et en classant les termes en fonction de leurs ordres, nous obtenons une système triangulaire dont l'équation dominante peut être résolue par la formule d'inversion de Carleman [28, 35]. Si nous considérons un cas simple où le downwash ne dépend que de x, le saut de potentiel dominant est

$$[\phi_0](x,y) = -2A\mathrm{w}(x)\sqrt{h^{*2} - y^2}. \tag{14}$$

L'application de la relation de Bernoulli instationnaire donne la distribution du saut de pression. Si nous faisons sa moyenne le long de l'envergure locale, nous obtenons la portance adimensionnée par unité de longueur à l'ordre 0

$$f_0(x) = (i\omega + \partial_x)(A\pi h^{*2}(x)\mathrm{w}(x)). \tag{15}$$

Nous pouvons voir que ce résultat est équivalent à la théorie du corps élancé. Mais, l'avantage de cette méthode est que nous pouvons obtenir toutes les corrections à partir du système triangulaire. La correction de portance à l'ordre 1 est alors donnée par

$$f_1(x) = \left(i\omega + \frac{\partial}{\partial x}\right)\left\{\frac{\pi A^3 h^{*4}}{4}\left[\left(\ln\frac{4}{Ah^*} - \frac{3}{4}\right)\mathrm{w}''(x) + \oint_{-1}^{\infty}\frac{\mathrm{w}(\xi)}{|x-\xi|^3}\mathrm{d}\xi\right]\right\}. \tag{16}$$

Cette formule permet de calculer la portance (ou le saut de pression) de façon plus précise que la théorie du corps élancé, surtout pour des surfaces de rapport d'aspect intermédiaire. Pour valider ces résultats théoriques, nous étudions une surface rectangulaire de rapport d'aspect $A = 0.3$. Cette surface se déforme selon le premier mode naturel de poutre à la fréquence réduite $k = 0.5$. La portance par unité de longueur est tracée en fonction de x sur la Fig. 5.

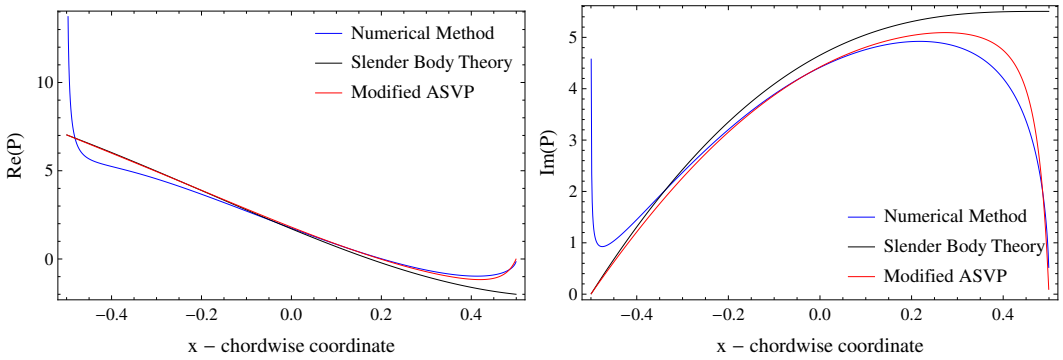

Figure 5 – Parties réelles et imaginaires de portance par unité de longueur, $A = 0.3$, $k = 0.5$, la mode première naturelle de poutre.

Nous pouvons voir que les résultats (la courbe rouge dans Fig. 5) donnés par notre modèle sont plus précis que ceux de la théorie du corps élancé. D'autres comparaisons, présentées au chapitre 3, valident aussi cette conclusion.

Inspirés par cette méthode théorique, nous proposons une autre méthode analytique plus simple. Nous nous concentrons sur une surface rectangulaire (voir Fig. 1). En formulant ce problème en termes de potentiel d'accélération $[\psi]$, nous obtenons une équation d'intégral similaire à l'éq. (10). En utilisant une série de Taylor pour estimer $[\psi]$ et en appliquant la définition de la partie finie de l'intégral, nous avons

$$\begin{aligned} I(x,\epsilon) =& \frac{1}{\epsilon^2}\left(\frac{x - l_{LE}^*}{[(x-l_{LE}^*)^2+\epsilon^2]^{1/2}} + \frac{l_{TE}^* - x}{[(l_{TE}^*-x)^2+\epsilon^2]^{1/2}}\right)[\psi](x,\eta) \\ &+ \left(\frac{1}{[(x-l_{LE}^*)^2+\epsilon^2]^{1/2}} - \frac{1}{[(l_{TE}^*-x)^2+\epsilon^2]^{1/2}}\right)\partial_x[\psi](x,\eta) + \cdots \end{aligned} \tag{17}$$

En comparant avec l'éq. (11), nous pouvons voir que le coefficient du premier terme dans (17) n'est plus constant, alors que I_{-2} est constant dans (11). Si nous introduisons une série asymptotique pour le saut du potentiel d'accélération, nous obtenons uns système triangulaire dont l'équation dominante n'est plus du type de l'équation de Carleman. Par une technique d'approximation simple, la formule d'inversion de Carleman peut être encore appliquée et nous obtenons une expression nouvelle de la portance dominante par unité de longueur

$$F_0^a(X) = \rho\frac{2\pi H^2}{b^*}D(W(X)), \qquad \text{avec} \qquad D = i\Omega + U\partial_X \tag{18}$$

dans laquelle

$$b^* = 1 + \frac{[(l^*_{TE} - x)^2 + A^2/4]^{1/2}}{l^*_{TE} - x}, \tag{19}$$

Pour valider ce résultat, nous comparons au problème vu ci-dessus. La portance par unité de longueur est tracée sur la Fig. 6.

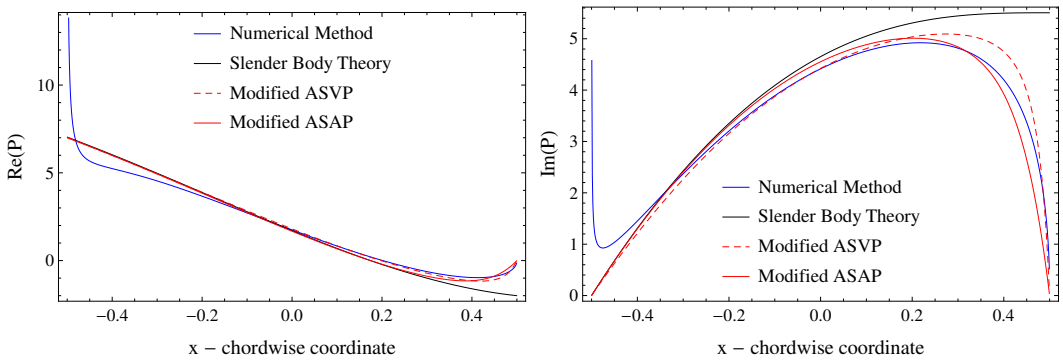

Figure 6 – Parties réelles et imaginaires de portance par unité de longueur, $A = 0.3$, $k = 0.5$, la mode première naturelle de poutre.

Nous pouvons voir que la portance (courbe rouge) donné par (18) est quasiment identique à celle obtenue précédemment par (16) (courbe rouge discontinue). Mais l'avantage de l'expression (18) est qu'elle est beaucoup plus simple et satisfait la condition de Kutta en l'ordre 0. Cela signifie que la portance (pression) donnée par (18) est plus physique, surtout pour des surfaces de rapports d'aspect intermédiaires. C'est l'expression (18) que nous allons utiliser dans le reste de la thèse pour calculer la force exercée sur un corps flexible en mouvement dans un fluide.

Battement du drapeau

Dans cette section, nous allons faire un résumé en français du chapitre 4. Nous étudions le battement du drapeau en utilisant le modèle théorique de fluide proposé au chapitre précédent. Considérons une plaque rectangulaire dans le système de coordonnées cartésiennes $(OXYZ)$. La géométrie de la plaque est décrite par le rapport d'aspect $A = H/L$ (H soit la envergure et L l'allongement). Le bord d'attaque est fixé sur l'axe Y, alors que le bord de fuite est libre. La plaque est immergée dans un écoulement homogène, incompressible, irrotationnel à l'extérieur de la couche limite et du sillage. L'écoulement est dans la direction des X positifs (Fig. 7). Il s'agit d'un problème de modèle d'interaction fluide-structure [27, 32, 56, 57].

L'équation de poutre d'Euler-Bernoulli linéarisée permet de décrire la dynamique de la plaque, avec une charge externe due au saut de pression à travers la plaque. Ainsi, nous obtenons l'équation linéarisée du mouvement de la plaque flexible sous forme adimensionnée

$$\frac{\partial^2 z}{\partial t^2} + \frac{1}{U^{*2}} \frac{\partial^4 z}{\partial x^4} - M^* \langle \Delta p \rangle_y = 0, \tag{20}$$

dans laquelle $\langle \Delta p \rangle_y$ est la moyenne le long de y de la différence de pression adimensionnée, U^* la vitesse réduite et M^* la masse réduite.

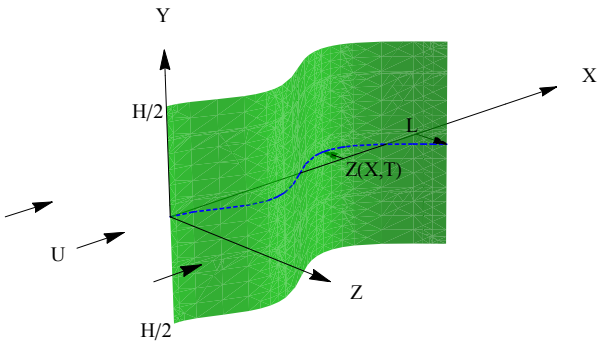

Figure 7 – Schématique d'une plaque avec la 2D deflection $Z(X,T)$ immergée dans un écoulement avec le vitesse U.

Avec l'hypothèse d'écoulement potentiel, il est facile de voir que (20) est linéaire par rapport à z. La deflection de la plaque peut alors être exprimée par une série de Galerkin

$$z(x,t) = \sum_{n=1}^{N} a_n z_n(x) e^{i\omega t}, \tag{21}$$

ici, N est un nombre entier (troncature), z_n sont les fonctions propres de poutre dans le vide satisfaisant les conditions limites: encastrée au bord d'attaque et libre au bord de fuite [56, 57]. En multipliant (20) par z_m et en utilisant les propriétés d'orthogonalité des fonctions propres, (20) devient un problème aux valeurs propres

$$\det(\mathcal{M}(\omega)) = 0, \text{ avec } \mathcal{M}(\omega) = -\omega^2 \mathcal{I} + \frac{1}{U^{*2}} \mathcal{I}^* - M^* \mathcal{P}, \tag{22}$$

dans lequel $\mathcal{I}$ est la matrice identité de taille $N \times N$, $\mathcal{I}^*$ la matrice diagonale avec k_n^4 dans l'ordre croissant sur la diagonale principale, et les éléments de matrice carrée $\mathcal{P}$ sont donnés par

$$\mathcal{P}_{m,n} = z_m \otimes p_n, \tag{23}$$

dans lequel p_n est le saut de pression correspondant à la deflection z_n. Une fois que les solutions de l'équation de solvabilité (22) sont trouvés, nous obtenons la fréquence et le taux de croissance de chaque mode de battement.

Avec le modèle de fluide proposé (éq. 18), nous avons étudié l'effet du rapport d'aspect (Fig. 8) et de la masse réduite (Fig. 9) sur la vitesse critique d'apparition du battement. Il apparaît que le modèle proposé donne des résultats plus précis que la théorie du corps élancé. En effet, la vitesse critique obtenue avec le modèle proposé est plus précise quand le rapport d'aspect est modéré ($0.2 < A < 0.7$) : on peut observer un bon accord entre les croix et la courbe rouge dans la Fig. 8. Dans la Fig. 9, nous pouvons voir un bon accord pour le cas $A = 0.2$, même si pour le rapport d'aspect $A = 0.9$ les résultat obtenus sont moins bons, mais restent raisonnables pour de petites masses adimensionnées. Ces deux figures et les

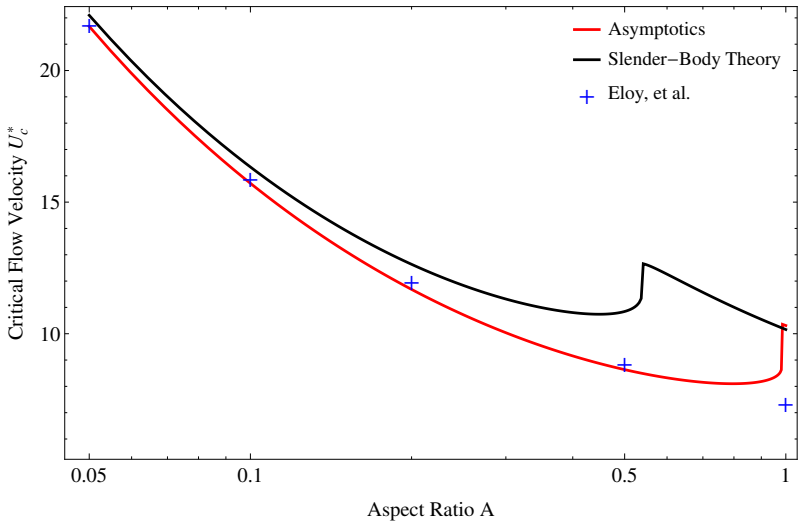

Figure 8 – Vitesse critique de l'écoulement en fonction du rapport d'aspect A pour une plaque de masse réduite $M^* = 1$. Les croix sont les résultats d'Eloy et al. [27]. Les courbes noire et rouge sont les résultats obtenus respectivement avec la théorie du corps élancé et le modèle proposé.

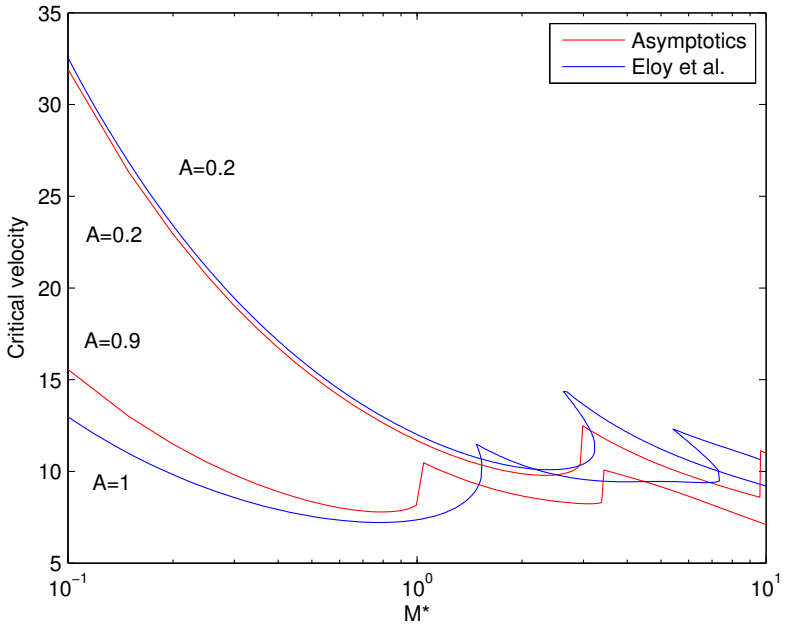

Figure 9 – Vitesse critique de l'écoulement en fonction de la masse réduite pour différents rapports d'aspect. La courbe rouge correspond aux résultats obtenus avec le modèle proposé alors que la courbe bleue correspond aux résultats d'Eloy et al. [27].

résultats du chapitre 4 valident l'applicabilité du modèle proposé dans l'analyse d'instabilité du drapeau.

La nage des poissons

Dans cette section, nous utilisons le modèle proposé pour faire des analyses qualitatives sur la morphologie des poissons. L'équation (18) permet, en effet, d'exprimer la force hydrodynamique sur un corps déformable d'envergure variable, et peut donc d'appliquer à la nage ondulatoire utilisée par une majorité de poissons.

En suivant la méthode introduite par Lighthill [46], nous pouvons calculer la poussée moyenne produite par un mouvement

$$\overline{F_T} = -\int_0^L m_a(x)\frac{\partial}{\partial x}\left(\frac{2}{b_m^*}\right)\overline{\frac{\partial h}{\partial t}V(x,t)}\mathrm{d}x - \frac{1}{2}m_a(L)\overline{V^2(L,t)}. \tag{24}$$

avec L la longueur du poisson, D son envergure (hauteur), $m_a(x)$ sa masse ajoutée, $h(x,t)$ sa déflection et $V(x,t) = \mathcal{D}h(x,t)$ le downwash. La poussée obtenue par Lighthill [46] est la limite de cette expression pour un rapport d'aspect nul. D'après cette expression, nous voyons que la poussée dépend du mouvement proche du bord de fuite (alors que seul celui du bord de fuite intervient dans la théorie Lighthill). L'efficacité de la nage des poissons est définie par l'efficacité de Froude

$$\eta_F = \frac{\overline{F}_T U}{\overline{P}} = \frac{\overline{P} - \frac{1}{2}m_a(L)\overline{V^2(L,t)}U}{\overline{P}}. \tag{25}$$

dans laquelle $\overline{P}$ est la puissance mécanique nécessaire au poisson, qui est aussi déterminé par le premier terme de (24).

Supposons que la déflection latérale du poisson puisse être écrite sous la forme

$$h(x,t) = f(x)\cos(\omega t - \frac{x}{c}). \tag{26}$$

En appliquant (24) et en faisant quelques approximations, nous obtenons l'efficacité

$$\eta_F = 1 - \frac{1}{2}\left(1 - \frac{U}{c\omega}\right)\frac{3d(L)}{3d(L) - Dd'(L)}. \tag{27}$$

dans laquelle d est l'envergure locale de poisson. Cette expression est plus générale que l'efficacité obtenue par Lighthill [46], dans le sens où elle tient compte du rapport d'aspect fini. Si nous nous concentrons sur des poissons "anguilliformes", l'efficacité est donnée par

$$\eta_F = 1 - \frac{1}{2}\left(1 - \frac{U}{c\omega}\right)\frac{64}{64 - A^2}. \tag{28}$$

Puisque cette expression est une fonction décroissante de A, l'efficacité maximale est obtenue en $A = 0$. Cela expliquerait peut-être pourquoi le rapport d'aspect de ce type de poisson est toujours petit. Mais une étude plus approfondie est nécessaire pour conclure, les travaux de ce chapitre 5 étant toujours en cours.

Contents

Chapter 1

Introduction

1.1 Some fluid-structure interaction problems

Fluid-structure interaction is a very common phenomenon in nature, industry, and daily life. It can be experienced in numerous industrial fields, including the aerospace industry (wings or airfoils, turbomachinery, acoustics), power generation/transmission (wind, gas, steam turbines, heat exchanger tubes, nuclear reactors, power transmission lines), civil engineering (tall slender buildings, suspension bridges, pumps, valves) and undersea technology (marine tow cables, pipes conveying oils). It appears broadly in nature, such as the interaction between a tree/leaves and wind, fish swimming, and bird/insect flying. In daily life, for example clarinet reeds, snoring, and a book clapping in the wind, there also exist the fluid-structure interactions. Some can cause destructive vibrations (wing flutter, vibration of turbine blades, etc) or a catastrophe (Tacoma narrows bridge in 1940). Others give useful motions (energy harvesting, fish swimming, etc).

Physically, fluid-structure interaction problems involve the interaction between some movable or deformable structure with an internal or surrounding fluid flow. The fluid exerts forces on the structure, hence causing deformation or displacement of structure. This deformation/displacement, however, changes the boundary conditions of the flow at the same time. If the structure motions play a minor role on the flow, we can treat the flow as steady. It corresponds to the weakly-coupled fluid-structure interaction problems ('steady flow' case in Fig. 1.1). Otherwise, problems should be modeled as fully-coupled fluid-structure inter-

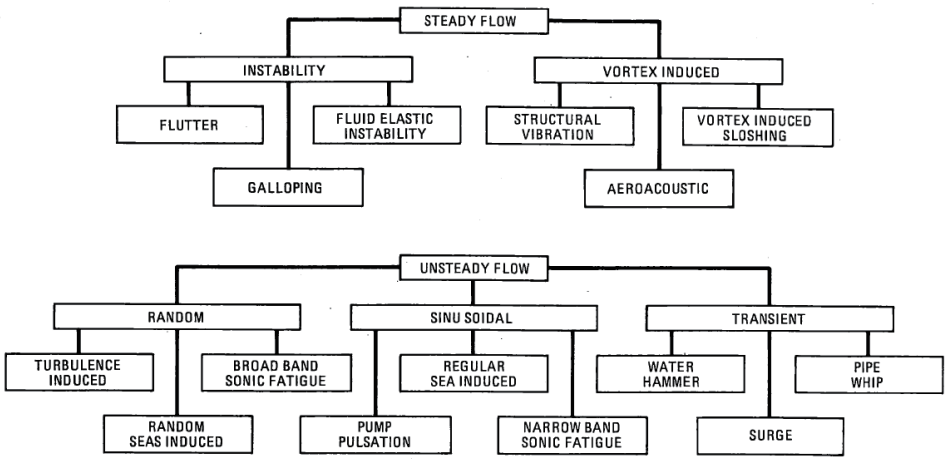

Figure 1.1 – A classification of flow induced vibrations, figure from Blevins [10]

action ('unsteady flow' case in Fig. 1.1). More detailed introductions on FSI can be found in [10, 19, 63, 58]. In this thesis, we focus on two fully-coupled fluid-structure interaction problems: the flapping flag instability and the fish swimming.

1.1.1 Flapping flag instability

As a canonical example of flow induced vibrations, the flapping of flags is also a subset of more general fluid-structure interaction problems that may concern the interaction of flexible structures (such as sheets or plates [25, 27], tubes [18, 57]) with high Reynolds number flows, and the interaction of flexible objects with low Reynolds number flows [42, 79]. The understanding of these phenomena is important to applications such as paper processing [74], energy harvesting [3, 52, 65], snoring [15], and turbulent reduction [64]. In this thesis, we restrict ourselves to the interaction of flexible sheets or plates with high Reynolds number flows.

It may be convenient to explain this problem using the experimental results of Zhang et al. [80] (see Fig. 1.2). Their experimental setup consists of a one-dimensional filament in a two-dimensional soap film flow, the interface fringes created by a monochromatic light source is used to visualize the flow.

In their experiment, three distinct states have been observed. Fig. 1.2a shows the stretched-straight (SS) sate for low flow speed in which the filament does not flap and is aligned with the flow. For this state, a thin von Kármán vortex street has been observed downstream from the trailing edge. As the flow velocity is increased, the flag begins to flap at a critical flow velocity U_c^*. The flapping motion and the surrounding flow are shown in Fig. 1.2b, and superimposed snapshots of the filament for one flapping cycle can be found in Fig. 1.2c. We can see that the amplitude of motion gradually increases from the leading edge to the trailing edge. There is no flow separation along the filament and a thin wake is shed from the trailing edge. Unlike the von Kármán vortex street in the SS state, the wake vortices share the same sign for the overall half-stroke and will alter sign for the next half-stroke. If the flow velocity is very large, the flag flaps with aperiodic motion as shown in Fig. 1.2d. As a counterpoint, Fig. 1.2e shows the flow around a rigid filament with flag-like shape, the flow separation has been observed and the vortices exist all along the filament since the filament obstructs the flow, as explained by Zhang et al. [80].

The experimental work of Eloy et al. [25] has clearly shown the hysteresis loop for a two-dimensional clamped-free plate immersed in a three-dimensional air flow. The motion amplitude is plotted with respect to reduced flow velocity in Fig. 1.3. We can find that the plate does not flap for low reduced flow velocity ($U^* < 10.3$), this corresponds to the stretched-straight state. As the reduced flow velocity is increased and in excess of $U_c^* = 10.3$, the periodic flapping of plate appears. However, when the reduced flow velocity is now decreased, the plate stops flapping at $U_d^* = 8$ instead of $U_c^* = 10.3$, thus exhibiting hysteresis. When the plate span becomes larger, the hysteresis is usually stronger.

Numerous experimental works on the flapping flag instability [17, 39, 62, 66, 67, 78] have shown that the flutter modes at threshold are one-dimensional. Another observation is that the measured critical flow velocity is generally larger than the theoretical or numerical predictions.

The flapping flag instability can be considered as a competition between destabilizing pressure forces and stabilizing bending stiffness. For the structure part, the flag motion is usually modeled by one-dimensional flutter modes as observed in most experiments. Thus, the Euler-Bernoulli beam equation can be applied to model inertial and internal mechanical forces of the flag. For the fluid part, the fluid model is usually divided into two categories according to the aspect ratio of the flag (ratio of span to chord). For the flags with small aspect ratio, Slender-body theory [46] is applied to calculate the pressure forces acting on the flag, then the studies of instability for slender flags [17, 43] are established. When a flag with large aspect ratio is considered, the flow can be treated as two-dimensional: applying

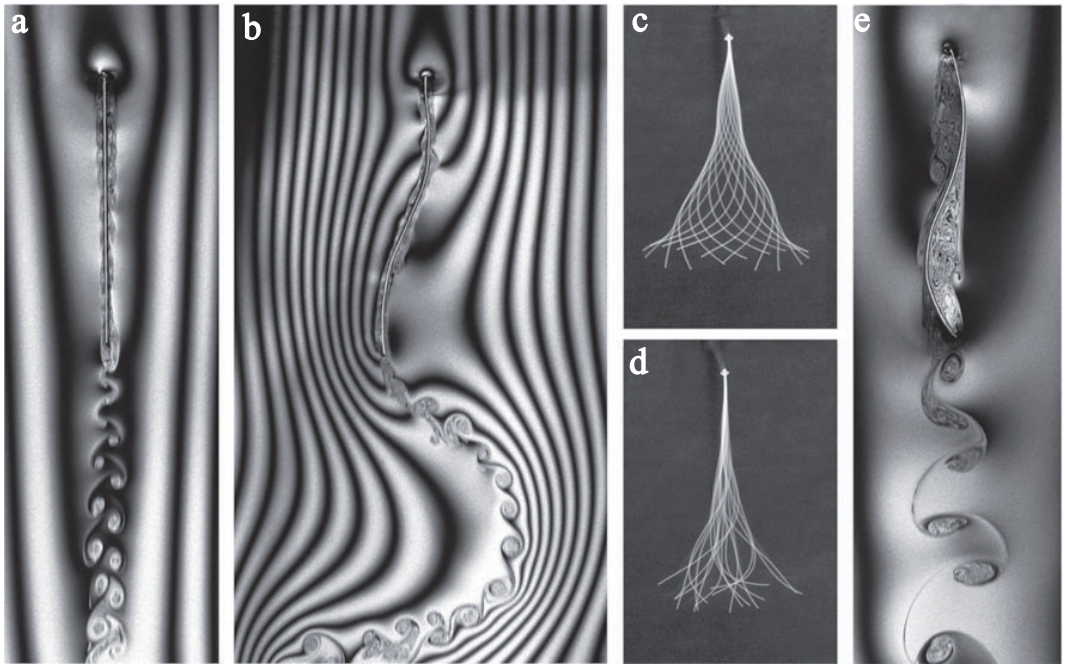

Figure 1.2 – Flow visualization of the wake structure downstream of a flexible filament made of silk thread and immersed in a running soap film. a) The stretched-straight state. b) flapping. c) A coherently flapping filament at several times along its flapping cycle. d) The same filament at higher flow speed, showing aperiodic flapping. e) The flow around a stiff metal wire bent permanently into the shape of a flapping filament. Results from Zhang et al. [80]

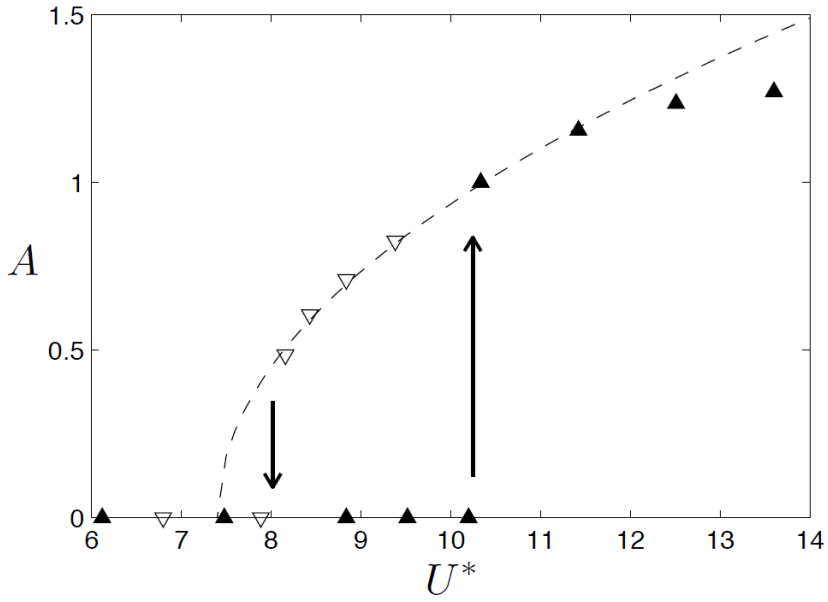

Figure 1.3 – Mode amplitude A (measured in arbitrary units) as a function of the reduced velocity. Amplitude is plotted as filled triangles when velocity is increased and open triangles when it is decreased. The aspect ratio is $H^* = 1$ and the mass ratio is $M^* = 0.6$. The instability exhibits a strong hysteresis with $U_c^* = 10.3$ and $U_d^* = 8$. Results from Eloy [25]

the 2D unsteady airfoil theory [68] as done in the models of [34, 39, 74]; or solving the pressure distribution in the Fourier space as performed by [27, 32].

However, for a flag with intermediate aspect ratio, there is not a simple theoretical way to model the surrounding flow. Shayo [61] may be the first to address the influence of plate span (or equivalently intermediate aspect ratio) on the critical flow velocity. He made a three-dimensional stability analysis by employing linearized plate and potential flow theories together with asymptotic expressions for the generalized pressures. Shayo claimed that a two-dimensional analysis (infinite aspect ratio) may yield an overestimate of the critical flow velocity for finite width panels. It can be inferred that a plate with infinite span should be more stable than the finite one. This conclusion is not in accord with the stability analysis for slender flags [17, 43]. Lucey & Carpenter [50] have carried out a theoretical stability analysis of a compliant panel of finite dimensions embedded in a rigid wall. Note that a compliant panel is stable for low flow speed, becomes unstable for the flow speeds in excess of a critical value, and the motion of panel for high flow speeds can be modeled by flutter modes which consists of downstream propagating waves, thus this problem exhibits a strong analogy to the flapping flags. They found that a compliant wall of finite span is always more stable than its infinite counterpart. Recently, Eloy et al. [27] has made an extension of the anylysis of Guo & Païdoussis [32] to study the effect of finite span on the critical flow velocity. They found that the system is more stable for the plate with smaller span, thus in accord with results of Argentina & Mahadevan [4] and Lucey & Carpenter [50].

The discrepancy between the measured critical flow velocity and the theoretical/numerical predictions has been studied theoretically and experimentally by Eloy et al. [25]. They observed that the flutter modes at threshold is no longer one-dimensional for the plate with aspect ratio $H^* \geq 2$. Thus, the nonlinear Föppl-von Kármán equation [5, 20] should be applied to model the plate motion if the deflection along the span can not be neglected. Accordingly, a three-dimensional fluid model is needed. More recently, Eloy et al. [24] has studied the origin of hysteresis by examining the nonlinear aspect of flapping flag instability. They proposed the nonlinear model in the limit of small and large aspect ratio, and carried out the experiments with flat plates and curved plates. They concluded that the planeity defect of plate could be the main cause for the hysteresis and the discrepancy.

In this thesis, the effects of aspect ratio will be re-examined. We will propose a three-dimensional theoretical model which can model the flow surrounding a surface with intermediate aspect ratio. Using the fluid-structure interaction model originally proposed by Eloy et al. [27], we will study the influence of aspect ratio and mass ratio on the flutter modes, critical flow velocity.

1.1.2 Fish swimming

Fish swimming is of interest not only for its locomotory performance in terms of burst speed, acceleration or agility, but also it is a fundamental problem of fluid mechanics of intrinsic complexity. Fish of many species propel themselves by passing a bending wave down their bodies, which is called 'undulatory swimming', or 'body and caudal fin' propulsion since the flexion is located at the level of the body and caudal fin. The majority of fish use 'undulatory swimming' as their main mode of locomotion. Others swim by the 'Median and paired fin' propulsion [9] (for example bluefish), or by jet propulsion [16] (for example jellyfish).

Based on the biological observations, undulatory swimmers can be divided into two groups: elongated eel-like swimmers, and salmon-like or tuna-like ones. Geometrically speaking, the elongated swimmers have elongated bodies, whose aspect ratio is of 0.1 and cross section do not vary much along the body length. While the bodies of salmon-like or tuna-like swimmers have aspect ratio about 0.2. Their bodies consist of three parts: the large and streamlined anterior region (accounting for the most of body mass), the caudal peduncle of highly reduced cross section, and the caudal fin. For the aspect of swimming motion, the elongated swimmers swim by bending their whole body, and the envelope of the motion

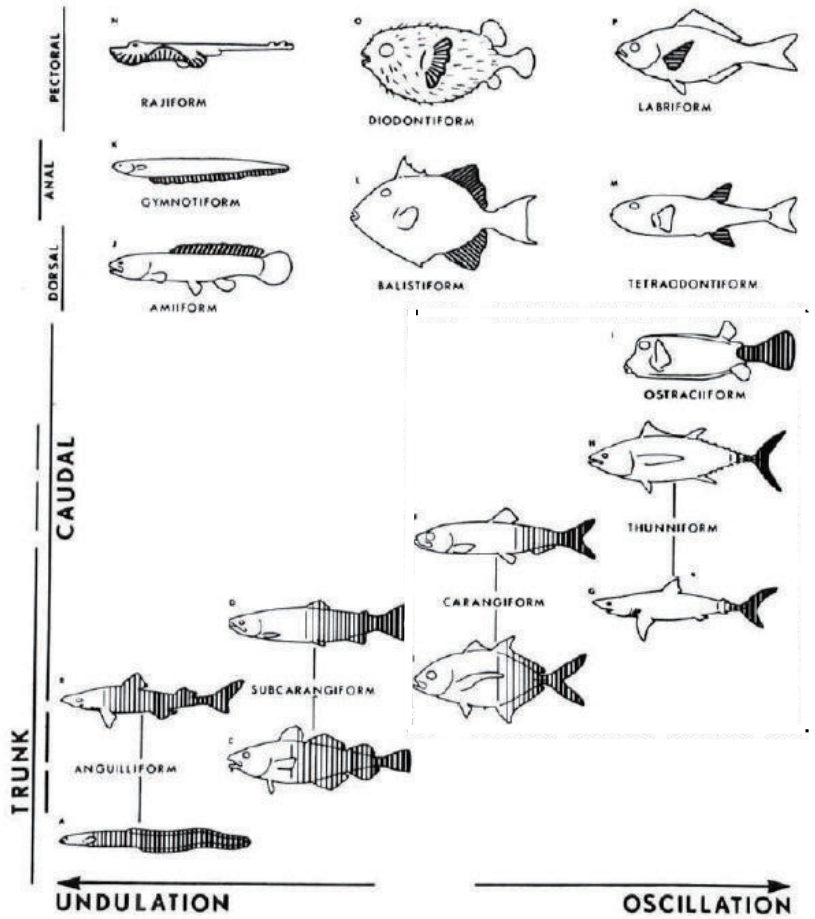

Figure 1.4 – The classification of fish swimming mode, figure from Lindsey [49]

grows linearly from head to tail. This swimming mode is usually called as anguilliform locomotion. While the salmon-like or tuna-like swimmers bend only the posterior part of body to propel themselves, thus they are usually described as a motionless cargo (the anterior region) propelled by the moving propeller (caudal fin). This swimming mode can be divided into three subclasses: sub-carangiform, carangiform and thunniform locomotion, according to the localization of bending along the body length. Although this classification [41, 49, 60] does not concern any phylogenetic considerations (i.e. related to the evolutionary tree) or metabolic performances, it gives an clear view of the fish geometry and the swimming gaits (see Fig. 1.4).

The studies on fish swimming date back to Gray [29] and Bainbridge [6, 7], and have been reviewed numerous times [2, 8, 30, 45, 41, 73, 70, 76]. Despite various works on fish locomotion (from physiology to physics of swimming), optimization studies are relatively spare.

Lighthill [45, 47] is probably the first to address physically the optimization in undulatory swimming, based on linear elongated-body theory [46]. By qualitative analysis, Lighthill [47] concluded that the morphology of carangiform (tuna-like) swimmers is well adopted to the motion: the localization of the large amplitude motion in the posterior region (caudal fin) is simply aiming at reducing the wasted energy; the envelope of motion should tend be constant when approaching the trailing edge of tail, and this leads to a narrow region (caudal peduncle) separating the tail from the anterior region; to minimize the inefficient recoil pitching motion, most of the mass should be localized in the anterior region.

Li et al. [44] have investigated numerically the performance of locomotion of flapping plates

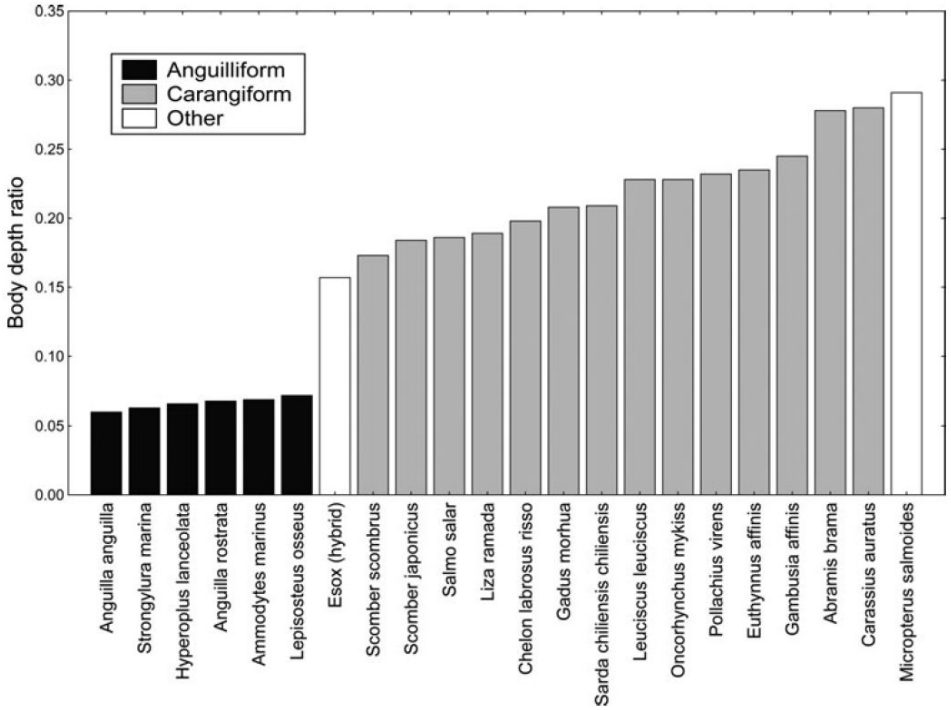

Figure 1.5 – Average aspect ratio of various fish. Result from van Weerden et al. [72]

of typically fish-like shape. Their numerical results show that the plates of forked shape have better performance than the unforked ones. They conclude that the caudal fin in carangiform mode has greater thrust, and the lunate tail fin in thunniform mode has higher efficiency. They also investigated the wake topology and the influence of wake on the thrust.

The optimal body shape and corresponding motion for achieving lowest energetic costs, or highest swimming speed have been investigated by Eloy [22]. This study is performed using an evolutionary algorithm which considers the fluid mechanics as the main selective pressure. The model is weakly non-linear, includes the resistive forces and the enhancement of skin-friction drag. His results yielded two distinct species: one specialized in economical swimming and the other in large swimming speed. Through comparison with experimental data, Eloy concluded that the evolution is consistent with the selection of species with low energetic costs. Similarly, Tokić and Yue [69] performed the optimization of body shape and lateral motion for maximum efficiency or swimming speed. Their model is linear, and more efforts are made on the physiological feasibility of the optimal body shape and motion. Despite the difference of model, their main results are very similar to those of Eloy [22].

As shown in Fig. 1.5, the fish of a given swimming mode either (anguilliform or carangiform) share the same aspect ratio. One interesting question is that: is it the result of evolution, or is this the optimized morphology? However, when we want to perform the optimization in terms of aspect ratio, none of the elongated-body theory [46, 48] or the waving plate theory [77] can give accurate pressure forces acting on the body. One may apply the numerical method to calculate the pressure force, but considering the computational costs during the optimization, we try to propose a theoretical model which can be applied for different aspect ratio. Since this work is still in progress, only the qualitative analysis on the thrust and the optimal shape is performed.

1.2 Fluid model

When considering the fluid-structure interaction between a flexible body and a surrounding fluid, the flow field is generally divided into two regions: the outer flow (away from the body boundaries) where the viscous effect plays a minor role; the inner flow composed of boundary layer (near the body boundaries) and the wake, where viscosity can not be neglected.

If vorticity is negligible in the outer flow and the fluid is assumed to be incompressible, potential flow theory can be used to model the outer flow field, which consists of a three-dimensional Laplace equation with Neumann boundary condition. When the body immersed in the flow is sufficiently wide, the Laplace equation is reduced to be two-dimensional (chord-wise and lateral direction), then 2D unsteady airfoil theory [77] (section 1.2.2) is proposed. Similarly, if an elongated body is considered, a two-dimensional (span-wise and lateral direction) Laplace equation is capable to model the surrounding flow for a given chord-wise position, Slender body theory [46] (section 1.2.1) is therefore derived.

For the flow surrounding a body with arbitrary geometry, the three-dimensional Laplace with Neumann boundary condition can be solved by means of Green representation theorem [53], and the problem transforms into a Fredholm integral equation of first kind with a singular kernel (section 1.3). However, there is no a simple method to solve this integral equation. Thus, numerical techniques, such as the vortex-lattice method [14, 36, 38, 71] (chapter 2), or the doublet-lattice methods [1, 59] have to be used to invert this integral equation. Moreover, if some asymptotic approximations are made in the limit of small or large aspect ratio, an asymptotic solution can be obtained using the perturbation method [21] (chapter 3).

1.2.1 Slender-body theory

For large Reynolds number flows, Slender body theory has been originally proposed by Munk [54] and developed by Lighthill [46] in 1960. It is a classic and popular model used to calculate the hydrodynamic forces produced by an elongated body moving in a uniform flow. The main principle of Slender body theory will be introduced in this section.

Consider a Cartesian coordinate system $(Oxyz)$ and a uniform, irrotational flow of inviscid fluid with density ρ. The flow velocity U is directed in the positive x-direction. A slender body aligned with the flow is moving in this flow and the lateral displacement is prescribed by $z = h(x, t)$ (see Fig. 1.6).

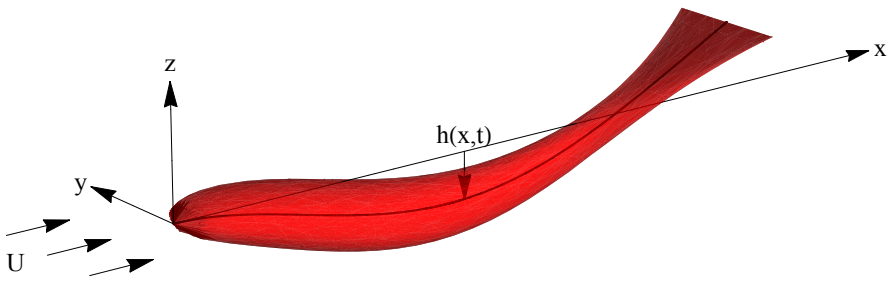

Figure 1.6 – Schematic of Slender body theory.

By applying a transformation of coordinates, the moving body becomes a fixed surface. The new coordinates X, Y, Z and T are defined by

$$X = x, \quad Y = y, \quad Z = z - h(x,t), \quad T = t, \tag{1.1}$$

hence, we have

$$\frac{\partial}{\partial x} = \frac{\partial}{\partial X} - \frac{\partial h}{\partial x}\frac{\partial}{\partial Z}, \quad \frac{\partial}{\partial y} = \frac{\partial}{\partial Y}, \quad \frac{\partial}{\partial z} = \frac{\partial}{\partial Z}, \quad \frac{\partial}{\partial t} = \frac{\partial}{\partial T} - \frac{\partial h}{\partial t}\frac{\partial}{\partial Z}. \tag{1.2}$$

The continuity equation becomes a Laplace equation if the flow velocity can be represented by $\nabla\phi$, and it becomes

$$\left(\frac{\partial}{\partial X} - \frac{\partial h}{\partial X}\frac{\partial}{\partial Z}\right)\left(\frac{\partial \phi}{\partial X} - \frac{\partial h}{\partial X}\frac{\partial \phi}{\partial Z}\right) + \frac{\partial^2 \phi}{\partial Y^2} + \frac{\partial^2 \phi}{\partial Z^2} = 0. \tag{1.3}$$

Lighthill introduced a slenderness parameter ϵ, so that the body's lateral dimension will not exceed ϵl, nor its lateral velocity ϵU (where l is the x-length of the body). Then the first term in Eq. (1.3) is of order ϵ^2 relative to the second or third one. Consequently, near the body only a two dimensional Laplace equation is necessary

$$\frac{\partial^2 \phi}{\partial Y^2} + \frac{\partial^2 \phi}{\partial Z^2} = O(\epsilon^2). \tag{1.4}$$

Noting that the impermeability boundary condition should be satisfied on the body boundary, that is

$$\nabla\phi \cdot \mathbf{n} = \frac{\partial h}{\partial T}\mathbf{e}_z \cdot \mathbf{n}, \tag{1.5}$$

in which $\mathbf{n}$ is the normal vector on the body boundary, $\mathbf{e}_z$ the unit Z-direction vector. If the surface of the stretched straight body can be described by the equation $F(X,Y,Z) = 0$, then the normal vector $\mathbf{n}$ is $(\partial_X F, \partial_Y F, \partial_Z F)$, the boundary condition of (1.4) can be therefore written as

$$\left(\frac{\partial \phi}{\partial X} - \frac{\partial h}{\partial X}\frac{\partial \phi}{\partial Z}\right)\left(\frac{\partial F}{\partial X} - \frac{\partial h}{\partial X}\frac{\partial F}{\partial Z}\right) + \frac{\partial \phi}{\partial Y}\frac{\partial F}{\partial Y} + \frac{\partial \phi}{\partial Z}\frac{\partial F}{\partial Z} = \frac{\partial h}{\partial T}\frac{\partial F}{\partial Z}. \tag{1.6}$$

Based on the small amplitude assumption, the potential flow around an elongated body can be regarded as composed of

(i) the steady flow around the stretched straight body;
(ii) the flow due to lateral displacement $h(x,t)$.

A moving body is described as 'stretched straight' when it is held stationary in a standard position such that no resultant normal force acts on any cross section. Consequently, the velocity potential ϕ can be written as

$$\phi = UX + \phi_0(X,Y,Z) + \phi_1(X,Y,Z,T), \tag{1.7}$$

in which $UX + \phi_0(X,Y,Z)$ is the potential due to the incoming flow and the motionless stretched straight body, it depends only on the shape of body. Injecting expression (1.7) into Eq. (1.6) and neglecting the minor terms yields

$$U\left(\frac{\partial F}{\partial X} - \frac{\partial h}{\partial X}\frac{\partial F}{\partial Z}\right) + \left(\frac{\partial \phi_0}{\partial Y} + \frac{\partial \phi_1}{\partial Y}\right)\frac{\partial F}{\partial Y} + \left(\frac{\partial \phi_0}{\partial Z} + \frac{\partial \phi_1}{\partial Z}\right)\frac{\partial F}{\partial Z} = \frac{\partial h}{\partial T}\frac{\partial F}{\partial Z}. \tag{1.8}$$

The boundary condition for ϕ_0 can be derived by setting $h = 0$ and $\phi_1 = 0$

$$U\frac{\partial F}{\partial X} + \frac{\partial \phi_0}{\partial Y}\frac{\partial F}{\partial Y} + \frac{\partial \phi_0}{\partial Z}\frac{\partial F}{\partial Z} = 0. \tag{1.9}$$

Subtracting this from Eq. (1.8) gives the boundary condition for ϕ_1

$$\frac{\partial \phi_1}{\partial Y}\frac{\partial F}{\partial Y} + \left(\frac{\partial \phi_1}{\partial Z} - \frac{\partial h}{\partial T} - U\frac{\partial h}{\partial X}\right)\frac{\partial F}{\partial Z} = 0. \tag{1.10}$$

The method of calculating the steady flow potential ϕ_0 is fairly well known [54, 55], and it leads to a pressure distribution with no resultant force (d'Alembert paradox) or moment for a symmetrical shape. Noting that Eq. (1.4) with the boundary condition (1.10) only depends on coordinates Y and Z, this implies that for a given $X = M_0$, ϕ_1 can be regarded as the potential of the two-dimensional flow in the Y-Z plane, resulting from the movements of an infinite cylinder C_X, whose cross section S_X is defined by $F(M_0, Y, Z) = 0$, thus S_X is the same as that of slender body at $X = M_0$. The infinite cylinder C_X is shown as the green cylinder in Fig. 1.7. The lateral velocity of cylinder C_X in the Z-direction is

$$V(X,T) = \frac{\partial h}{\partial T} + U\frac{\partial h}{\partial X}. \tag{1.11}$$

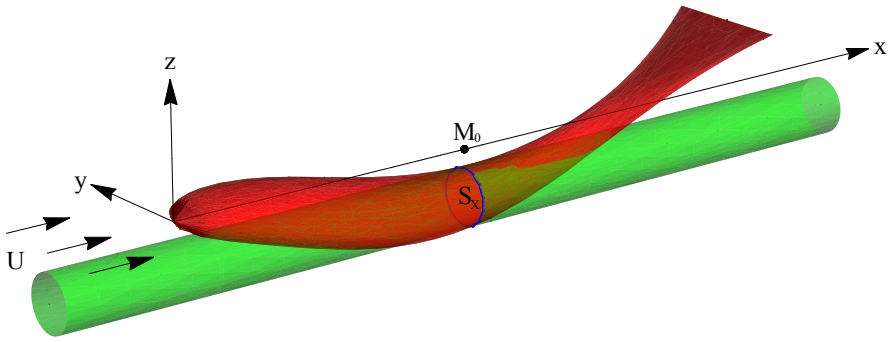

Figure 1.7 – Constitution of the equivalent cylinder C_X.

If $\Phi(X, Y, Z)$ is the potential due to the said cylinder C_X moving with unit velocity in the Z-direction through fluid at rest, then ϕ_1 can be rewritten as

$$\phi_1(X, Y, Z, T) = V(X, T)\Phi(X, Y, Z). \tag{1.12}$$

The pressure distribution is obtained from the unsteady Bernoulli equation

$$p - p_\infty = -\rho\left(\frac{\partial \phi}{\partial T} - \frac{\partial h}{\partial T}\frac{\partial \phi}{\partial Z}\right) - \rho\left(\frac{\partial \phi}{\partial X} - \frac{1}{2}\frac{\partial h}{\partial X}\frac{\partial \phi}{\partial Z}\right)^2 - \frac{1}{2}\rho\left(\frac{\partial \phi}{\partial Y}\right)^2 - \frac{1}{2}\rho\left(\frac{\partial \phi}{\partial Z}\right)^2 + \frac{1}{2}\rho U^2, \tag{1.13}$$

Injecting expression (1.7) into Eq. (1.13) and neglecting the terms of order ϵ^4, then we have

$$p - p_\infty = p_0 + p_1 + p_2, \tag{1.14}$$

with

$$
\begin{aligned}
p_0 &= \rho\left\{-U\frac{\partial\phi_0}{\partial X}-\frac{1}{2}\left(\frac{\partial\phi_0}{\partial Y}\right)^2-\frac{1}{2}\left(\frac{\partial\phi_0}{\partial Z}\right)^2\right\},\\
p_1 &= \rho\left\{-\frac{\partial\phi_1}{\partial T}-U\frac{\partial\phi_1}{\partial X}+\left(V-\frac{\partial\phi_1}{\partial Z}\right)\frac{\partial\phi_0}{\partial Z}-\frac{\partial\phi_1}{\partial Y}\frac{\partial\phi_0}{\partial Y}\right\},\\
p_2 &= \rho\left\{V\frac{\partial\phi_1}{\partial X}-\frac{1}{2}\left(\frac{\partial\phi_1}{\partial Y}\right)^2-\frac{1}{2}\left(\frac{\partial\phi_1}{\partial Z}\right)^2\right\}.
\end{aligned}
\tag{1.15}
$$

where p_0 is the steady pressure distribution past the stretched straight body, p_2 is the pressure distribution due to the steady motion of the cylinder C_X through fluid at rest with velocity V, and p_1 is the remainder of pressure distribution. Hence, p_0 depends only on the shape of stretched straight body, p_2 only on the steady lateral velocity V, and p_1 linearly on both.

Because of the stretched straight definition, p_0 has no contribution to the lift per unit length $L(X,T)$, which is the resultant force in the z-direction. Identically, p_2 does not contribute to the resultant force since the resistance to the motion of C_X in steady potential flow is zero (d'Alembert paradox). Therefore, only p_1 produces the Z-direction force

$$
L = \oint_{S_X} p_1 \mathbf{n}\cdot\mathbf{e}_z \mathrm{d}l, \tag{1.16}
$$

where the integral is taken over the bound of C_X. The normal vector $\mathbf{n}$, the infinitesimal arc $\mathrm{d}l$ in the Y-Z plane for $X = M_0$ are given by

$$
\begin{aligned}
\mathbf{n} &= \frac{1}{\sqrt{(\partial F/\partial Y)^2+(\partial F/\partial Z)^2}}\left(\frac{\partial F}{\partial Y},\frac{\partial F}{\partial Z}\right)\\
\mathrm{d}l &= \sqrt{1+\left(\frac{\partial F/\partial Y}{\partial F/\partial Z}\right)^2}\,\mathrm{d}Y
\end{aligned}
\tag{1.17}
$$

Substituting the above expressions into Eq. (1.16) results in

$$
L = \oint_{S_X} p_1 \mathrm{d}Y = L_1 + L_2, \tag{1.18}
$$

with

$$
\begin{aligned}
L_1 &= -\rho\oint_{S_X}\left(\frac{\partial}{\partial T}+U\frac{\partial}{\partial X}\right)\phi_1 \mathrm{d}Y,\\
L_2 &= -\rho\oint_{S_X}\left\{\left(\frac{\partial\phi_1}{\partial Z}-V\right)\frac{\partial\phi_0}{\partial Z}+\frac{\partial\phi_1}{\partial Y}\frac{\partial\phi_0}{\partial Y}\right\}\mathrm{d}Y.
\end{aligned}
\tag{1.19}
$$

Using the boundary condition (1.10) into the expression of L_2, and applying the Stokes' theorem, we obtain

$$
\begin{aligned}
L_2 &= -\rho\oint_{S_X}\left\{\frac{\partial\phi_1}{\partial Y}\frac{\partial\phi_0}{\partial Z}\mathrm{d}Z+\frac{\partial\phi_1}{\partial Y}\frac{\partial\phi_0}{\partial Y}\mathrm{d}Y\right\}\\
&= -\rho\iint_{E_X}\left\{-\frac{\partial^2\phi_1}{\partial Y^2}\frac{\partial\phi_0}{\partial Z}+\frac{\partial^2\phi_1}{\partial Y\partial Z}\frac{\partial\phi_0}{\partial Y}\right\}\mathrm{d}Y\mathrm{d}Z,
\end{aligned}
\tag{1.20}
$$

where the bound of area E_X is S_X. Using the two-dimensional Laplace equation for ϕ_1, then adding $\frac{\partial \phi_1}{\partial Z}\Delta\phi_0$, we have

$$\begin{aligned} L_2 &= -\rho \iint_{E_X} \left\{ \frac{\partial^2 \phi_1}{\partial Z^2}\frac{\partial \phi_0}{\partial Z} + \frac{\partial \phi_1}{\partial Z}\frac{\partial^2 \phi_0}{\partial Z^2} + \frac{\partial \phi_1}{\partial Z}\frac{\partial^2 \phi_0}{\partial Y^2} + \frac{\partial^2 \phi_1}{\partial Y \partial Z}\frac{\partial \phi_0}{\partial Y} \right\} \mathrm{d}Y\mathrm{d}Z \\ &= -\rho \iint_{E_X} \left\{ \frac{\partial}{\partial Z}\left(\frac{\partial \phi_1}{\partial Z}\frac{\partial \phi_0}{\partial Z}\right) + \frac{\partial}{\partial Y}\left(\frac{\partial \phi_1}{\partial Z}\frac{\partial \phi_0}{\partial Y}\right) \right\} \mathrm{d}Y\mathrm{d}Z. \end{aligned} \tag{1.21}$$

An application of the Stokes' theorem, then substitution of the boundary condition (1.9) gives

$$\begin{aligned} L_2 &= -\rho \oint_{S_X} \frac{\partial \phi_1}{\partial Z}\left(\frac{\partial \phi_0}{\partial Z}\mathrm{d}Y - \frac{\partial \phi_0}{\partial Y}\mathrm{d}Z\right) \\ &= -\rho \oint_{S_X} \frac{\partial \phi_1}{\partial Z}\left(\frac{\partial \phi_0}{\partial Z} + \frac{\partial \phi_0}{\partial Y}\frac{\partial F/\partial Y}{\partial F/\partial Z}\right)\mathrm{d}Y \\ &= \rho U \oint_{S_X} \frac{\partial \phi_1}{\partial Z}\frac{\partial F/\partial X}{\partial F/\partial Z}\mathrm{d}Y \\ &= -\rho U \oint_{S_X} \frac{\partial \phi_1}{\partial Z}\left(\frac{\partial Z}{\partial X}\right)_{Y constant}\mathrm{d}Y \end{aligned} \tag{1.22}$$

Now we introduce $\rho A(X)$ the added mass per unit length of the cylinder C_X (the explanations and evaluations of added mass can be found in [12]), whose cross section is S_X, and we then have

$$A(X) = \oint_{S_X} \Phi \mathrm{d}Y. \tag{1.23}$$

From this formula it follows that

$$\begin{aligned} -\rho\left(\frac{\partial}{\partial T} + U\frac{\partial}{\partial X}\right)\{VA(X)\} &= -\rho \oint_{S_X} \left[\left(\frac{\partial}{\partial T} + U\frac{\partial}{\partial X}\right)\{V\Phi\}\right. \\ &\quad \left. + UV\frac{\partial \Phi}{\partial Y}\left(\frac{\partial Y}{\partial X}\right)_{Y \text{ constant}} + UV\frac{\partial \Phi}{\partial Z}\left(\frac{\partial Z}{\partial X}\right)_{Y \text{ constant}}\right]\mathrm{d}Y \\ &= -\rho \oint_{S_X} \left(\frac{\partial}{\partial T} + U\frac{\partial}{\partial X}\right)\{V\Phi\}\mathrm{d}Y \\ &\quad - \rho U \oint_{S_X} V\frac{\partial \Phi}{\partial Z}\left(\frac{\partial Z}{\partial X}\right)_{Y \text{ constant}}\mathrm{d}Y, \end{aligned} \tag{1.24}$$

where the first term can be identified with L_1, the second term results from the variation of the cross section S_X with respect to X and is equal to L_2.

Thus, the lift per unit length which is the force in the z-direction on the cross section S_X can be derived

$$L(X,T) = -\rho\left(\frac{\partial}{\partial T} + U\frac{\partial}{\partial X}\right)\{VA(X)\}. \tag{1.25}$$

From the above calculation, we can find that by reducing the governing equation to a 2D Laplace equation, decomposing the potentials according to their origins, properly picking the dominating terms, Slender body theory gives a very simple equation to calculate the lift per unit length exerted on the moving body by the surrounding fluid.

1.2.2 2D unsteady airfoil theory

For a flexible body with large aspect ratio moving in a high Reynolds number flow, 2D unsteady airfoil theory can be applied to calculate the force exerted on the moving body. In this section, 2D unsteady airfoil theory will be summarized (more details can be found in [77]).

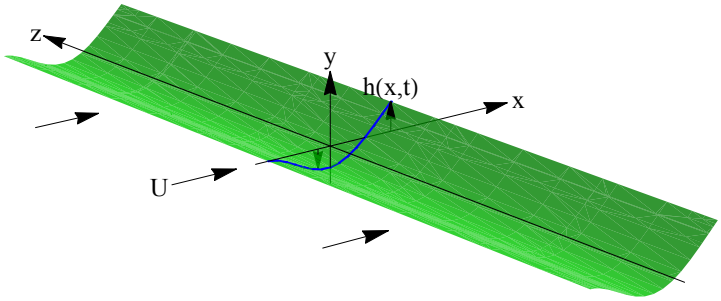

Figure 1.8 – Schematic of 2D unsteady airfoil theory.

Consider a two-dimensional incompressible flow of an inviscid fluid generated by the motion of a deformable plate of zero thickness spanning from $x = -1$ to $x = 1$ (thus taking half-chord as characteristic length) in an otherwise uniform flow of constant velocity U in the positive x-direction (see Fig. 1.8). The motion of the flexible plate may be prescribed in the general form by

$$y = h(x,t), \ -1 < x < 1, \tag{1.26}$$

where $h(x,t)$ is an arbitrary continuous function of x for every time t, and h and $\partial h/\partial x$ are assumed small compared to unity. Consequently, the flow velocity can be expressed by $\mathbf{q} = (U+u, v)^T$ and the continuity equation of flow becomes

$$\text{div } \mathbf{q} = \frac{\partial u}{\partial x} + \frac{\partial v}{\partial y} = 0. \tag{1.27}$$

Consider $(u,v)^T$ as a small perturbation of incoming flow velocity U, the Euler equation may be linearized and gives

$$\left(\frac{\partial}{\partial t} + U\frac{\partial}{\partial x}\right)\mathbf{q} = -\frac{1}{\rho}\text{grad } p = \text{grad } \varphi, \tag{1.28}$$

where the Prandtl's acceleration potential φ is defined by

$$\varphi(x,y,t) = (p_\infty - p)/\rho, \tag{1.29}$$

in which ρ is the density, p the pressure of the fluid and p_∞ the pressure at infinity.

The impermeability condition requires that the component of flow velocity normal to the moving solid boundary must be equal to the plate normal velocity

$$\mathbf{q}\cdot\mathbf{n}=\frac{\partial h}{\partial t}\mathbf{e}_z\cdot\mathbf{n},\quad\text{with}\quad\mathbf{n}\simeq\left(-\frac{\partial h}{\partial x},1\right)^T. \tag{1.30}$$

Then, the y-direction component of perturbation flow velocity should be

$$v=\frac{\partial h}{\partial x}+U\frac{\partial h}{\partial t}\quad\text{on}\quad y=\pm 0\ (-1<x<1). \tag{1.31}$$

Now, the problem will be formulated with complex acceleration potential. Taking the divergence of (1.28) and making use of (1.27), we obtain

$$\frac{\partial^2\varphi}{\partial x^2}+\frac{\partial^2\varphi}{\partial y^2}=0, \tag{1.32}$$

hence, φ is a harmonic function of (x,y) for every t. A conjugate harmonic function $\psi(x,y,t)$ can be defined by Cauchy-Riemann equations

$$\frac{\partial\varphi}{\partial x}=\frac{\partial\psi}{\partial y},\quad\frac{\partial\varphi}{\partial y}=-\frac{\partial\psi}{\partial x}. \tag{1.33}$$

Then, the complex acceleration potential is defined

$$f(z,t)=\varphi(x,y,t)+i\psi(x,y,t),\ \text{with}\ z=x+iy, \tag{1.34}$$

where $i=\sqrt{-1}$ is the imaginary unit. By introducing the complex flow velocity

$$w(z,t)=u(x,y,t)-iv(x,y,t), \tag{1.35}$$

Eq. (1.28) can be rewritten as

$$\frac{\partial f}{\partial z}=\frac{\partial w}{\partial t}+U\frac{\partial w}{\partial z}, \tag{1.36}$$

in which the real and imaginary parts represent Eq. (1.28) in x-direction and y-direction, respectively. An integration of (1.36) gives w in terms of $f(z,t)$

$$w(z,t)=\frac{1}{U}\int_{-\infty}^{z}g\left(z_1,t+\frac{z_1-z}{U}\right)\mathrm{d}z_1,\quad g(z,t)=\frac{\partial f(z,t)}{\partial z}. \tag{1.37}$$

The impermeability boundary condition for $f(z,t)$ can be given by injecting (1.31) into the y-direction part of Eq. (1.28) and making use of (1.33)

$$-\frac{\partial\psi}{\partial x}=\left(\frac{\partial}{\partial x}+U\frac{\partial}{\partial x}\right)^2 h(x,t)\quad\text{on}\quad y=\pm 0\quad(-1<x<1). \tag{1.38}$$

As v and ψ are even with respect to y, u and ψ should be odd according to the Cauchy-Riemann equations. Then, we have

$$\varphi(x,0,t)=0\quad\text{for}\quad|x|>1\quad\text{and for all } t. \tag{1.39}$$

The Kutta condition states that the flow leaves tangentially the trailing edge, i.e., the velocity at the trailing edge is finite, this requires

$$|f(1,t)| < \infty, \quad z = 1 \quad \text{for all } t. \tag{1.40}$$

Since the potential is considered as a small perturbation to the incoming flow, it should vanish at infinity, thus we have

$$f(z,t) \to 0 \quad \text{as} \quad |z| \to \infty; \qquad w(z,t) \to 0 \quad \text{as} \quad z \to -\infty, \tag{1.41}$$

which justifies a posteriori the convergence of the integral (1.37).

The statement of problem for a arbitrary deflection $h(x,t)$ is finished. It is composed of the Laplace equation (1.32) and boundary conditions (1.38 - 1.41) in terms of complex acceleration potential $f(z,t)$.

Now, we consider the harmonic motion of a flexible plate, which can be expressed in a general form

$$h(x,t) = h_1(x)e^{i\omega t} \quad \text{for} |x| < 1, \tag{1.42}$$

where $h_1(x)$ is an arbitrary real function of x, but may in general be complex with respect to i. By the conformal map

$$z = (\zeta + \zeta^{-1})/2, \tag{1.43}$$

the original z-plane, cut along the x-axis from $x = -1$ to x=1, is mapped on the region outside the unit circle $|\zeta| = 1$. On the unit circle, $\zeta = e^{i\theta}$, and hence

$$x = \cos\theta. \tag{1.44}$$

h and $\partial h/\partial x$ must be even in θ due to the zero thickness of plate. Expanding $h_1(x)$ in a Fourier cosine series, we then have

$$h(x,t) = \left[\frac{1}{2}\beta_0 + \sum_{n=1}^{\infty} \beta_n \cos(n\theta)\right] e^{i\omega t}, \tag{1.45}$$

where the Fourier coefficient β_n are given by

$$\beta_n = \frac{2}{\pi}\int_0^{\pi} h_1(\cos\theta)\cos(n\theta)\mathrm{d}\theta \quad n = 0, 1, 2, \cdots \tag{1.46}$$

From (1.44), we have

$$\frac{\partial}{\partial x} = -\frac{1}{\sin\theta}\frac{\partial}{\partial\theta} \quad \text{for} \quad y = 0 \quad |x| < 1. \tag{1.47}$$

Then, an injection of above formulas into (1.45) leads to

$$\frac{\partial h}{\partial x} = \frac{1}{\sin\theta}\sum_{n=1}^{\infty} n\beta_n \sin(n\theta)e^{j\omega t} = \left[\frac{1}{2}\gamma_0 + \sum_{n=1}^{\infty}\gamma_n\cos(n\theta)\right] e^{i\omega t}, \tag{1.48}$$

where the coefficients γ_n are given by

$$\gamma_{2n} = 2\sum_{m=n}^{\infty}(2m+1)\beta_{2m+1}, \qquad \gamma_{2n+1} = 2\sum_{m=n}^{\infty}(2m+2)\beta_{2m+2}, \qquad n = 0, 1, 2, \cdots. \tag{1.49}$$

Substituting (1.45 - 1.49) into (1.31) gives

$$v(x, \pm 0, t) = -U\left[\frac{1}{2}\lambda_0 + \sum_{n=1}^{\infty}\lambda_n \cos(n\theta)\right] e^{i\omega t}, \tag{1.50}$$

where

$$\lambda_n = -(\gamma_n + j\sigma\beta_n), \quad \sigma = \omega/U, \quad \text{for} \quad n = 0, 1, 2, \cdots \tag{1.51}$$

The reduced frequency σ is defined with unit half-chord, if the chord is c, σ must be $\omega c/(2U)$.

The solution for $f(z,t)$ satisfying conditions (1.50 - 1.51) and (1.38 - 1.41) is obtained by Küssner & Schwarz [40], and only the results are presented here. The complex acceleration potential $f(z,t)$ can be written in the form

$$f(z,t) = \varphi + i\psi = iU\left[\frac{a_0}{\zeta+1} + \sum_{n=1}^{\infty}\frac{a_n}{\zeta^n}\right] e^{i\omega t}, \tag{1.52}$$

accordingly we have

$$\begin{aligned} \varphi &= U^2\left[\frac{a_0}{2}\tan\frac{\theta}{2} + \sum_{n=1}^{\infty} a_n \sin(n\theta)\right] e^{i\omega t}, \\ \psi &= U^2\left[\frac{a_0}{2} + \sum_{n=1}^{\infty} a_n \cos(n\theta)\right] e^{i\omega t}, \end{aligned} \tag{1.53}$$

where the coefficients a_n are given by

$$\begin{aligned} a_0 &= (\lambda_0 + \lambda_1)C(\sigma) - \lambda_1, \quad C(\sigma) = \frac{K_1(j\sigma)}{K_0(j\sigma) + K_1(j\sigma)}, \\ a_n &= \lambda_n + \frac{j\sigma}{2n}(\lambda_{n-1} - \lambda_{n+1}), \quad n = 1, 2, 3, \cdots \end{aligned} \tag{1.54}$$

in which K_0 and K_1 are the modified Bessel functions of the second kind, and $C(\sigma)$ is called the Theodorsen's function [68].

Therefore, the pressure difference across the plate can be derived from (1.53)

$$\begin{aligned} \Delta p &= p(x, 0^-, t) - p(x, 0^+, t) = \rho[\varphi(x, 0^-, t) - \varphi(x, 0^+, t)] \\ &= \rho U^2\left[a_0 \tan\frac{\theta}{2} + 2\sum_{n=1}^{\infty} a_n \sin(n\theta)\right] e^{i\omega t}. \end{aligned} \tag{1.55}$$

Then, the lift on the solid plate is

$$L = \int_{-1}^{1} \Delta p \, \mathrm{d}x = \int_0^{\pi} \Delta p \, \sin\theta \, \mathrm{d}\theta = \pi\rho U^2(a_0 + a_1)e^{i\omega t}. \tag{1.56}$$

The moment of force about the mid-chord, positive in the nose-up sense, is

$$M = -\int_{-1}^{1} \Delta p \; x \; \mathrm{d}x = \frac{1}{2}\pi\rho U^2(a_0 - a_2)e^{i\omega t}. \tag{1.57}$$

From the above calculations, it can be seen that the problem formulation is firstly achieved for an arbitrary small deflection $h(x,t)$ by considering the Laplace Equation and its boundary conditions in terms of the complex acceleration potential $f(z,t)$. Then, a particular deflection $h_1 e^{j\omega t}$ is considered, and the boundary conditions are reconstructed by introducing the conformal mapping and Fourier series. Finally, the solution $f(z,t)$ can be found by applying the general theory for oscillating deformable airfoils. And consequently, the pressure difference across the plate Δp, the lift on the plate L and the moment of force about the mid-chord M can be obtained.

1.3 General formulation of the lifting surface integral

Consider a Cartesian coordinate system $(OXYZ)$ and a uniform, incompressible, irrotational flow of an inviscid fluid with density ρ. The flow velocity U is directed in the positive X-direction. A flexible surface is moving at angular frequency Ω around the reference plane $Z = 0$ (see Fig. 1.9). The surface displacement $h(X,T)$ is assumed sufficiently small that two hypotheses can be made: the surface and its trailing vortex sheet can be represented by their respective projection onto the reference plane, namely S and Σ; the motion of surface can be considered as small periodic perturbation to the incident flow. The flow around the surface is three-dimensional, and the motion of the surface is two-dimensional.

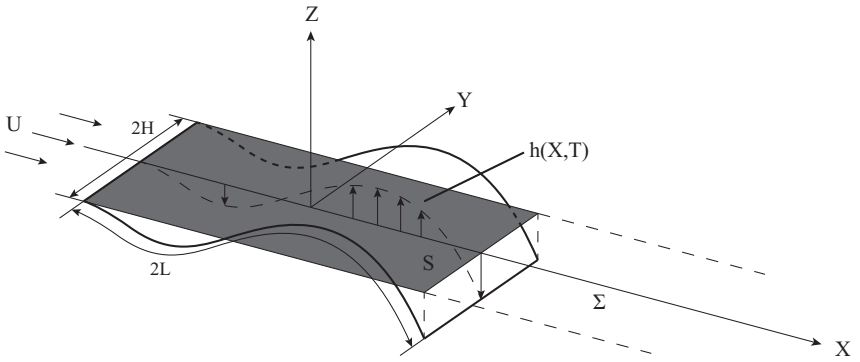

Figure 1.9 – Schematic of the lifting surface problem.

For the sake of simplicity, the complex factor $e^{i\Omega T}$ for all quantities will be omitted in this section, M_0 is an arbitrary point on S, M is any point on S or Σ, P represents any point belonging to the flow domain outside S and Σ.

The lateral motion of the flexible surface prescribes a perturbation of the flow velocity in the Z-direction (see above Eq. 1.31)

$$\mathrm{W}(M_0) = (i\Omega + U\partial_x)h(M_0), \tag{1.58}$$

where $h(M_0)$ is the Z-direction displacement of the surface. Using the perturbation velocity potential Φ, the flow velocity for any point P can be represented as $U + \nabla\Phi(P)$, hence the continuity equation of the flow becomes the Laplace equation with a Neumann boundary condition.

$$\Delta\Phi(P) = 0, \quad \text{with} \quad \partial_z\Phi(M_0) = \mathrm{W}(M_0). \tag{1.59}$$

Note that the Z-derivative of the perturbation velocity potential has no definition on S, hence, we have to define

$$\partial_Z \Phi(M_0) = \lim_{Z_P \to 0^+} \partial_Z \Phi(P) = \lim_{Z_P \to 0^-} \partial_Z \Phi(P), \tag{1.60}$$

where M_0 is the projection of P onto the reference plane. Physically, this definition simply states that the Z-component flow velocity is a continuous function with respect to Z, including $Z = 0$ which is required by the impermeability condition on S.

The Eq. (1.59) can be solved by means of Green's representation theorem [53], and for any point P, the perturbation velocity potential can be written in the following form:

$$\Phi(P) = \int_{S+\Sigma} [\Phi](M) \frac{\partial}{\partial Z_P} G(M, P) \mathrm{d}S_M, \tag{1.61}$$

where $[\Phi]$ is the jump of Φ across S, and $G(M, P)$ is the elementary Green function of the Laplace equation:

$$[\Phi](M) = \Phi(X_M, Y_M, 0^+) - \Phi(X_M, Y_M, 0^-), \tag{1.62}$$

$$G(M, P) = -\frac{1}{4\pi |MP|}. \tag{1.63}$$

The Neumann boundary condition is imposed by applying Z-derivative operator onto Eq. (1.61) and taking the limit as Z_P to zero

$$\mathrm{W}(M_0) = \lim_{Z_P \to 0} \int_{S+\Sigma} [\Phi](M) \frac{\partial^2}{\partial Z_P^2} G(M, P) \mathrm{d}S_M, \tag{1.64}$$

where M_0 is the projection of P onto the reference plane. The existence of this limit is guaranteed physically, and it can be evaluated by exchanging the order of limit and integral, hence,

$$\mathrm{W}(M_0) = \fint_{S+\Sigma} [\Phi](M) F(M, M_0) \mathrm{d}S_M, \tag{1.65}$$

in which

$$F(M, M_0) = \lim_{Z_P \to 0} \frac{\partial^2}{\partial Z_P^2} G(M, P) = \frac{1}{4\pi |MM_0|^3}. \tag{1.66}$$

However, the above exchange of order is permitted only when the Hadamard finite-part integral definition (represented by the cross on the integral sign) [33] is adopted, then the singular integral in Eq. (1.65) can be calculated elegantly [11, 51] in the present context.

Once the potential jump $[\Phi]$ satisfying Eq. (1.65) is found, we can obtain the pressure jump across the surface by applying the linearized unsteady Bernoulli equation:

$$[P](M_0) = -\rho(i\Omega + U\partial_X)[\phi](M_0). \tag{1.67}$$

Note that the pressure jump should be zero in the wake and at the trailing edge of surface (Kutta condition), the potential jump should thus satisfy:

$$[\phi](X, Y) = [\Phi](L, Y) e^{i\Omega(L-X)/U}, \quad \text{on} \quad \Sigma \quad (X \geq L,\ -H < Y < H), \tag{1.68}$$

where $X = L$ is the trailing edge of surface. The X-periodicity of potential jump ensures the pressure jump is zero in the wake, and the Kutta condition at the trailling edge is guaranteed by the continuity of potential jump between S and Σ. The Eq. (1.68) also expresses that the potential jump in the wake is generated due to the advection of the potential jump from the trailing edge at velocity U. Since the above formulation has no limitations about the surface geometry, one just needs to replace the coordinate of trailing edge by the that of local trailing edge in (1.68) to model an alternative surface geometry.

The application of elementary Green function requires the body under consideration to have asymptotically small thickness. As well known, a zero thickness body leads to the singularity of pressure jump at the leading edge which is usually integrable. This singularity yields a force called leading edge suction, and it can be smoothed out by adding a finite thickness [21].

The prescribed perturbation velocity W is related to the unknown potential jump $[\Phi]$ through an integral equation (1.65) which is usually called lifting-surface equation. From the mathematical point of view, this equation is a Fredholm integral equation of first kind with kernel $F(|MM_0|)$. The potential jump $[\Phi]$ can be found by inverting Eq. (1.65). However, due to the singular nature of its kernel $F(|MM_0|)$, there is no simple method to invert this lifting-surface equation. In chapter 2, we will examine how to invert the lifting-surface equation using a numerical method called "vortex panel method". In chapter 3, we will see how the lifting surface integral can be solved analytically when considering the asymptotic limit of small aspect ratio.

Chapter 2

Numerical fluid model

Let us consider a moving surface submerged in an incompressible potential flow of inviscid fluid. With theoretical techniques we are capable to calculate the pressure distribution if some geometrical simplifications are made (like the hypotheses introduced in previous chapter). Even though these theoretical methods are relatively simple and make fast computations possible, the simplifying approximations can limits the applications. In contrast, the numerical techniques allow the treatment of more realistic geometries and the fulfillment of the boundary conditions on actual complex surfaces. Consequently, these numerical techniques give more accurate results and are very popular in the aerospace sector.

2.1 Unsteady lifting-surface method

The general principle and procedure of the classical unsteady lifting-surface method will be introduced to treat a three-dimensional thin lifting surface problem. The problem under consideration in this section is similar to problem introduced in section 1.3, but the motion could be non-periodic and the amplitude does not have to be small. More details can be found in the book of Katz & Plotkin [36].

2.1.1 Discretization and grid generation

As introduced in section 1.3, the moving surface is defined by the lateral displacement $Z = h(X, Y, T)$ and is divided into M chord-wise panels and N span-wise panels. Details about the grid can be found in Fig. 2.1. The leading segment of a vortex ring is placed at the corresponding panel's quarter chord line, and the collocation point is located at the center of panel's three-quarter chord line. The normal vector $\mathbf{n}_{i,j,T}$ is also defined at this point. A constant circulation $\Gamma_{i,j,T}$ is distributed for this vortex ring. A typical vortex ring (with corner points $ABCD$, circulation Γ_{ij}) and collocation point P_{ij} is shown in Fig. 2.2. The chord-wise counter i will have values between 1 and M, while the span-wise counter j varies from 1 to N. The coordinates of a vortex (or collocation point) can be identified by specifying its i,j counters.

Now it is necessary to address the wake shedding procedure. At the first time step, the problem is treated without free wake vortices and the trailing segments of the trailing edge vortex rings represent the starting vortex. At the second time step, the trailing edge vortex rings in the previous time step are shed into the wake with the local flow velocity and becomes the first row of wake vortex rings. These wake vortex rings keep the same strength and shape and are advected by the flow velocity U. In the following time steps, new wake vortex rings will be created and the existing wake vortices will maintain the strength unchanged (according to the Helmholtz theorem) and move with flow velocity U.

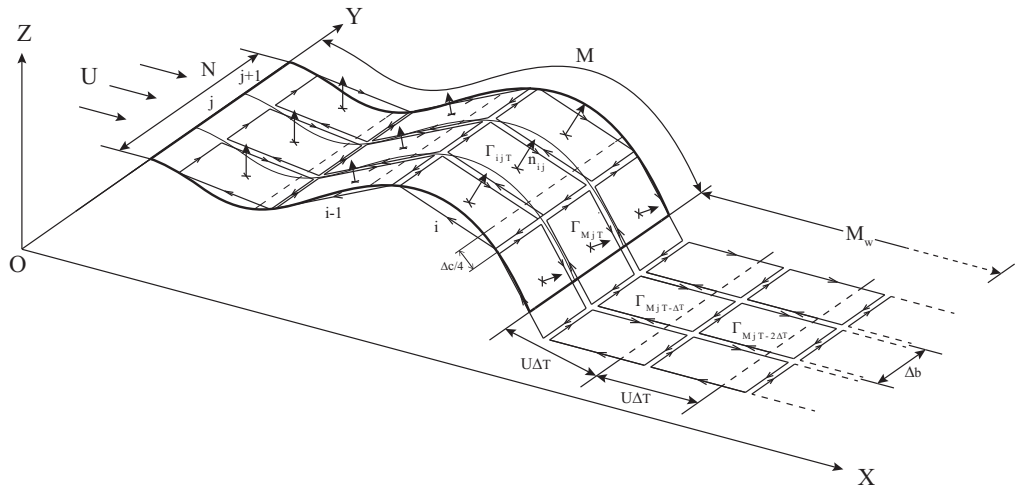

Figure 2.1 – Unsteady vortex ring model for a thin lifting surface.

The wake shedding procedure is shown in Fig. 2.1, and the strength of wake vortex rings are given by

$$\Gamma_{i,j,T} = \Gamma_{M,j,T-(i-M)\Delta T},\ i = M+1, M+2, \cdots \tag{2.1}$$

with

$$\Delta T = \frac{\Delta c}{U}, \tag{2.2}$$

in which ΔT is the time step, Δc chord-wise length of wake vortices.

At this stage, all the information such as coordinates of vortex rings corner points, panel area $S_{i,j,T}$, normal vector $\mathbf{n}_{i,j,T}$, coordinates of collocation points, strength of wake vortex rings should be calculated.

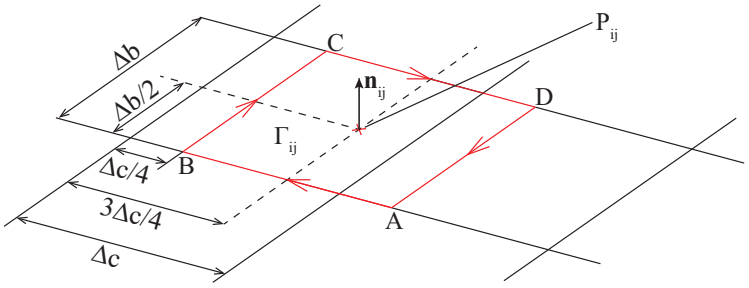

Figure 2.2 – Typical vortex ring element and collocation point.

2.1.2 Influence coefficient and the vector R

The purpose of this numerical method is to satisfy the impermeability condition across the moving surface, and it is achieved approximately by the fulfillment of zero normal flow velocity at all collocation points which requires

$$(\mathbf{V}_b + \mathbf{V}_\mathrm{w} + \mathbf{U} + \mathbf{V}_B) \cdot \mathbf{n}_{k,T} = 0, \quad k = 1, 2, \cdots, M \times N \tag{2.3}$$

where k is the sequential number $k = (i-1) \times N + j$, $\mathbf{V}_b$ and $\mathbf{V}_\mathrm{w}$ are the velocities at the collocation point k induced respectively by the unknown vortex rings on the surface and the known wake vortex rings, $\mathbf{U}$ is the incoming flow velocity, and $\mathbf{V}_B$ is the velocity at the collocation point k due to the surface motion (noting that $\mathbf{V}_B$ is the opposite of the surface motion).

Now, it is necessary to introduce the Bio-Savart Law for a straight vortex segment which is a part of vortex ring. As shown in Fig. 2.3, the straight vortex segment is pointing from A to B and with circulation Γ. The velocity $\mathbf{V}$ induced at P by this vortex segment can be derived [36]

$$\mathbf{V}(P, A, B, \Gamma) = \frac{\Gamma}{4\pi} \frac{\mathbf{r}_1 \times \mathbf{r}_2}{|\mathbf{r}_1 \times \mathbf{r}_2|^2} \mathbf{r}_0 \cdot \left(\frac{\mathbf{r}_1}{|\mathbf{r}_1|} - \frac{\mathbf{r}_2}{|\mathbf{r}_2|} \right), \tag{2.4}$$

with

$$\mathbf{r}_1 = \overrightarrow{AP}, \quad \mathbf{r}_2 = \overrightarrow{BP}, \quad \mathbf{r}_0 = \mathbf{r}_1 - \mathbf{r}_2. \tag{2.5}$$

The induced velocity is linear with respect to the circulation Γ and this allows the transformation of lifting surface integral to a linear system.

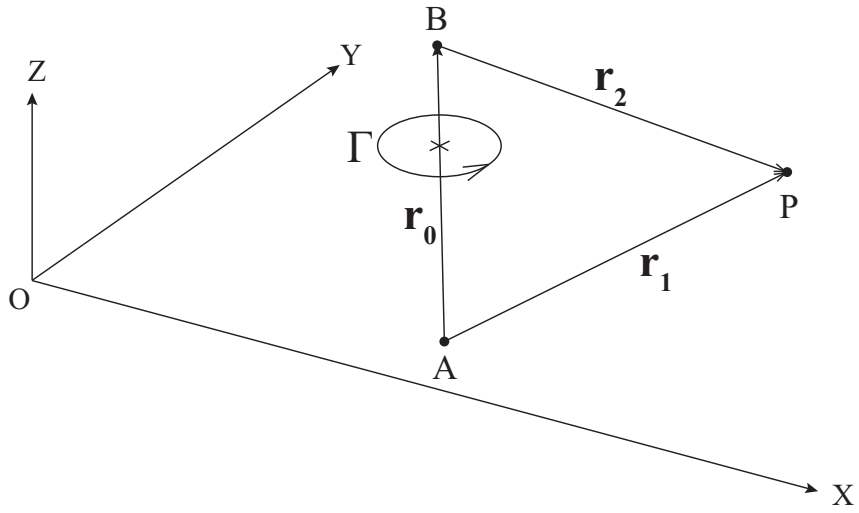

Figure 2.3 – The velocity induced by a three-dimensional, straight vortex segment.

From Eq. (2.4), the velocity induced at an arbitrary point P by a rectangular vortex ring with corner points $ABCD$ and circulation Γ can be given by

$$\mathbf{V}_{ring}(P, A, B, C, D, \Gamma) = \mathbf{V}(P, A, B, \Gamma) + \mathbf{V}(P, B, C, \Gamma) + \mathbf{V}(P, C, D, \Gamma) + \mathbf{V}(P, D, A, \Gamma). \tag{2.6}$$

and therefore, the velocity at the collocation point k by the vortex ring l can be derived

$$\mathbf{V}_{k,l,\Gamma_{l,T}} = \mathbf{V}_{ring}(P_k, A_l, B_l, C_l, D_l, \Gamma_{l,T}), \tag{2.7}$$

where P_k is the collocation point k, $A_l B_l C_l D_l$ are the corner points of the vortex ring l whose circulation is $\Gamma_{l,T}$.

A sum of velocity at collocation point k induced by all the vortex rings on the surface leads to

$$\mathbf{V}_b \cdot \mathbf{n}_{k,T} = a_{k1}\Gamma_{1,T} + a_{k2}\Gamma_{2,T} + \cdots + a_{km}\Gamma_{m,T}, \quad \text{with} \quad m = M \times N, \tag{2.8}$$

where the influence coefficient a_{kl} is defined by

$$a_{kl} = \mathbf{V}_{k,l,\Gamma_{l,T}=1} \cdot \mathbf{n}_{k,T}. \tag{2.9}$$

Similarly, the velocity due to all wake vortex rings with the known strength can also by calculated by

$$\mathbf{V}_{\mathrm{w}} \cdot \mathbf{n}_{k,T} = \mathbf{n}_{k,T} \cdot \sum_{l=m+1}^{m^*} \mathbf{V}_{k,l,\Gamma_{l,T}}, \quad \text{with} \quad m^* = (M + M_{\mathrm{w}}) \times N, \tag{2.10}$$

where M_{w} is the chord-wise number of wake vortex rings. The wake vortex circulations are already known from the previous time step as shown in Eq. (2.1). If it is the first time step, then $M_{\mathrm{w}} = 0$, if the second time step is considered, $M_{\mathrm{w}} = 1$, and so on. Note that M_{w} will increase to infinity if time keeps increasing, it means too many wake vortex rings are shed in the wake and accounted by the problem. However, this is not necessary, because the wake vortex which is far away from the surface induces very minor velocity on the surface. So, a truncation number $M_{\mathrm{w}} = 2 \times \max(M, N)$ is set to avoid the unnecessary computation costs, when too many wake vortex are accounted.

Since the surface is explicitly defined by $Z = h(X, Y, T)$, the surface velocity $-\mathbf{V}_B$ at the collocation point k can be easily calculated.

From Eq. (2.3), (2.8) and (2.10), the impermeability condition for the collocation point k reduces to

$$a_{k1}\Gamma_{1,T} + a_{k2}\Gamma_{2,T} + \cdots + a_{km}\Gamma_{m,T} = \mathrm{R}_{k,T}, \quad \text{with} \quad m = M \times N, \tag{2.11}$$

in which

$$\mathrm{R}_{k,T} = -(\mathbf{V}_{\mathrm{w}} + \mathbf{U} + \mathbf{V}_B) \cdot \mathbf{n}_{k,T}. \tag{2.12}$$

2.1.3 Solving the linear system

The fulfillment of the impermeability condition for all collocation point results in the following linear equation:

$$M_a \boldsymbol{\Gamma} = \mathbf{R}, \tag{2.13}$$

where M_a is the $m \times m$ influence matrix whose element a_{kl} is defined by Eq. (2.9), the vector $\boldsymbol{\Gamma}$ contains the unknown circulations of all vortex rings on the surface, and the elements of vector $\mathbf{R}$ are defined by Eq. (2.12). By solving this equation, the circulation of all all vortex rings on the surface can be determined.

2.1.4 Computation of pressure difference distribution

Once the circulation vector is calculated, the pressure difference distribution can be derived by using the unsteady Bernoulli equation, which can be written as (because the circulation of vortices is related to the velocity potential jump across the surface)

$$\Delta p_{i,j,T} = \rho \left([\mathbf{V}_B + \mathbf{V}_\mathrm{w} + \mathbf{U}]_{i,j,T} \cdot \boldsymbol{\tau}_i \frac{\Gamma_{i,j,T} - \Gamma_{i-1,j,T}}{\Delta c_{ij}} + [\mathbf{V}_B + \mathbf{V}_\mathrm{w} + \mathbf{U}]_{i,j,T} \cdot \boldsymbol{\tau}_j \frac{\Gamma_{i,j,T} - \Gamma_{i,j-1,T}}{\Delta b_{ij}} + \frac{\partial}{\partial T}\Gamma_{i,j,T} \right), \quad (2.14)$$

where Δc_{ij} and Δb_{ij} are the length in the i and j direction for panel ij. $\boldsymbol{\tau}_i$ and $\boldsymbol{\tau}_j$ are the tangential vector in the the i and j direction for panel ij. For the panel at the leading edge, the local circulation in Eq. (2.14) will be $\Gamma_{i,j,T}$ instead of $\Gamma_{i,j,T} - \Gamma_{i-1,j,T}$. Similar treatment is applied for the panels at the side edge.

Once the pressure distribution is obtained, it is possible to calculate the local or total lift. The advantage for this method is that it can account for surface with big or small amplitude, periodic or non-periodic motion. More realistic and complex phenomena can be modeled by this method, but we can see that the influence matrix M_a and vector R depend on time, which implies that the whole computation procedure should be repeated for every time step, and this can be extremely costly, especially when a refined grid is used.

2.2 Fixed-frequency lifting-surface method

The general principle and procedure of unsteady lifting-surface method presented in section 2.1 remain valid for all the moving bodies submerged in a incompressible potential flow. Thus, the problem introduced in section 1.3 can be easily treated. However, with the small amplitude motion assumption, it is possible to represent the boundary layer and the wake using vortex rings on the reference plane S and in the wake Σ, respectively (see Fig. 1.9). If the impermeability condition is required to be satisfied on S and we are interested in a single frequency only, the linear equation of the unsteady lifting-surface method transforms into a time-independent linear system, thus reducing computation costs.

2.2.1 Assumptions, modifications and algorithm

Discretization and grid generation

The moving surface is now defined by the harmonic function $Z = h(X, Y)e^{i\Omega T}$. As for general unsteady lifting surface method, the boundary layer on the moving surface is still modeled by M chord-wise panels and N span-wise panels on S. The wake vortex sheet is represented by M_w chord-wise panels and N span-wise panels on Σ. The grid is presented in Fig. 2.4. The index ij is still used to indicate the location of a vortex ring (or a collocation point). The chord-wise counter i will have values between 1 and M, and the span-wise counter j varies from 1 to N.

Like the classic unsteady lifting-surface method, the leading segment of a vortex ring is placed at the corresponding panel's quarter chord line and the collocation point is located at the center of panel's three-quarter chord line. The normal vector $\mathbf{n}_{ij}$ defined at the collocation point can be written as

$$\mathbf{n}_{i,j,T} \simeq (-\frac{\partial h}{\partial X}e^{i\Omega T}, -\frac{\partial h}{\partial Y}e^{i\Omega T}, 1) \quad (2.15)$$

For the vortex rings on the moving surface (represented by S), a circulation $\Gamma_{i,j}e^{i\Omega T}$ is distributed

$$\Gamma_{i,j,T} = \Gamma_{i,j}e^{i\Omega T}, \quad 1 \le i \le M, \quad 1 \le j \le N. \tag{2.16}$$

In order to fulfill the Kutta condition, the wake vortex rings are placed parallel to the local flow velocity (represented by the incident flow velocity U), and from Eq. (2.1), the circulations of wake vortex rings are given by

$$\Gamma_{i,j,T} = \Gamma_{M,j}e^{i\Omega(T-(i-M)\Delta c/U)}, \quad M+1 \le i \le M_{\mathrm{w}}, \quad 1 \le j \le N, \tag{2.17}$$

where Δc is the chord-wise length of vortex ring. This is similar to (1.68), which describes the wake shedding process and ensures the satisfaction of Kutta condition at the trailing edge.

In addition, coordinates of vortex rings corner points, panel area S_{ij}, coordinates of collocation points should be calculated.

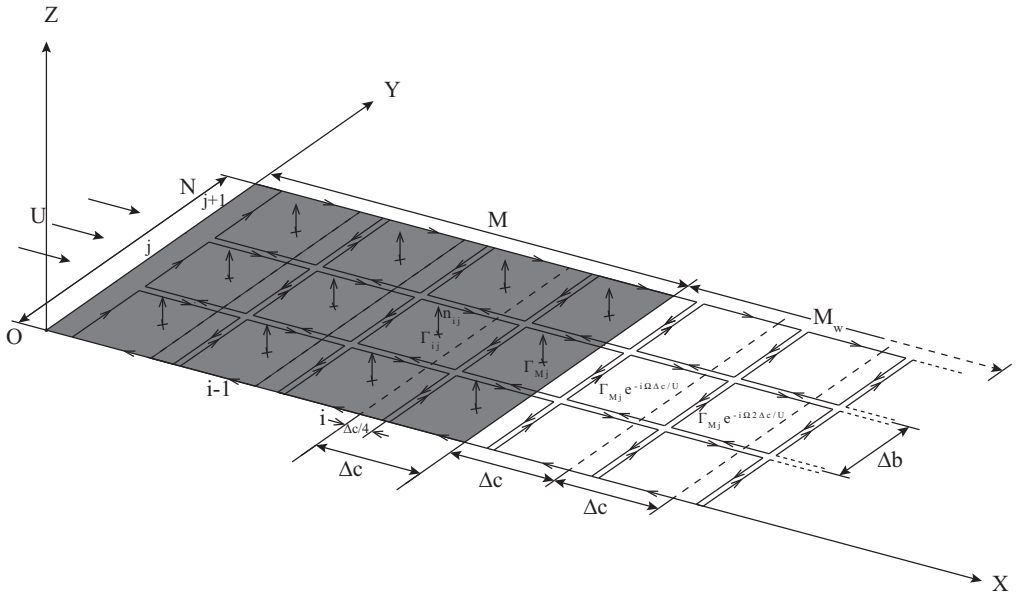

Figure 2.4 – Fixed-frequency vortex ring model for a thin lifting surface.

Influence coefficients and the vector R

Because of small amplitude motion hypothesis, $\frac{\partial h}{\partial X}$ and $\frac{\partial h}{\partial Y}$ should be asymptotically small compared with unity; the velocities induced respectively by the vortex rings on the surface and the wake vortex rings are asymptotically small compared with $\mathbf{U}$. Neglecting the minor terms, the impermeability condition (2.3) for the collocation point k reduces to

$$\mathbf{V}_b \cdot \mathbf{e}_Z + \mathbf{V}_{\mathrm{w}} \cdot \mathbf{e}_Z - \frac{\partial h}{\partial X} U e^{i\Omega T} + \mathbf{V}_B \cdot \mathbf{n}_{k,T} = 0, \quad k = 1, 2, \cdots, M \times N, \tag{2.18}$$

where k is the sequential number $k = (i-1) \times N + j$.

A sum of normal velocities at the collocation point k induced by all the vortex rings on the surface leads to

$$\mathbf{V}_b \cdot \mathbf{e}_Z = (a^*_{k1}\Gamma_1 + a^*_{k2}\Gamma_2 + \cdots + a^*_{km}\Gamma_m)e^{i\Omega T}, \quad \text{with} \quad m = M \times N, \tag{2.19}$$

where

$$a^*_{kl} = \mathbf{V}_{k,l,\Gamma_l=1} \cdot \mathbf{e}_Z, \quad 1 \le k, l \le m. \tag{2.20}$$

Similarly, the normal velocity due to all the wake vortex rings can also by calculated by

$$\mathbf{V}_{\mathrm{w}} \cdot \mathbf{e}_Z = e^{i\Omega T} \sum_{l=m-N+1}^{m} b_{kl}\Gamma_l, \tag{2.21}$$

in which b_{kl} is the normal velocity induced by the wake vortex rings shed from the unity strength trailing edge vortex indexed by $l = m - N + j$.

$$b_{kl} = \sum_{n=1}^{M_{\mathrm{w}}} \vec{V}_{k,l^*_n,\Gamma_{l^*_n}} \cdot \vec{e}_Z, \quad \text{with} \quad l^*_n = l + n \times N,\ \Gamma_{l^*_n} = e^{-i\Omega n \Delta c/U}, \tag{2.22}$$

where $\mathrm{M_w}$ is the chord-wise number of the wake vortex rings, and this truncation number can be set as $M_{\mathrm{w}} = 2 \times \max(M, N)$ to model properly the wake influence and avoid unnecessary computation costs.

Summing up Eq.(2.19) and Eq. (2.21) yields

$$\mathbf{V}_b \cdot \mathbf{e}_Z + \mathbf{V}_{\mathrm{w}} \cdot \mathbf{e}_Z = (a_{k1}\Gamma_1 + a_{k2}\Gamma_2 + \cdots + a_{km}\Gamma_m)e^{i\Omega T}, \tag{2.23}$$

where the influence coefficients are given by

$$a_{kl} = \begin{cases} a^*_{kl} & : 1 \le l \le m - N \\ a^*_{kl} + b_{kl} & : m - N + 1 \le l \le m \end{cases} \tag{2.24}$$

The surface velocity can be given by $(0, 0, i\Omega h e^{i\Omega T})$, we then have

$$\mathbf{V}_B \cdot \mathbf{n}_{k,T} = -i\Omega h(X_k, Y_k)e^{i\Omega T}, \tag{2.25}$$

where (X_k, Y_k) indicates the coordinate of the collocation point k.

By considering Eqs. (2.18), (2.23), (2.25), the impermeability condition for the collocation point k reduces to a time-independent linear equation

$$a_{k1}\Gamma_1 + a_{k2}\Gamma_2 + \cdots + a_{km}\Gamma_m = \mathrm{R}_k, \quad k = 1, 2, \cdots, m, \tag{2.26}$$

where the elements of the vector $\mathbf{R}$ are defined as

$$\mathrm{R}_k = i\Omega h(X_k, Y_k) + U\partial_X h(X_k, Y_k), \quad k = 1, 2, \cdots, m. \tag{2.27}$$

Solving the linear system

Eq. (2.26) can be rewritten as

$$M_a \boldsymbol{\Gamma} = \mathbf{R} \tag{2.28}$$

where M_a is the $m \times m$ influence matrix whose element a_{kl} is defined by Eq. (2.24), the vector $\boldsymbol{\Gamma}$ contains the unknown circulations of all vortex rings on the surface, and the elements of $\mathbf{R}$ are defined by Eq. (2.27).

The Eq. (2.28) is time-independent, it needs to be solved only once, and the time-dependent quantities can be obtained by multiplying them with the factor $e^{i\Omega T}$.

Computation of pressure difference distribution

Once the circulation vector $\mathbf{\Gamma}$ is obtained, the pressure distribution can be derived by applying Eq. (2.14) and neglecting the minor terms

$$\Delta p_{ij} = \rho \left(U \frac{\Gamma_{i,j} - \Gamma_{i-1,j}}{\Delta c_{ij}} + i\Omega\Gamma_{ij} \right), \tag{2.29}$$

where Δc_{ij} are the length in the i direction for panel ij. For the panel at the leading edge, the local circulation in Eq. (2.29) will be Γ_{ij} instead of $\Gamma_{i,j} - \Gamma_{i-1,j}$. Similar treatment is applied for the panel at the side edge.

Since the pressure distribution is already obtained, the local or total lift and the moment can be easily calculated.

The advantage of the fixed-frequency lifting-surface method is that the whole computation needs to be executed only once, and therefore it reduces a lot of computational costs compared to the general unsteady lifting-surface method.

2.2.2 Optimization and parallelization of the code

The general principle of the unsteady lifting-surface method remains unchanged, the modifications and optimization introduced in this section will only affect the computational rapidity of the code.

Program algorithm

By observing the Bio-Savart Law (2.4), it is easy to find that apart the factor Γ the vortex induced velocity $\mathbf{V}_{k,l,\Gamma_l}$ depends on the location of the collocation point k relative to the vortex l. Thus, three optimization techniques can be derived:

1. $\mathbf{V}_{k,l,\Gamma_l}$ is completely independent of $\mathbf{V}_{k^*,l^*,\Gamma_{l^*}}$ ($k \neq k^*$ or $l \neq l^*$), such that the different influence coefficient $a(k,l) = \mathbf{V}_{k,l,\Gamma_l} \cdot \mathbf{e}_Z$ can be computed in parallel.

2. If the location of collocation point k^* relative to the vortex l^* is the same as the location of k relative to l, then we have $a(k,l) = a(k^*,l^*)$. This implies that some influence coefficients can be initialized without calculation.

3. Since the two nearby vortex rings share a vortex segment, the influence of this vortex segment will be calculated twice during the calculation of the these two influence coefficients. This redundant computation cost can be removed during the programming.

The vortex influence at collocation point k by the vortex l can be decomposed into four sub-influences (see Eq. 2.6),

$$a_t(k,l) = a_{ab}(k,l) + a_{bc}(k,l) + a_{cd}(k,l) + a_{da}(k,l), \tag{2.30}$$

with

$$a_{ab}(k,l) = \mathbf{V}(P_k, A_l, B_l, \Gamma_l = 1) \cdot \mathbf{e}_Z, \tag{2.31}$$

similar definitions are made for $a_{bc}(k,l), a_{cd}(k,l), a_{da}(k,l)$.

If we consider the influence at the collocation point k by all the vortices (in the ascending order of sequential number l), they can be divided into three categories (see Fig. 2.6): the red vortex owning no shared segment, the green vortices with one shared segment (a leading segment or a side segment), the black vortices with two shared segments (a leading segment and a side segment). Regarding the features 1 and 3, a simple algorithm to calculate the vortex influence at the collocation points indexed from k_s to k_e by all the vortices may be shown in Fig. 2.5.

parallel do $k = k_s, k_e$ Loop to scan the collocation points

The red vortex
$a_t(k,1) = (a_{ab}(k,1) + a_{bc}(k,1) + a_{cd}(k,1) + a_{da}(k,1)$ Segments AB,BC,CD,DA
$a_i(1) = a_{cd}(k,1)$ Store the influence of segment AB of vortex (1,2)
$a_j(1) = a_{da}(k,1)$ Store the influence of segment BC of vortex (2,1)

do $j = 2, N$ The green vortices
$l = j$ The sequential number of vortex (1,j)
$a_t(k,l) = -a_i(1) + a_{bc}(k,l) + a_{cd}(k,l) + a_{da}(k,l)$ Segments BC,CD,DA
$a_i(1) = a_{cd}(k,l)$ Store the influence of segment AB of vortex (1,j+1)
$a_j(j) = a_{da}(k,l)$ Store the influence of segment BC of vortex (2,j)
end do

do $i = 2, M_{\mathrm{w}}$ The green vortices
$l = (i-1)N + 1$ The sequential number of vortex (i,1)
$a_t(k,l) = a_{ab}(k,l) - a_j(1) + a_{cd}(k,l) + a_{da}(k,l)$ Segments AB,CD,DA
$a_i(i) = a_{cd}(k,l)$ Store the influence of segment AB of vortex (i,2)
$a_j(1) = a_{da}(k,l)$ Store the influence of segment BC of vortex (i+1,1)
end do

do $i = 2, M_{\mathrm{w}}$ The black vortices
do $j = 2, N$
$l = (i-1)N + j$ The sequential number of vortex (i,j)
$a_t(k,l) = -a_i(i) - a_j(j) + a_{cd}(k,l) + a_{da}(k,l)$ Segments CD,DA
$a_i(i) = a_{cd}(k,l)$ Store the influence of segment AB of vortex (i,j+1)
$a_j(j) = a_{da}(k,l)$ store the influence of segment BC of vortex (i+1,j)
end do
end do

do $i = M+1, M_{\mathrm{w}}$ Correct with wake vortex strengths, application of Eq.2.17
do $j = 1, N$
$l = (i-1)N + j$
$a_t(k,l) = a_t(k,l) e^{-i\Omega(i-M)\Delta c/U}$
end do
end do

do $l = 1, m$ Initialize the influence coefficients, application of Eq.2.24
if $(k \le m - N)$ *then*
$a(k,l) = a_t(k,l)$
else
$a(k,l) = \sum_{i=0}^{M_{\mathrm{w}}} a_t(k, l^* = l + i \times N)$
end if
end do

end parallel do

Figure 2.5 – Parallel algorithm to calculate the vortex influence.

Using the algorithm of Fig. 2.5, the influence coefficients for the collocation point indexed from k_s to k_e can be calculated in parallel, and the influence of a vortex segment is calculated only once as expected.

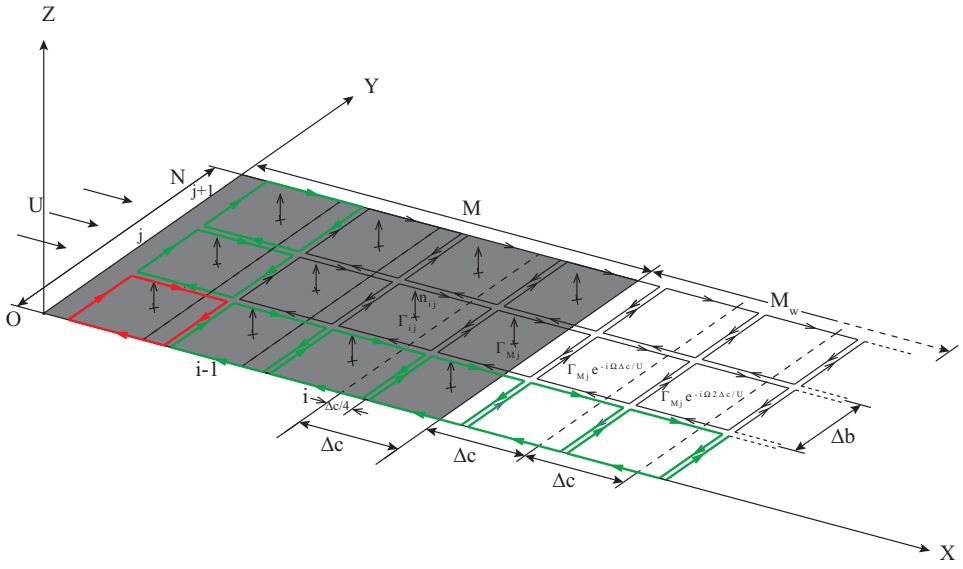

Figure 2.6 – A classification of vortices.

Note that the lifting surface under consideration is rectangular, and the strength of the vortex in a row (same j) are the same during the calculation of the influence coefficients ($\Gamma = 1$), the condition in the feature 2 can be easily met by the span-wise translation of collocation point and the vortex. For example, the velocity at the red point induced by the red vortex ring is equal to the velocity at the blue point due to the blue vortex ring (see Fig. 2.7). A formula about this feature can be obtained:

$$a(k_{i1,j1}, l_{i2,j2}) = a(k_{i3,j3}, l_{i4,j4}), \text{ with } i1 = i3,\ i2 = i4,\ j1 - j3 = j2 - j4 \tag{2.32}$$

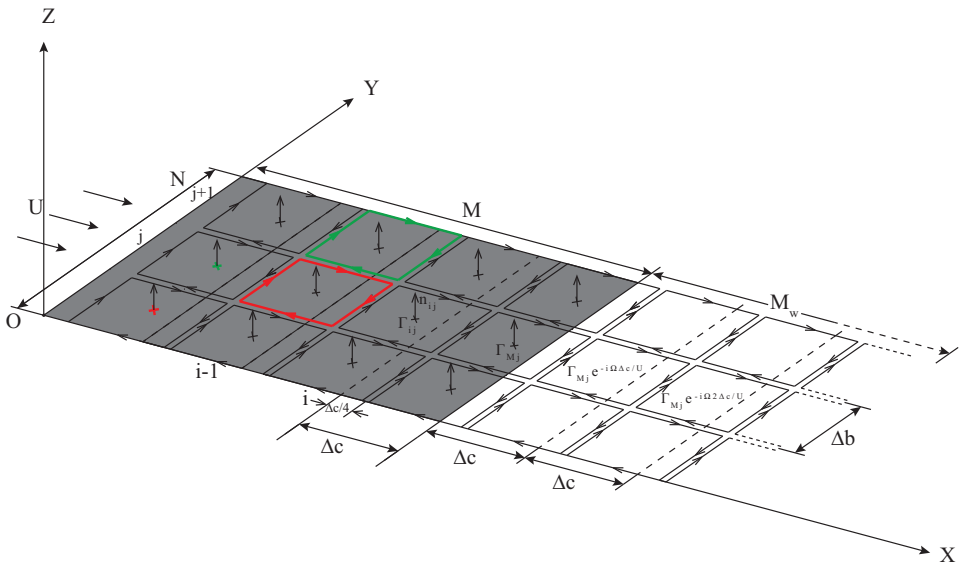

Figure 2.7 – Optimization with translation feature.

Accordingly, an algorithm is derived to initiate the influence coefficients:

```
do i1 = 1, M                    loop to scan the collocation points
    do j1 = 2, N − 1

        k = (i1 − 1)M + j1
        k* = (i1 − 1)M + 1
        k** = (i1 − 1)M + N

        do i2 = 1, M
            do j2 = 1, j1 − 1
                l = (i2 − 1)M + j2
                l** = (i2 − 1)M + j2 − j1 + N
                a(k, l) = a(k**, l**)
            end do
            do j2 = j1, N
                l = (i2 − 1)M + j2
                l* = (i2 − 1)M + j2 − j1 + 1
                a(k, l) = a(k*, l*)
            end do
        end do

    end do
end do
```

Figure 2.8 – Initialization with translation feature.

With the algorithm of Fig. 2.5, the influence coefficients at the collocation point $k_{i,j=1 \text{ or } N}$ can be calculated in parallel. Applying the algorithm of Fig. 2.8, the influence coefficients at the collocation point k (j = from 2 to $N-1$) can be initialized without calculation. Therefore, the computation effort for this section is reduced by a factor of 2/N.

Reflection techniques

In situations where a symmetry exists between the left and right halves of the body's surface, reflection techniques can be applied. This method only reduces the number of unknowns and accelerates the computation, the basic principle of the lifting-surface method remains unchanged.

The lifting surface in Fig. 2.4 is geometrically symmetric between the left and right halves. The lateral velocity of the surface symmetric with respect to the middle chord-line. Hence the symmetric vortex rings will have the same strength

$$\Gamma_{i,j} = \Gamma_{i,N+1-j}, \tag{2.33}$$

or in the sequential number form

$$\Gamma_{(i-1)N+j} = \Gamma_{(i-1)N+N+1-j}. \tag{2.34}$$

In addition, a simple application of Bio-Savart law (2.4) validates the symmetry of the influence coefficient:

$$a_{kl} = a_{k^* l^*}, \tag{2.35}$$

where the asterisk index k^* (or l^*) indicates the image position of the position k (or l^*) according to the left/right symmetry.

Consider the collocation point k, the linear equation (2.26) can be rewritten as

$$\sum_{i=1}^{M} c_i = \mathrm{R}_k, \tag{2.36}$$

where

$$c_i = \sum_{j=1}^{N} a_{kl}\Gamma_l, \quad \text{with} \quad l = (i-1)N + j. \tag{2.37}$$

Using Eq. (2.34) into Eq. (2.37), we obtain a linear equation with $q + r$ unknowns:

$$c_i = \sum_{j=1}^{q}(a_{kl} + a_{kl^*})\Gamma_l + \delta_{1r}a_{k,q+1}\Gamma_{q+1}, \quad \text{with} \quad l = (i-1)N + j,\ l^* = (i-1)N + N + 1 - j, \tag{2.38}$$

in which the number q is the quotient of N with respect to 2, r the corresponding remainder, δ_{1r} the Kronecker delta function.

Now, consider the image collocation point k^* of the collocation point k, the similar results can be obtained:

$$\sum_{i=1}^{M} c_i^* = \mathrm{R}_{k^*}, \tag{2.39}$$

where

$$c_i^* = \sum_{j=1}^{q}(a_{k^*l} + a_{k^*l^*})\Gamma_l + \delta_{1r}a_{k^*,q+1}\Gamma_{q+1}, \quad \text{with} \quad l = (i-1)N + j,\ l^* = (i-1)N + N + 1 - j. \tag{2.40}$$

Note that vector $\mathbf{R}$ is also symmetric according the symmetry of the lateral velocity, comparing Eq. (2.36) and (2.39), using the symmetric relation (2.35), we can find that Eq. (2.36) and (2.39) are the same. So, it is possible to remove the redundant equation (2.39) from the linear system.

From the above optimization, only the left half of surface is modeled, the number of unknown is reduced by a factor of 2. Since much of computational effort is spent on the matrix inversion, which increases at a rate of square of matrix dimension. The use of this reflection techniques can reduce total computation time and the Random-Access Memory by approximately 4.

Program code

The fixed-frequency lifting-surface method is implemented in FORTRAN. The size of the main program is about 500 lines, wherein the parallelization is realized with OpenMP, and the LAPACK Linear Algebra Package is used to solve the linear system. It takes about 2.5 hours to compute a lifting surface problem with a grid including ($M = 80 + M_{\mathrm{w}} = 1600$) $\times$ ($N = 800$) vortex rings on a personal computer with Intel Xeon Processor X5450 (4 cores, 12M Cache, 3.00 GHz, 1333 MHz FSB).

2.3 Validation of the numerical program

In order to validate the numerical program, the lifting surface problem described in the section 1.3 and Fig. 1.9 is considered. The leading edge of the surface is clamped at $X = 0$, while the trailing edge is free at $X = 1$. The aspect ratio of the surface is defined by $A = span/chord = H/L$. The lateral displacement of the surface is prescribed by the natural mode of a clamped-free beam in the vacuo:

$$Z = \cos(KX) + K_2 \sin(KX) + \cosh(KX) - K_2 \sinh(KX), \text{ with } K_2 = \frac{\sin(K) - \sinh(K)}{\cos(K) + \cosh(K)}, \tag{2.41}$$

where

$$K = \begin{cases} 1.8751040687119 & \text{first mode} \\ 4.6940911329742 & \text{second mode} \\ 7.8547574382376 & \text{third mode} \\ \vdots & \vdots \end{cases} \tag{2.42}$$

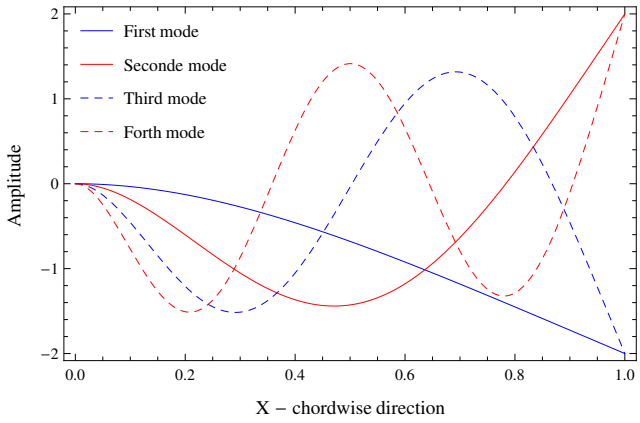

Figure 2.9 – The natural mode envelopes of a clamped-free beam.

The degree of unsteadiness of the problem is defined by the reduced frequency

$$k = \frac{\Omega L}{U}, \tag{2.43}$$

where Ω is the angular frequency, L is the surface semi-chord, and U is the velocity of flow.

The pressures obtained from the numerical program or the analytic theories is normalized by ρU^2:

$$p = \frac{P}{\rho U^2} \tag{2.44}$$

Since in the numerical method there is no any constraint or specific requirement about the lateral displacement (except small amplitude) and the surface geometry, we are going to verify whether the numerical program works correctly with various aspect ratio, reduced frequency, and different displacement envelopes (modes).

2.3.1 Convergence and the influence of wake vortex number

Like other numerical methods, the results of the fixed frequency lifting-surface method depend on the number of discrete elements $M \times N$. But, when the number of vortex rings is sufficiently large, the numerical results should converge and become independent of this number.

To validate the convergence of the numerical method, a lifting surface problem is considered. The aspect ratio is $A = 0.1$, reduced frequency is $k = 0.5$, and lateral displacement is given by the first natural mode of a clamped-free beam.

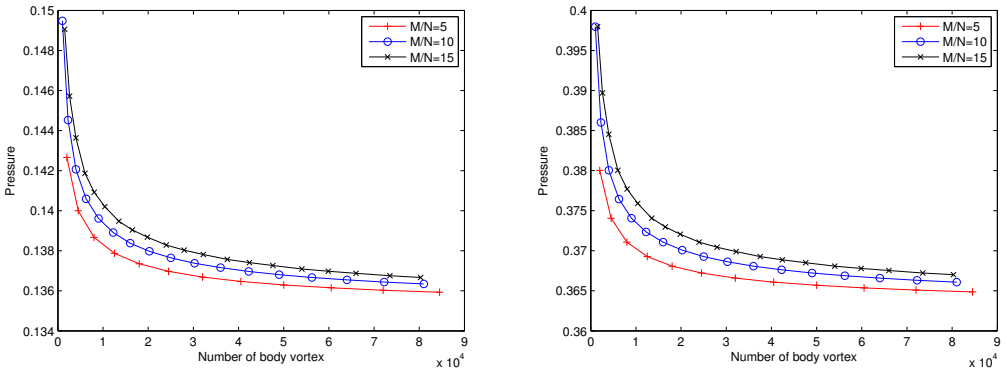

Figure 2.10 – Real and imaginary parts of the span-wise average pressure difference at mid-chord.

The boundary layer is modeled by M chord-wise and N span-wise vortices, the wake is discretized by $M_w = 2M$ chord-wise and N span-wise wake vortices. The real and imaginary parts of the span-wise average pressure at mid-chord $X = 0.5$ are plotted as function of the number of the body vortex $M \times N$ in Fig. 2.10 (three cases are studied: $M/N = 5, 10, 15$).

For any curve in Fig. 2.10, the pressure decreases and converges to a finite value when the number of body vortices increases, this shows a good stability of the numerical program. The pressures given by the three cases are not the same, especially when the number of body vortices is small, but the relative error is within 1%, when the number of body vortex is sufficiently large (for exemple, 8×10^4 in Fig. 2.10). Therefore, it can be said that the three cases converge to the same result, and the numerical program is convergent.

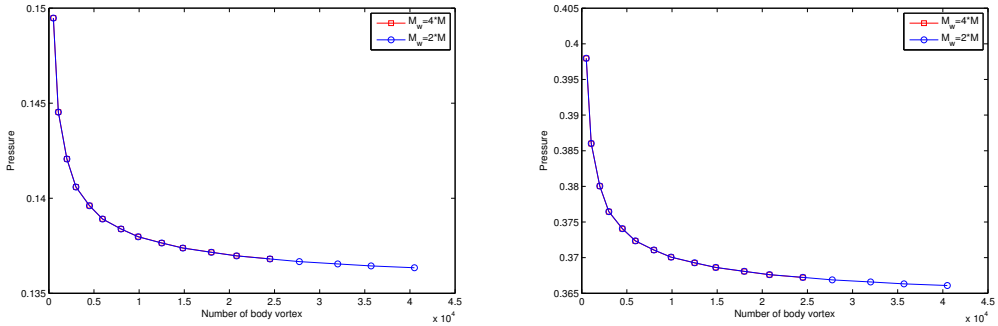

Figure 2.11 – The influence of wake vortex number.

In the numerical program, the chord-wise number of wake vortex M_w is set as $2M$ to precisely model the wake vortex and avoid unnecessary computation costs. However, this is just a empirical value, a dedicated study about the influence of M_w should be performed.

The computation is repeated using almost the same parameters except $M_w = 4M$ and $M/N = 10$, the real and imaginary part of the span-wise average pressure at mid-chord $X = 0.5$ is plotted as a function of the number of the body vortex $M \times N$ in Fig. 2.11.

We find that for any number of body vortices, the results obtained with $M_w = 4M$ are the same as the results obtained with $M_w = 2M$. This means the wake vortices which are further than $M_w = 2M$ play a very minor role on the lifting surface, and it can be neglected in the computation.

2.3.2 Comparison with Slender-body theory

Lighthill's slender-body theory is valid for moving bodies with slender geometry and small lateral motion. By using the concept of added mass, the lift per unit chord length must be equal and opposite to the rate of change of momentum of the added mass in Eq. (1.25). The theoretical average pressure jump can be easily obtained by dividing the lift by the span.

To compare with slender-body theory, a rectangular surface with $A = 0.1$ is considered, as small aspect ratio is required. The boundary layer is represented by $(M = 900) \times (N = 90)$ body vortex rings, and the wake vortex sheet is discretized by $(M_w = 1800) \times (N = 90)$ wake vortex rings.

Firstly, the reduced frequency is set at $k = 0.5$, the lateral displacement is imposed to be the first eigenmode of the clamped-free beam in vacuo. The fixed frequency lifting surface method gives numerically the distribution of vorticity (circulation) and the pressure difference on the surface, and they are plotted in Figs. 2.12 and 2.13, respectively. It can be found that both the vorticity (circulation) and the pressure jump show an elliptical distribution in the spanwise direction, and give zero value at side edges ($Y = 0$ and $Y = 0.1$) (see Fig. 2.14). In Fig. 2.12, the rectangular circle vorticity (circulation) rings are found in the anterior part of surface, this leads to an singularity of pressure jump at the leading edge in Fig. 2.13; the horseshoe vorticity (circulation) rings appear in the posterior part of surface, consequently, zero pressure jump is found at the trailing edge as required by the Kutta condition in Fig. 2.13. The circulation of vorticity rings in the anterior part is positive, while that in the posterior part is negative, this implies that the vorticity rings in the anterior part is in the direction as shown in Fig. 2.4, and the vorticity rings in the posterior part is in the opposite direction.

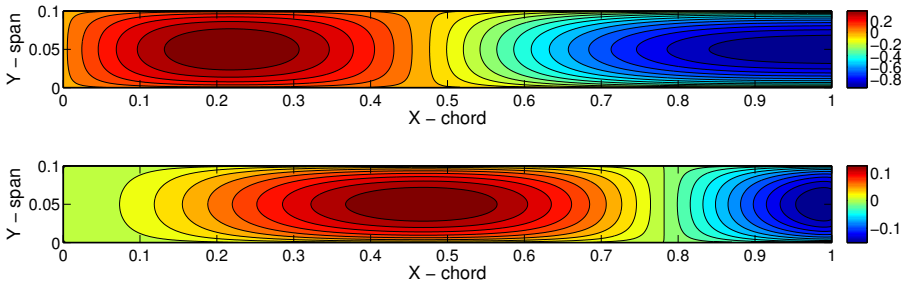

Figure 2.12 – Real and imaginary parts of circulation distribution across a slender surface, $A = 0.1$, $k = 0.5$, first eigenmode.

Now, the span-wise average pressure difference obtained from the numerical program is compared with the pressure difference obtained from the slender-body theory. The complex pressure jump is decomposed into real and imaginary parts, and they are plotted as functions of the chord-wise coordinate in Fig. 2.15.

From Fig. 2.15, it can be seen that the numerical results coincides with the theoretical ones for the most part of the surface. The correctness of the numerical program can be therefore validated. However, the Kutta condition is not satisfied by slender-body theory, and the

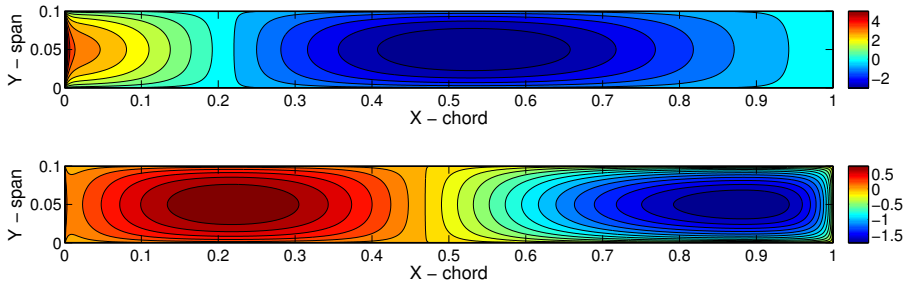

Figure 2.13 – Real and imaginary parts of pressure difference distribution across a slender surface, $A = 0.1$, $k = 0.5$, first eigenmode.

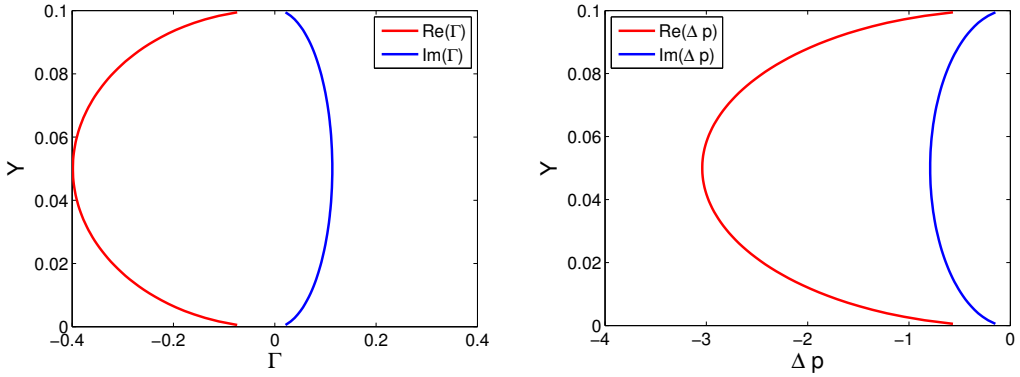

Figure 2.14 – The spanwise distribution of circulation and pressure difference at $X = 0.6$, $A = 0.1$, $k = 0.5$, first eigenmode.

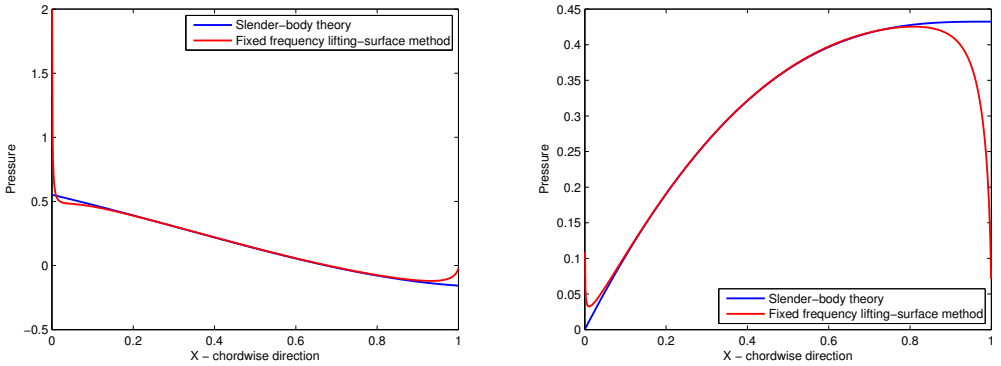

Figure 2.15 – Real and imaginary parts of pressure difference along the chord of a slender surface, $A = 0.1$, $k = 0.5$, first eigenmode.

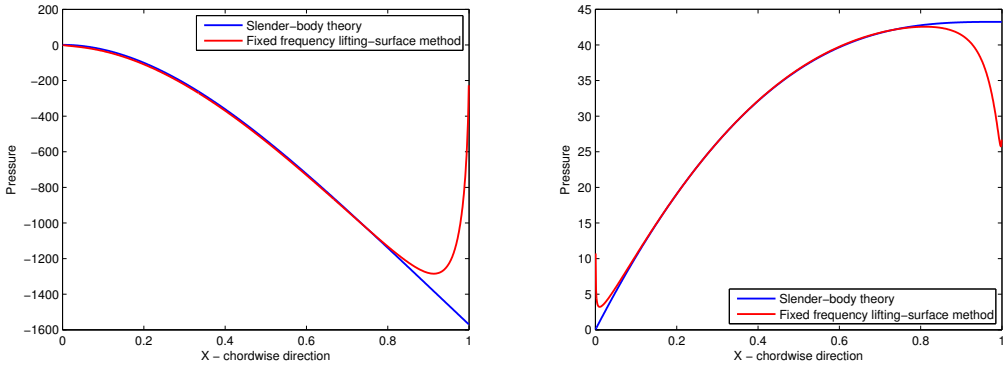

Figure 2.16 – Real and imaginary parts of pressure difference along the chord of a slender surface, $A = 0.1$, $k = 50$, first eigenmode.

leading edge suction effect is not included in this theory. This is why discrepancies occur near the leading and trailing edges. Even though the numerical program gives infinite pressure difference at the leading edge, it remains integrable with respect to the chord coordinate X, and a finite lift per unit span length will be obtained if we calculate the integral of pressure difference from the leading edge $X = 0$ to the trailing edge $X = 1$.

Secondly, we want to see the performance of the numerical program in the domain of high unsteadiness. Hence, the reduced frequency is set at $k = 50$, while the lateral displacement is still prescribed to be the first eigenmode. The real and imaginary parts of pressure difference are plotted with respect to the chord-wise coordinate in Fig. 2.16.

Compared with the results in Fig. 2.15, the pressure difference in Fig. 2.16 is highly increased due to the high unsteadiness. The coincidence between the numerical results and the theoretical ones for the most part of chord validates the correctness of numerical program in the domain of high reduced frequency. The region where a discrepancy exists near the leading edge (or trailing edge) remains almost unchanged, it implies that this discrepancy is independent of the reduced frequency.

Note that the fixed frequency lifting-surface method has been established with an arbitrary small displacement, it should work correctly with different displacement forms, such as lateral translation, rotation, etc. The lateral displacement is now set to be the second mode of a clamped-free beam, while the reduced frequency is $k = 0.5$. The real and imaginary parts of pressure difference with respect to the chord coordinate are plotted in Fig. 2.17.

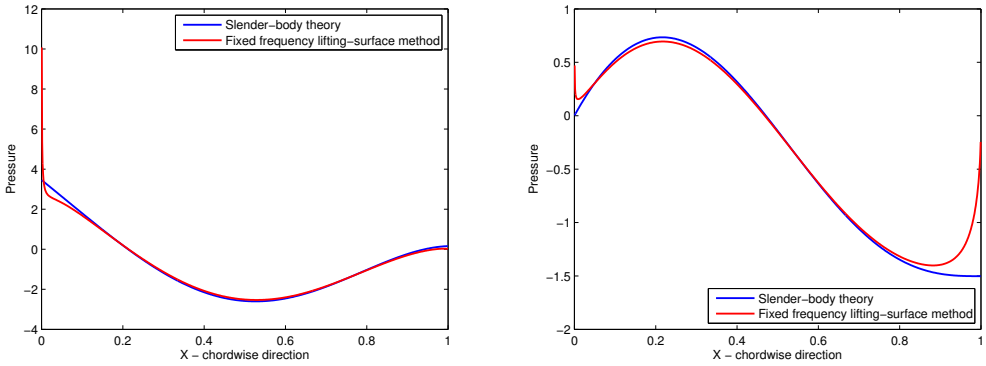

Figure 2.17 – Real and imaginary parts of pressure difference along the chord of a slender surface, $A = 0.1$, $k = 0.5$, second eigenmode.

A good agreement between the numerical results and the theoretical ones for the most part

of chord can be found in Fig. 2.17, and this makes the numerical method applicable for the various displacement form (mode). However, the numerical pressure difference envelope is slightly smaller than the theoretical one, this is because the slender-body theory is the first order approximation, when the wavelength of the deformation becomes smaller (and comparable to the span), the slender-body theory is not valid anymore.

The above various applications has allowed us to confirm that the fixed frequency lifting-surface method can be applied to calculate the pressure difference of a moving surface with small aspect ratio. Moreover, it can include the leading edge singularity and satisfy the Kutta condition at trailing edge. Therefore, compared to the slender-body theory, the fixed frequency lifting-surface method gives more accurate and physical results.

2.3.3 Comparison with 2D unsteady airfoil theory

In the limit of large aspect ratio, the flow is assumed to be almost two-dimensional. Through the formulation in terms of complex acceleration potential and applying the general theory of a oscillating wing, the pressure difference exerted on the surface can be given by a series in which the coefficients are explicitly given (more details can be found in the section 1.2.2).

We consider a rectangular surface with aspect ratio $A = 10$, so that 2D unsteady airfoil theory can be applied. The boundary layer on the surface is divided into $(M = 80) \times (N = 800)$ body vortex rings, while the wake vortex sheet is modeled by $(M_{\mathrm{w}} = 1600) \times (N = 800)$ wake vortex rings.

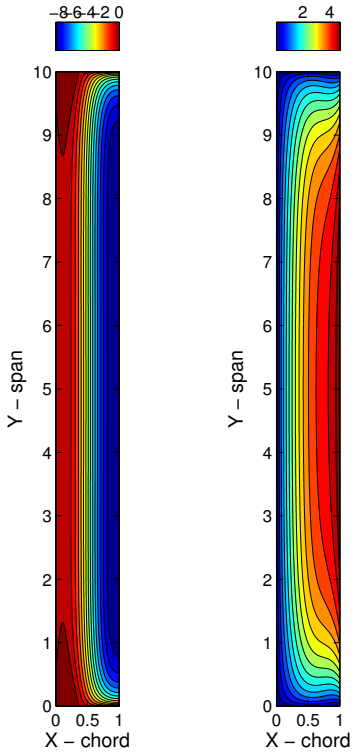

Figure 2.18 – Real and imaginary parts of circulation distribution across a large surface, $A = 10$, $k = 0.5$, first eigenmode.

Firstly, the surface is moving at reduced frequency $k = 0.5$ and with the envelope of first

eigenmode of a clamped-free beam. The vorticity (circulation) and the pressure jump distribution obtained from the numerical code are plotted respectively in Figs. 2.18 and 2.19. In the middle region of surface (far from the leading, trailing and side edges), both the vorticity (circulation) and the pressure jump are almost constant with respect to Y (see Fig. 2.20). As approaching the side edges, the circulation decreases; both the circulation and its X-derivative gives zero value at side edges ($Y = 0$ and $Y = 10$) in Fig. 2.18, consequently, the pressure jump should be zero at side edges in Fig. 2.19. The circulation tends to be zero when approaching the leading edge, but the X-derivative of imaginary part of circulation is non-zero, accordingly, an infinite pressure jump is found at the leading edge in Fig. 2.19. On contrary, for a given Y, when approaching the trailing edge, the circulation tends to be a constant with respect to X and gives a finite value in Fig. 2.18, this makes the Kutta condition satisfied at the trailing edge in Fig. 2.19. Fig. 2.18 clearly shows the horseshoe vorticity rings which is widely applied in the panel method to model the vorticity distribution on the airplane wings. The moving surface is symmetric with respect to the chord-line $Y = 5$, thus the same symmetry can be found for both the circulation and the pressure jump distribution, as expected.

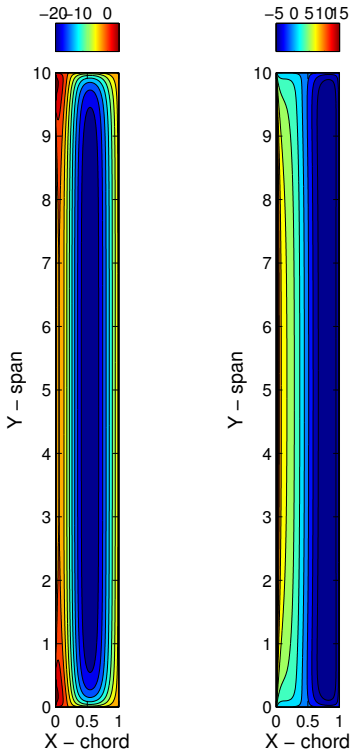

Figure 2.19 – Real and imaginary parts of pressure difference distribution across a large surface, $A = 10$, $k = 0.5$, first eigenmode.

In order to compare with the theoretical results, the span-wise average pressure difference obtained from the numerical code is compared with the pressure obtained from 2D unsteady airfoil theory in Fig. 2.21.

A good agreement between the results from the fixed frequency lifting-surface method and the results from the 2D unsteady airfoil theory is obtained in Fig. 2.21. The Kutta condition is satisfied by both the numerical method and the theoretical one. It seems like the leading edge suction effect does not exist for the imaginary part of pressure difference, but it is just too close to the leading edge and can not be seen Due to the limited chord-wise number of

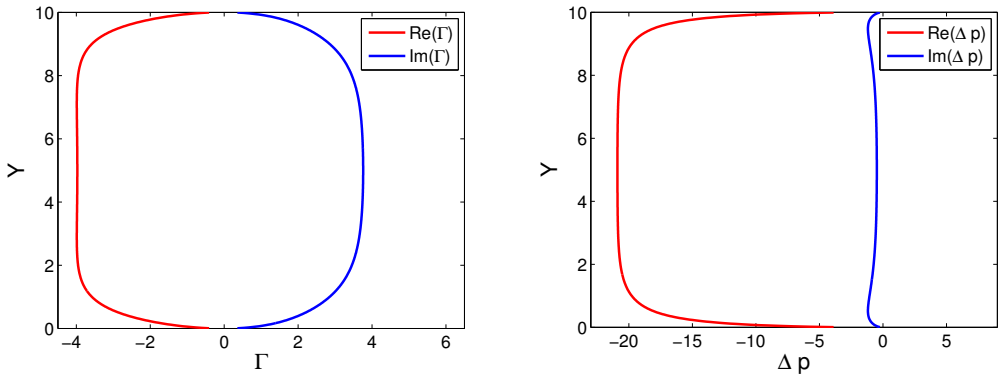

Figure 2.20 – The spanwise distribution of circulation and pressure difference at $X = 0.5$, $A = 10$, $k = 0.5$, first eigenmode.

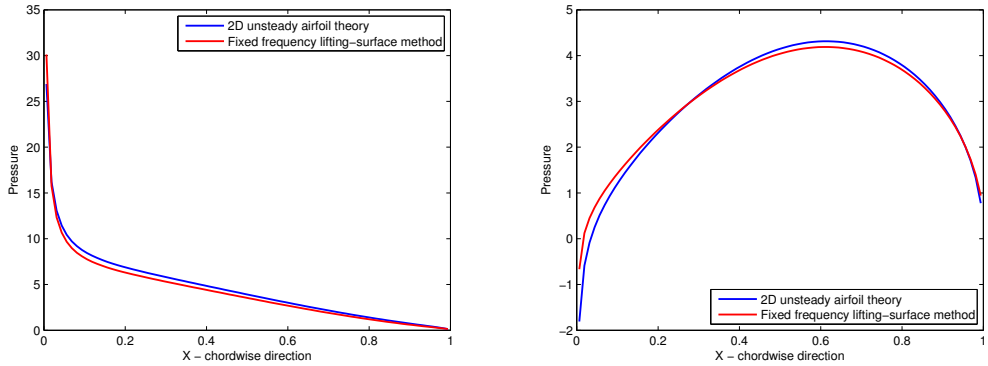

Figure 2.21 – Real and imaginary parts of pressure difference across the chord of a large surface, $A = 10$, $k = 0.5$, first eigenmode.

body vortices ($M = 80$).

Secondly, the surface is now displaced at higher reduced frequency: $k = 50$, while the lateral displacement is still the first mode of a clamped-free beam. Then, the effect of reduced frequency is shown in Fig. 2.22.

Because of a higher reduced frequency, both the numerical results and the theoretical ones are highly increased. The applicability of numerical method for various reduced frequency is confirmed by the relative good agreement. However, the discrepancy becomes larger compared to Fig. 2.21. The Kutta condition is always fulfilled at the trailing edge. Like Fig. 2.16, it seems that the leading edge suction effect only appears for the imaginary part of pressure difference.

Finally, the envelope of motion of the surface is prescribed to be the second mode of a clamped-free beam in the vacuo, while the reduced frequency is set at $k = 0.5$. Then, the performance of numerical method with respect to various deflection forms is shown in Fig. 2.23.

As expected, a good agreement between the numerical results and the theoretical pressures can be found, this also validates that the fixed frequency lifting-surface method is valid for various lateral displacements (mode). Compared to Fig. 2.21, the discrepancy seems unchanged when a different mode is considered. This seems to imply that when different displacement modes are considered, the numerical method gives the results with the same order of approximation.

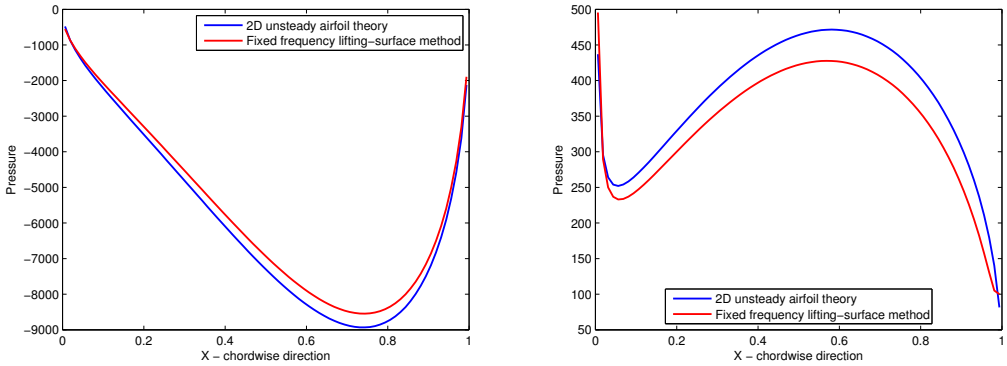

Figure 2.22 – Real and imaginary parts of pressure difference across the chord of a large surface, $A = 10$, $k = 50$, first eigenmode.

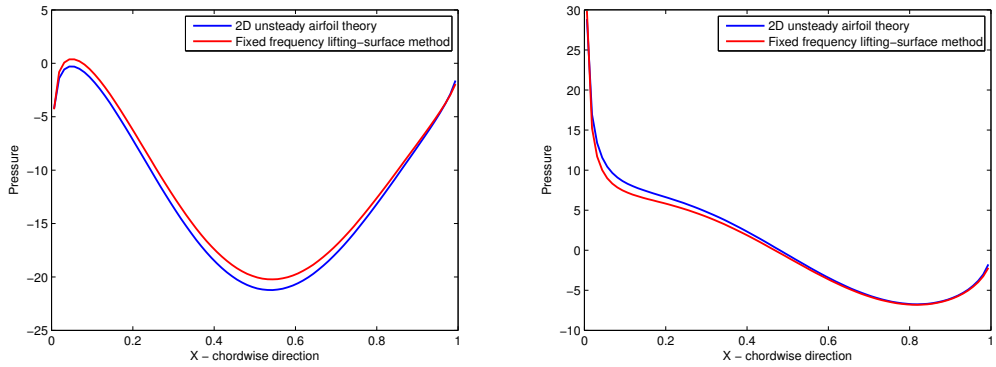

Figure 2.23 – Real and imaginary parts of pressure difference across the chord of a large surface, $A = 10$, $k = 0.5$, second eigenmode.

From the above various applications, we can say that the fixed-frequency lifting-surface method is applicable to model the fluid surrounding a moving surface with small/large aspect ratio. The leading edge suction effect and the trailing edge Kutta condition are naturally included in this numerical method. Noting that the numerical method has no constraint on the aspect ratio, it can be concluded that the fixed frequency lifting-surface method can be applied to calculate the pressure difference exerted by the surrounding fluid on the moving surface for any aspect ratio.

Chapter 3

Theoretical fluid model

The numerical lifting surface method gives the exact distribution of vorticity (circulation) and pressure jump across the moving surface without any approximation, but the computation costs are not always satisfactory. Although we have modified this method and proposed the fixed frequency lifting surface method to avoid the calculation at every time step, the computation cost is still large. This makes it only applicable in the domain where the computation cost is not a constraint, for example the aerospace sector. For the academic research, analytic model is always important as it allows fast computation and gives a physical view of the various quantities.

In this chapter, we consider a surface moving with small amplitude in a uniform, incompressible, potential flow of an inviscid fluid with density ρ. The chord and the span of the surface are $2L$ and $2H$, respectively. The surface is moving at the frequency Ω around the reference plane $Z = 0$ with Z-direction displacement $Z = h_1(X, Y)e^{i\Omega T}$. The projection of the surface and the wake onto the reference plane are respectively S and Σ. (see Fig. 3.1)

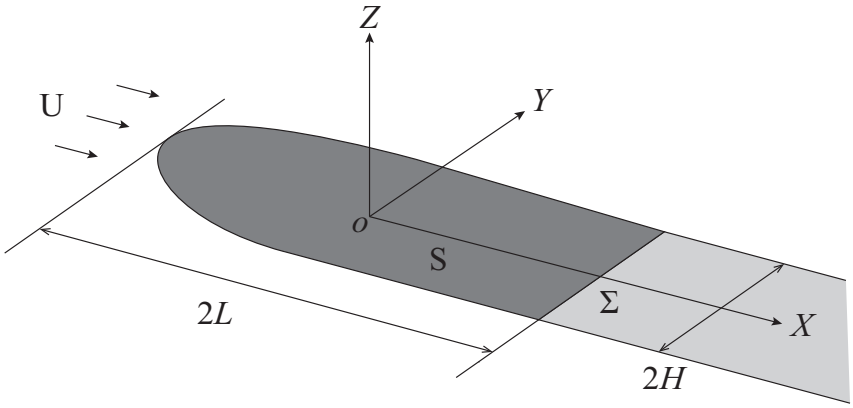

Figure 3.1 – Schematic of a lifting surface problem.

Applying the method introduced in section 1.3, the velocity potential jump $[\Phi]$ is related to the downwash W through a Fredholm integral equation (1.65). The purpose of the next section is to seek the unknown $[\Phi]$ by solving Eq. (1.65) in the asymptotic approximation of small aspect ratio H/L. Once the velocity potential jump $[\Phi]$ is found, the pressure jump can be obtained from the unsteady linearized Bernoulli equation (1.67).

3.1 Asymptotic solution by velocity potential

The asymptotic solution method was firstly used to solve the Fredholm integral equation for a lifting surface with an intermediate aspect ratio by Eloy et al.[23]. This method will be introduced with more details in this section.

Suppose the surface has a small aspect ratio $A = H/L \ll 1$. In order to facilitate the asymptotic sorting and give a clear view of the orders of quantities, the following non-dimensional quantities are defined

$$\begin{aligned} x &= \frac{X_{M_0}}{L}, \quad \xi = \frac{X_M}{L}, \quad y = \frac{Y_{M_0}}{H}, \quad \eta = \frac{Y_M}{H}, \\ [\phi] &= \frac{[\Phi]}{UL}, \quad \mathrm{w} = \frac{\mathrm{W}}{U}, \quad t = \frac{TU}{L}, \quad \omega = \frac{\Omega L}{U}. \end{aligned} \tag{3.1}$$

Considering the above non-dimensional quantities, separating the chordwise and the spanwise integration, we rewrite the Fredholm integral equation (1.65) as

$$\mathrm{w}(x,y) = \frac{A}{4\pi} \fint_{-1}^{1} I(x,\epsilon)\mathrm{d}\eta, \tag{3.2}$$

with

$$I(x,\epsilon) = \fint_{-l^*_{LE}(\eta)}^{\infty} \frac{[\phi](\xi,\eta)}{[(x-\xi)^2+\epsilon^2]^{3/2}}\mathrm{d}\xi, \tag{3.3}$$

where $\epsilon = A(y-\eta)$, and $x = -l^*_{LE}(\eta)$ is the dimensionless local leading edge of surface.

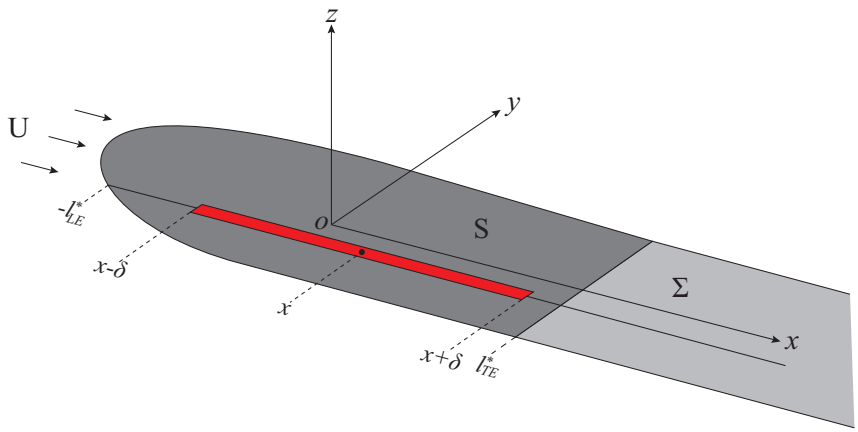

Figure 3.2 – The separation of integral interval. The red segment represents the inner interval, while the rest is the outer interval.

Using the Matched Asymptotic Expansion (MAE) method, we consider an intermediate length parameter δ [31, 37]: $\epsilon \ll \delta \ll 1$, divide the integral (3.3) in two parts (see Fig. 3.2): the inner interval for $|x-\xi| \leq \delta$, and the outer interval for $|x-\xi| > \delta$. For the outer interval, we use an asymptotic expansion $\frac{F_{AE}(\epsilon,x-\xi)}{|x-\xi|^3}$ to represent the kernel function, then the Fredholm integral equation (3.3) can be written as

$$I(x,\epsilon) = I_{in}(x,\epsilon) - I_{outin}(x,\epsilon) + \fint_{-l^*_{LE}(\eta)}^{\infty} \frac{[\phi](\xi,\eta)}{|x-\xi|^3} F_{AE}(\epsilon,x-\xi)\mathrm{d}\xi, \tag{3.4}$$

with

$$\begin{aligned} I_{in}(x,\epsilon) &= \fint_{x-\delta}^{x+\delta} \frac{[\phi](\xi,\eta)}{[(x-\xi)^2+\epsilon^2]^{3/2}}\mathrm{d}\xi, \\ I_{outin}(x,\epsilon) &= \fint_{x-\delta}^{x+\delta} \frac{[\phi](\xi,\eta)}{|x-\xi|^3} F_{AE}(\epsilon, x-\xi)\mathrm{d}\xi, \\ F_{AE}(\epsilon, x-\xi) &= \sum_{n=0}^{N_{AE}} \left[\frac{\epsilon^2}{(x-\xi)^2}\right]^n \frac{\prod_{j=0}^{n}(2j+1)}{(-2)^n n!}, \end{aligned} \tag{3.5}$$

where N_{AE} is a truncation integer number.

Assuming that the potential jump ϕ is as smooth as necessary with respect to chordwise coordinate, it can be approximated by the Taylor series

$$[\phi](\xi,\eta) = \sum_{n=0}^{N_T} \frac{1}{n!}\frac{\partial^n[\phi](x,\eta)}{\partial x^n}(\xi-x)^n + O[(\xi-x)^{N_T}], \quad \text{with} \quad -l_{LE}^*(\eta) < x < l_{TE}^*(\eta), \tag{3.6}$$

where N_T is a truncation integer number for Taylor series.

For a reason that will be evident later, we use $N_T = 4$ for the sake of simplicity. Injecting Eq. (3.6) into Eq. (3.5), and applying the Hadamard finite-part integral definition, $I_{in}(x,\epsilon)$ and $I_{outin}(x,\epsilon)$ can easily be calculated like ordinary integrals, we then have

$$\begin{aligned} I_{in}(x,\epsilon) = {} & \frac{2}{\epsilon^2(1+\epsilon^2/\delta^2)^{1/2}}[\phi](x,\eta) \\ & + \left\{-\frac{2}{(1+\epsilon^2/\delta^2)^{1/2}} + \ln\frac{(1+\epsilon^2/\delta^2)^{1/2}+1}{(1+\epsilon^2/\delta^2)^{1/2}-1}\right\}\frac{\partial^2[\phi](x,\eta)}{\partial x^2 2!} \\ & + \delta^2\left\{\frac{1+3\epsilon^2/\delta^2}{(1+\epsilon^2/\delta^2)^{1/2}} + \frac{3}{2}\frac{\epsilon^2}{\delta^2}\ln\frac{(1+\epsilon^2/\delta^2)^{1/2}-1}{(1+\epsilon^2/\delta^2)^{1/2}+1}\right\}\frac{\partial^4[\phi](x,\eta)}{\partial x^4 4!} + \cdots \end{aligned} \tag{3.7}$$

$$I_{outin}(x,\epsilon) = -\frac{1}{\delta^2}[\phi](x,\eta) + \ln\delta\frac{\partial^2[\phi](x,\eta)}{\partial x^2} + \frac{\delta^2}{4!}\frac{\partial^4[\phi](x,\eta)}{\partial x^4}, \quad \text{for} \quad N_{AE} = 0. \tag{3.8}$$

Noting that $\epsilon^2/\delta^2 \ll 1$, we expand the first term of (3.7) about $\epsilon^2/\delta^2 = 0$ to order $\left[\epsilon^2/\delta^2\right]^{N_{AE}+1}$, the second and third terms to order $\left[\epsilon^2/\delta^2\right]^{N_{AE}}$, $I_{in}(x,\epsilon) - I_{outin}(x,\epsilon)$ then reduces to a Puiseux series

$$I_{in}(x,\epsilon) - I_{outin}(x,\epsilon) = \frac{I_{-2}}{\epsilon^2}[\phi](x,\eta) + I_0\partial_x^2[\phi](x,\eta) + \epsilon^2 I_2\partial_x^4[\phi](x,\eta) + \cdots \tag{3.9}$$

with

$$\begin{aligned} I_{-2} &= 2, \\ I_0 &= -1 - \ln\frac{|\epsilon|}{2}, \\ I_2 &= \frac{5}{48} - \frac{\ln 2}{8} + \frac{\ln|\epsilon|}{8}. \end{aligned} \tag{3.10}$$

Adding Eqs. (3.9) and (3.4), an asymptotic expansion of $I(x,\epsilon)$ can be derived

$$\begin{aligned} I(x,\epsilon) =& \frac{I_{-2}[\phi](x,\eta)}{\epsilon^2} \\ &+ I_0\partial_x^2[\phi](x,\eta) + \oint_{-l^*_{LE}(\eta)}^{\infty} \frac{[\phi](\xi,\eta)}{|x-\xi|^3}\mathrm{d}\xi \\ &+ \epsilon^2\left(I_2\partial_x^4[\phi](x,\eta) - \oint_{-l^*_{LE}(\eta)}^{\infty} \frac{3[\phi](\xi,\eta)}{2|x-\xi|^5}\mathrm{d}\xi\right) + \cdots \end{aligned} \tag{3.11}$$

From the above calculations, we can find that the truncation number N_{AE} of the function F_{AE} can be as big as may be necessary, and if the potential jump $[\phi](\xi,\eta)$ can be accurately approximated by N_T-order Taylor series in Eq. (3.6), the above asymptotic expansion is an exact approximation of $I(x,\epsilon)$ for the interval $-l^*_{LE}(\eta)+A < x < l^*_{TE}(\eta)-A$. Consequently, the solution found by injecting Eq. (3.11) into Eq. (3.2) can fulfill the impermeability condition in this interval.

Rewriting the potential jump as an asymptotic expansion,

$$[\phi](x,y) = [\phi_0](x,y) + [\phi_1](x,y) + [\phi_2](x,y) + \cdots \tag{3.12}$$

where $[\phi_i](x,y)$ is asymptotically small compared to its previous term, considering the original Fredholm integral equation (3.2), Eqs. (3.11) and (3.12), sorting the terms by their orders, then we can write the impermeability condition as

$$\mathrm{w}_n(x,y) = \frac{1}{2\pi A}\oint_{-1}^{1} \frac{[\phi_n](x,\eta)}{(y-\eta)^2}\mathrm{d}\eta,\ n=0,1,2,\cdots \tag{3.13}$$

where

$$\begin{aligned} &\mathrm{w}_0(x,y) = \mathrm{w}(x,y), \\ &\mathrm{w}_1(x,y) = -\frac{A}{4\pi}\oint_{-1}^{1}\left(I_0\partial_x^2[\phi_0](x,\eta) + \oint_{-l^*_{LE}(\eta)}^{\infty}\frac{[\phi_0](\xi,\eta)}{|x-\xi|^3}\mathrm{d}\xi\right)\mathrm{d}\eta, \\ &\quad\vdots \end{aligned} \tag{3.14}$$

Note that the potential jump outside (including) the side edges of surface should be zero

$$[\phi_n](x,y) = 0,\ |y| \geq h^*,\ n=0,1,2,\cdots \tag{3.15}$$

in which the dimensionless local semi-span is defined as $h^* = h(x)/H$.

From the condition (3.15), it follows that

$$\mathrm{w}_n(x,y) = \frac{1}{2\pi A}\oint_{-h^*}^{h^*} \frac{[\phi_n](x,\eta)}{(y-\eta)^2}\mathrm{d}\eta,\ n=0,1,2,\cdots \tag{3.16}$$

And Eq. (3.14) must be evaluated by

$$\begin{aligned} &\mathrm{w}_0(x,y) = \mathrm{w}(x,y), \\ &\mathrm{w}_1(x,y) = -\frac{A}{4\pi}\left(\oint_{-h^*}^{h^*} I_0\partial_x^2[\phi_0](x,\eta)\mathrm{d}\eta + \oint_{-1}^{\infty}\oint_{-h^*(\xi)}^{h^*(\xi)}\frac{[\phi_0](\xi,\eta)}{|x-\xi|^3}\mathrm{d}\xi\mathrm{d}\eta\right), \\ &\quad\vdots \end{aligned} \tag{3.17}$$

An integration by parts of Eq. (3.16) leads to an improper integral in the sense of Cauchy principal value

$$\mathrm{w}_n(x,y) = \frac{1}{2\pi A}\left(\frac{[\phi_n](x,h^*)}{y-h^*} - \frac{[\phi_n](x,-h^*)}{y+h^*}\right) + \frac{1}{2\pi A}\int_{-h^*}^{h^*} \frac{\partial_\eta[\phi_n](x,\eta)}{(\eta-y)}\mathrm{d}\eta,\ n=0,1,2,\cdots \tag{3.18}$$

Because of the condition (3.15), the first term of (3.18) reduces to zero. An simple integration by substitution ($y = h^*y^*,\ \eta = h^*\eta^*$) of the second term of (3.18) results in

$$\mathrm{w}_n(x,y^*h^*) = \frac{1}{2\pi A}\int_{-1}^{1} \frac{\partial_\eta[\phi_n](x,\eta^*h^*)}{(\eta^*-y^*)}\mathrm{d}\eta^*,\ n=0,1,2,\cdots \tag{3.19}$$

where $y^* = Y_{M_0}/h(x)$ and $\eta^* = Y_M/h(x)$ are the non-dimensional variables defined by the characteristic length $h(x)$.

Eq. (3.19) can be regarded as a Carleman type singular integral equation [13], and its solution has been obtained by Estrada et al. [28] and Kanwal [35], as

$$\partial_y[\phi_n](x,y^*h^*) = -\frac{2A}{\pi}\left[\frac{1-y^*}{1+y^*}\right]^{\frac{1}{2}}\int_{-1}^{1}\left[\frac{1+\eta^*}{1-\eta^*}\right]^{\frac{1}{2}}\frac{\mathrm{w}_n(x,\eta^*h^*)}{\eta^*-y^*}\mathrm{d}\eta^* + \frac{C_n}{\sqrt{1-y^{*2}}},\ n=0,1,2,\cdots \tag{3.20}$$

in which the singular integral should be calculated in the sense of Cauchy principal value, the first term and second term correspond respectively to the particular and the homogeneous solution of (3.19), C_n is a constant which can be found by satisfying the condition (3.15).

Now, the procedure to find the n^{th}-order potential jump is:

1. calculate the n^{th}-order downwash w_n using Eq. (3.17),
2. inject w_n into Eq. (3.20),
3. calculate the solution $\partial_y[\phi_n](x,y^*h^*)$,
4. integrate $\partial_y[\phi_n](x,y^*h^*)$ with respect to y and find C_n satisfying (3.15).

The above formulation is valid for any two dimensional displacement. In order to give a clear explanation and an application of this method, we consider a simple case: the prescribed downwash w only depends on x. The derivative of the zeroth order potential jump can be easily obtained from Eq. (3.20) by applying $\mathrm{w}_0 = \mathrm{w}(x)$,

$$\partial_y[\phi_0](x,y^*h^*) = \frac{2A(y^*-1)+C_0}{\sqrt{1-y^{*2}}}\mathrm{w}(x). \tag{3.21}$$

The fulfillment of the boundary condition at the side edges (3.15) results in

$$C_0 = 2A, \tag{3.22}$$

and a simple integration of Eq. (3.21) with respect to y leads to

$$[\phi_0](x,y) = -2A\mathrm{w}(x)\sqrt{h^{*2}-y^2}. \tag{3.23}$$

The dimensionless zeroth order pressure jump across the surface can be obtained by applying the unsteady dimensionless Bernoulli equation

$$[p_0](x,y) = 2(i\omega+\partial_x)(A\mathrm{w}(x)\sqrt{h^{*2}(x)-y^2}), \tag{3.24}$$

and an integration of the above expression from $-h^*$ to h^* gives the dimensionless zeroth order force per unit chord length acting on the fluid

$$f_0(x) = (i\omega + \partial_x)(A\pi h^{*2}(x)\mathrm{w}(x)). \tag{3.25}$$

The corresponding dimensional zeroth order pressure jump and force can be found by multiplying ρU^2 to (3.24) and $\rho U^2 H$ to (3.25)

$$\begin{aligned} [P_0](X,Y) &= 2\rho(i\Omega + U\partial_X)(\mathrm{W}(X)\sqrt{h^2(X) - Y^2}), \\ F_0(X) &= (i\Omega + U\partial_X)(\rho\pi h^2(X)\mathrm{W}(X)). \end{aligned} \tag{3.26}$$

This expression of zeroth order force is equivalent to the result of slender body theory which was found by Lighthill in a different way [46]. The term $\rho\pi h^2(X)$ can be regarded as the added mass or the virtual mass [12] per unit chord length of fluid passing the cross-section S_x. This added mass is the fluid circumscribed by the local span of the moving surface. Consequently, the corresponding momentum in the Z-direction can also be defined as $\rho\pi h^2(X)\mathrm{W}(X)$, and the force per unit chord length exerted on the surrounding fluid by the moving surface must be equal to the rate of change of momentum of the fluid passing S_x.

The current model is thus equivalent to the slender body theory at leading order. But the advantage of this model is that it gives a clear view of the pressure distribution in the spanwise direction, therefore, this model can be viewed as a three-dimensional extension of slender body theory. Moreover, it can be expanded to any order in A.

Injecting the zeroth order potential jump (3.23) into Eq. (3.17), the first order downwash can be derived

$$\mathrm{w}_1(x,y) = -\frac{A^2h^{*2}}{8}\mathrm{w}''(x)\left(2\frac{y^2}{h^{*2}} + 1 + 2\ln\frac{Ah^*}{4}\right) + \frac{A^2h^{*2}}{4}\fint_{-1}^{\infty}\frac{\mathrm{w}(\xi)}{|x-\xi|^3}\mathrm{d}\xi. \tag{3.27}$$

Substituting the above expression into Eq. (3.20), we obtain

$$\partial_y[\phi_1](x, y^*h^*) = \frac{A^3h^{*2}}{2}\frac{1-y^*}{\sqrt{1-y^{*2}}}\left\{\left(y^{*2} + y^* + 1 + \ln\frac{Ah^*}{4}\right)\mathrm{w}''(x) - \fint_{-1}^{\infty}\frac{\mathrm{w}(\xi)}{|x-\xi|^3}\mathrm{d}\xi\right\} + \frac{C_1}{\sqrt{1-y^{*2}}}. \tag{3.28}$$

Integrating this expression with respect to y and noting that the condition (3.15) should be satisfied, we have

$$[\phi_1](x,y) = \frac{A^3h^{*2}}{6}\sqrt{h^{*2}-y^2}\left\{\left(\frac{y^2}{h^{*2}} + 2 + 3\ln\frac{Ah^*}{4}\right)\mathrm{w}''(x) - 3\fint_{-1}^{\infty}\frac{\mathrm{w}(\xi)}{|x-\xi|^3}\mathrm{d}\xi\right\}. \tag{3.29}$$

Applying the dimensionless unsteady Bernoulli equation to the above expression gives the first order dimensionless pressure jump, then integrating this from $-h^*$ to h^*, we obtain the first order force per unit length acting on the fluid

$$f_1(x) = \left(i\omega + \frac{\partial}{\partial x}\right)\left\{\frac{\pi A^3h^{*4}}{4}\left[\left(\ln\frac{4}{Ah^*} - \frac{3}{4}\right)\mathrm{w}''(x) + \fint_{-1}^{\infty}\frac{\mathrm{w}(\xi)}{|x-\xi|^3}\mathrm{d}\xi\right]\right\}. \tag{3.30}$$

Then, the corresponding dimensional first order force is

$$F_1(X) = \left(i\Omega + \frac{\partial}{\partial X}\right)\left\{\frac{\rho\pi h^4}{4}\left[\left(\ln\frac{4}{Ah^*} - \frac{3}{4}\right)\mathrm{W}''(X) + \fint_{-L}^{\infty}\frac{\mathrm{W}(X_M)}{|X-X_M|^3}\mathrm{d}X_M\right]\right\}. \quad (3.31)$$

According to the Hardamard finit-part integral definition, the second term of (3.30) is evaluated as

$$\fint_{-1}^{\infty}\frac{\mathrm{w}(\xi)}{|\xi-x|^3}\mathrm{d}\xi = \int_{-1}^{1}\frac{\mathrm{w}(\xi)-\mathrm{w}_{dec}(\xi,x)}{|\xi-x|^3} + \fint_{-1}^{1}\frac{\mathrm{w}_{dec}(\xi,x)}{|\xi-x|^3}\mathrm{d}\xi + \int_{1}^{\infty}\frac{\mathrm{w}(1)e^{i\omega(1-\xi)}}{(\xi-x)^3}\mathrm{d}\xi, \quad (3.32)$$

where

$$\mathrm{w}_{dec}(\xi,x) = \mathrm{w}(x) + \mathrm{w}'(x)(\xi-x) + \frac{\mathrm{w}''(x)}{2}(\xi-x)^2. \quad (3.33)$$

The first order force (3.31) is different from the result obtained by Eloy [23] for a surface with the variant local span, since the coefficient Ah^* of the first term in (3.31) represents the ratio of the local semi-span to the semi-chord, that is h/L,while this coefficient in [23] refers to H/L.

By observing the asymptotic solution (3.26), it can be seen that the zeroth order force $F_0(X)$ is generated only due to the local perturbation velocity $\mathrm{W}(X)$ and the local span $h(X)$. Thus, the zeroth order forces F_0 is independent of the surface geometry. All above observations are consistent with the assumptions of slender body theory. However, the leading edge suction and the influence of the wake through the Kutta condition depend on the surface geometry, that explains why these two effect are not included in the zeroth order force $F_0(X)$.

The first order force F_1 at x depends not only on the local characteristic (such as $\mathrm{W}''(X)$ and $h(X)$) of the moving surface, but also the global characteristic due to the last term in (3.31). This makes it completely different from Slender body theory [46] which is derived from the two-dimensional flow resulted from the motion of an infinite cylinder C_X.

3.2 Results and discussions

To validate the asymptotic solutions (3.26, 3.31), a rectangular surface moving in a stream directed in the x positive direction is considered, as it was done in chapter 2 on the numerical model. The leading edge is clamped at $x = -0.5$, while the trailing edge is free at $x = 0.5$. The half-span is H. The lateral displacement is prescribed by the natural modes of a clamped-free beam in vacuo. For convenience, all the forces below are normalized by $\rho\pi U^2H^2$. The numerical results below are calculated with the fixed frequency lifting surface method as exposed in previous chapter. We use square vortex ring elements: if the aspect ratio of the considered surface is A, the chordwise vortex number is M, then the spanwise vortex number is about $M \times A$ and the chordwise wake vortex number is $2M$.

First, the aspect ratio of the moving surface is $A = 0.1$, the lateral displacement is the first beam eigenmode, and the reduced frequency is $k = 0.5$. The real and imaginary parts of the force per unit chord length are plotted with respect to the chordwise coordinate.

Since the zeroth order force is equivalent to slender body theory, the results derived from Slender body theory and the zeroth order force are the same and marked by the legend 'Slender Body Theory'. The total force obtained from the asymptotic solution at next order is $F_0 + F_1$, and marked by 'Asymptotic solution'. Due to the corrective force F_1,

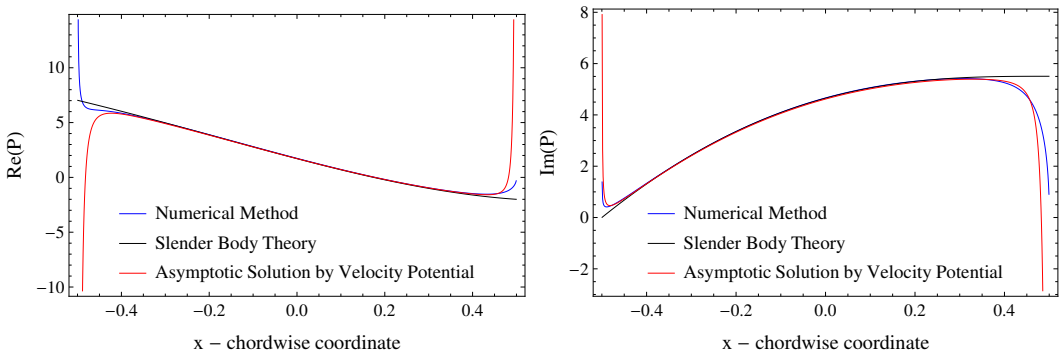

Figure 3.3 – Real and imaginary parts of the force per unit chord length, $A = 0.1$, $k = 0.5$, first beam eigenmode.

the total theoretical force gives more accurate results compared to Slender body theory for $-0.4 < x < 0.4$, but as x approaches the leading edge or trailing edge, the total force diverges to $\pm\infty$ due to the second and third term of (3.32).

In fact, to evaluate the velocity at the location x induced by the potential jump, only the potential jump in the vicinity should be accounted for, since the potential jump which is far away from the location x has very minor effect, this is validated by the study of the influence of wake sheet length in the section 2.3.1. Thus, when we attempt to calculate an asymptotic expansion of $I(x, \epsilon)$, it is logical to evaluate the integral in Eq. (3.3) only over the interval $x - \delta < \xi < x + \delta$ to derive the dominant term. However, as x approaches the leading edge, this interval will exceed the leading edge, the dominant term should be derived from the definite integral of the product of kernel function and potential jump on the surface over the interval $-l^*_{LE} < \xi < x + \delta$ (see Fig. 3.4). When x is in the vicinity of trailing edge, the dominant term should be sum of the definite integral of the product of kernel function and potential jump on the surface over the interval $x - \delta < \xi < l^*_{TE}$ and the definite integral of the product of kernel function and potential jump in the wake over the interval $l^*_{TE} < \xi < x + \delta$ (see Fig. 3.5). This difference between the asymptotics and the original lifting-surface equation explains the existence of pressure singularity at the leading and trailing edges.

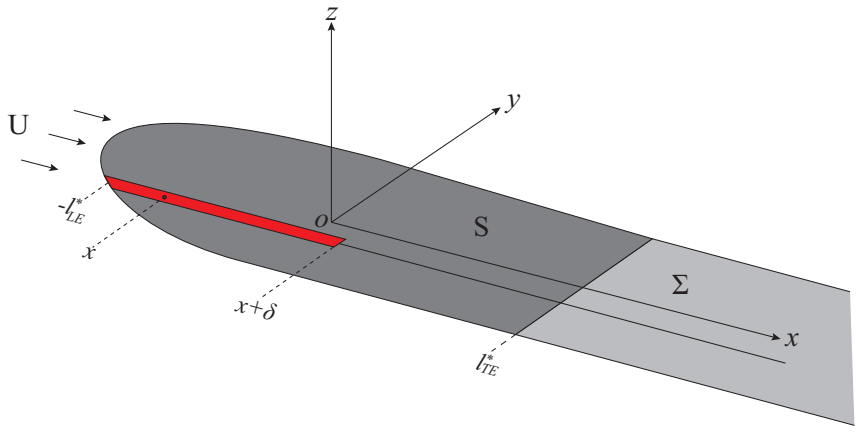

Figure 3.4 – The asymptotic sorting near the leading edge. The red segment implies that the body type potential jump should be used to calculate dominant term in (3.11).

Since the potential jump before the leading edge and the potential jump in the wake plays a minor role on the moving surface in the limit of small aspect ratio, the absence of the special treatments presented in the previous paragraph will not bring any problem. This explains why Slender body theory and the zeroth order force are valid for small aspect ratio.

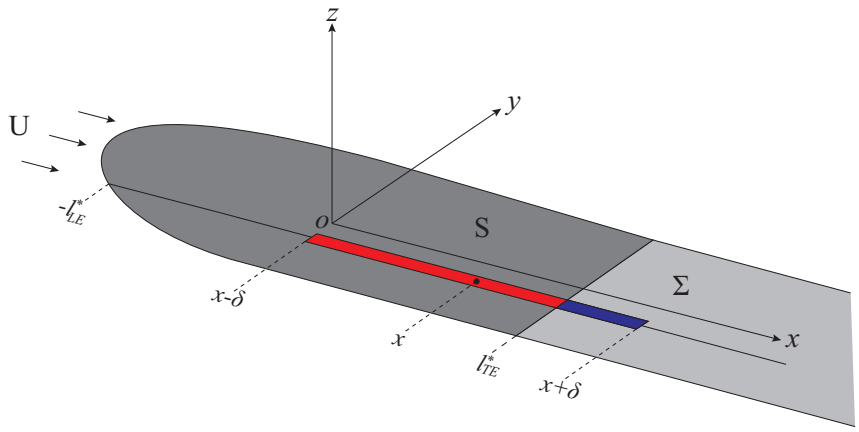

Figure 3.5 – The asymptotic sorting near the trailing edge. The body potential jump should be used for the red segment, while the potential jump in the wake should be employed for the blue segment.

From Eq. (3.4-3.11), we can find that the potential jump before the leading edge (from $x = -\infty$ to $x = -l^*_{LE}$) and the potential jump in the wake (from $x = l^*_{TE}$ to $x = \infty$) are treated as the potential jump on the surface during the calculation of the first, second, and fourth term of (3.11), while the real physical potential jump is applied to derive the third and fifth term of (3.11). This contradiction maybe explains the divergence of the total force near the leading or trailing edge. In addition, F_1 is evaluated from F_0, the failure of zero order force F_0 near the leading edge (or trailing edge) may make F_1 worse.

From the above analysis, the reason for the failures of the total force near the leading edge and trailing edge may be clear. It can be found that some components of the total force $F_0 + F_1$ tends to infinity when x approaches the leading edge (or trailing edge). If we can eliminate these infinite components, a better result could be found.

Now, we need to identify the components which tends to infinity. Expanding the first order force F_1 at the trailing edge and at the leading edge up to order 0 yields

$$\begin{aligned} F^*_{TE}(x) &= \rho\pi U^2 H \left[\frac{A^{TE}_{-2}}{(1-x)^2} + \frac{A^{TE}_{-1}}{1-x} + A^{TE}_0 \ln(1-x) + C_{TE} + O(1-x) \right], \\ F^*_{LE}(x) &= \rho\pi U^2 H \left[\frac{A^{LE}_{-2}}{(1+x)^2} + \frac{A^{LE}_{-1}}{1+x} + A^{LE}_0 \ln(1+x) + C_{LE} + O(1+x) \right]. \end{aligned} \tag{3.34}$$

The coefficients $A^{TE}_{\cdots}$, $A^{LE}_{\cdots}$, C_{TE} and C_{LE} in the above Puiseux series can be easily obtained from a symbolic calculation software, like Mathematica. The Kutta condition could be met at the trailing edge and the infinite first order force at the leading edge could be smoothed out by rewriting the total force as

$$F_{total}(x) = F^*_{LE}(x + \epsilon_{LE}) - F^*_{LE}(x) + F_0(x) + F_1(x) - F^*_{TE}(x) + F^*_{TE}(x + \epsilon_{TE}), \tag{3.35}$$

in which the forces are expressed in the non-dimensional coordinate x. This is equivalent to placing the singularities at $-\frac{1}{2} - \epsilon_{LE}$ and $\frac{1}{2} + \epsilon_{TE}$, out of the interval considered $-\frac{1}{2} < x < \frac{1}{2}$. The parameters ϵ_{LE} and ϵ_{TE} are small real numbers and can be derived by solving the implicit equations

$$\begin{aligned} F^*_{LE}(1 + \epsilon_{LE}) &= 0, \\ F^*_{TE}(1 + \epsilon_{TE}) + F_0(1) &= 0. \end{aligned} \tag{3.36}$$

Only the force near the trailing edge and the leading edge will be changed because the parameters ϵ_{TE} and ϵ_{LE} are small. From now on, the total force derived from Eq. (3.35) is denoted by the 'Modified Asymptotic Solution by Velocity Potential (ASVP)'. If we consider a surface with aspect ratio $A = 0.1$, moving with first beam eigenmode at reduced frequency $k = 0.5$, the results of modified asymptotic solution by velocity potential are shown below

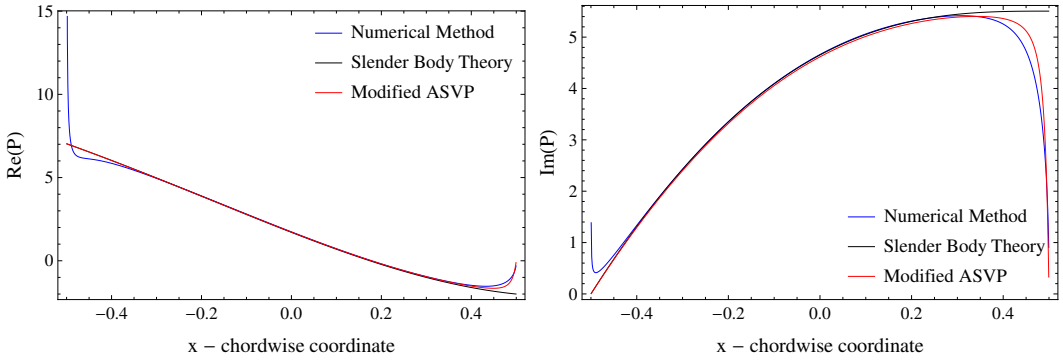

Figure 3.6 – Real and imaginary parts of the force per unit chord length, $A = 0.1$, $k = 0.5$, first beam eigenmode.

From Fig. 3.6, it can be seen that the Kutta condition is satisfied at the trailing edge by the modified asymptotic solution by velocity potential, and consequently the force near the trailing edge shows a better agreement with the numerical result. Near the leading edge, the modified ASVP gives almost the same results as those of Slender body theory. As the aspect ratio of the considered surface becomes larger, the effect of leading edge suction and Kutta condition on the pressure distribution across the surface becomes more important, and hence the modified asymptotic solution by velocity potential should give better results than Slender body theory for the intermediate aspect ratio.

To show the performance of the modified asymptotic solution by velocity potential, we consider a moving surface with a larger aspect ratio $A = 0.3$, the lateral displacement is imposed to be the first beam eigenmode, and the reduced frequency is $k = 0.5$. As usual, the force per unit chord length is plotted with respect to the chordwise coordinate x in Fig. 3.7.

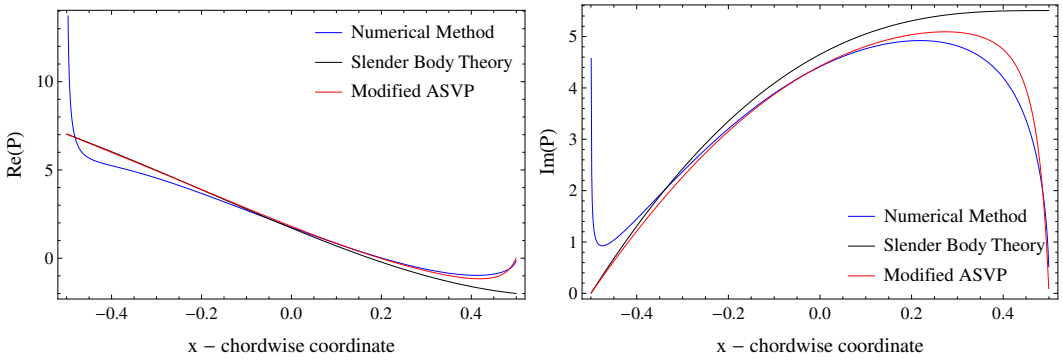

Figure 3.7 – Real and imaginary parts of the force per unit chord length, $A = 0.3$, $k = 0.5$, first beam eigenmode.

Since the surface under consideration is no longer slender, the failures of Slender body theory near the trailing edge and leading edge become worse. However, the modified asymptotic solution by velocity potential gives better results for the posterior part from $x = 0$ to $x = 0.5$, and almost the same results for the anterior part from $x = -0.5$ to $x = 0$, compared to the Slender body theory.

Now, let us reconsider the same surface, but this time with a larger reduced frequency $k = 50$. The corresponding results are shown in Fig. 3.8.

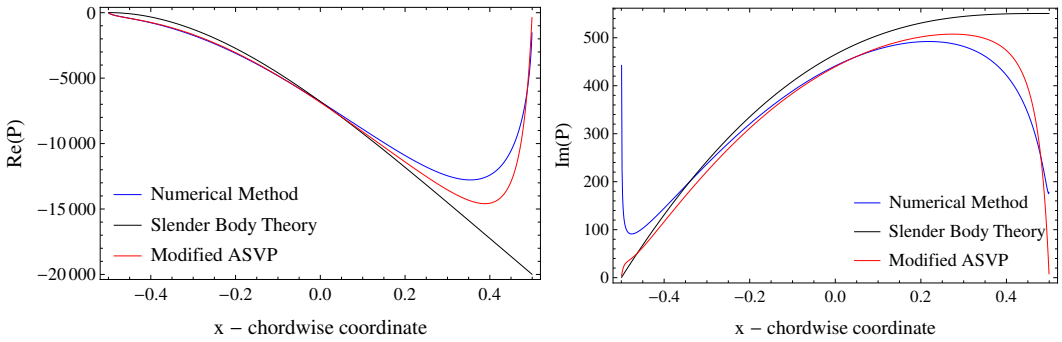

Figure 3.8 – Real and imaginary parts of the force per unit chord length, $A = 0.3$, $k = 50$, first beam eigenmode.

It seems that the effect of leading edge becomes less important due to the large reduced frequency. Although the real and imaginary parts of force become larger than the case $k = 0.5$, the relative error between the numerical results and the results from the modified asymptotic solution by velocity potential remains unchanged. This validates the applicability of the modified ASVP for different reduced frequency.

Finally, we consider a moving surface with the same aspect ratio $A = 0.3$ and a reduced frequency $k = 0.5$, but the lateral displacement is now prescribed to be the second beam eigenmode. The corresponding results are shown in Fig. 3.9. We can find that the envelope of result given by the modified ASVP is much closer to the numerical results than that of Slender body theory. In fact, the lateral displacement being imposed by the second beam eigenmode implies that the displacement varies more along the chord and its derivative with respect to x is bigger than that of the first beam eigenmode. Hence, the potential jump varies more, and it requires a higher order Taylor series to make an accurate approximation as shown in Eq. (3.6). Consequently, the modified asymptotic solution by velocity potential resulting from a second order Taylor series is more accurate than Slender body theory. But this means that if the surface is moving with the third or forth eigenmode, a higher order result may be necessary. Note that, for the second beam eigenmode the Kutta condition is still met at the trailing edge by the modified ASVP, while near the leading edge, the modified asymptotic solution by velocity potential gives almost the same results as the Slender body theory.

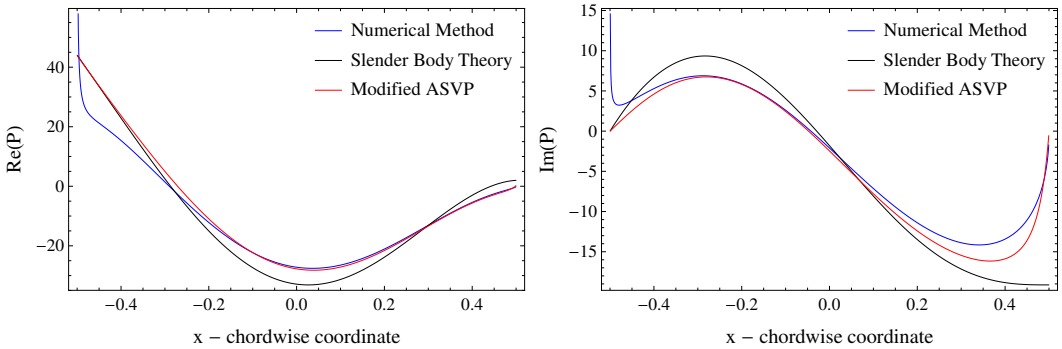

Figure 3.9 – Real and imaginary parts of the force per unit chord length, $A = 0.3$, $k = 0.5$, second beam eigenmode.

From the above applications, we can conclude that the modified asymptotic solution by velocity potential can model the flow around a surface with intermediate aspect ratio, which is moving with an arbitrary lateral deflection of small amplitude. The modified asymptotic

solution by velocity potential can satisfy the Kutta condition at the trailing edge, and as the first asymptotic solution, it gives more accurate result than Slender body theory. As a theoretical model, it take only a little symbolic calculation effort to obtain the force exerted on the surface. All these advantage makes it a a good candidate for optimization or control.

3.3 Asymptotic solution by acceleration potential

The general formulation of a lifting problem can be achieved through the lifting surface integral which relates the perturbation velocity W to the unknown velocity potential jump $[\Phi]$, as introduced in the section 1.3. With the same perturbation method, it is possible to model the lifting problem by a lifting surface integral expressed in terms of the pressure jump (or acceleration jump).

We define the acceleration potential as

$$\Psi = -\frac{P}{\rho}, \tag{3.37}$$

where P is the perturbation pressure. Noting the linearized Bernoulli law which relates the velocity to the pressure, the following equation can be easily derived (see Eq. 1.28)

$$\Psi = D(\Phi), \quad \text{with} \quad D = i\Omega + U\partial_X \tag{3.38}$$

Noting that the flow field is modeled by Eq. (1.59), an application of D-operator to Eq. (1.59) gives the governing PDE system in terms of acceleration potential Ψ (see Eqs. 1.32,1.33, and 1.38)

$$\Delta\Psi(P) = 0, \quad \text{with} \quad \partial_Z\Psi(M_0) = D(\mathrm{W}(M_0)), \tag{3.39}$$

in which P represents an arbitrary point located in the flow domain outside the moving surface and the wake, M_0 is a point on the surface, and the perturbation velocity of surface is $W(M_0)$.

As in section 1.3 for the velocity potential, the solution of Eq. (3.39) can be easily found by means of Green's representation theorem [53], and the fulfillment of Neumann boundary condition can be achieved by applying the Z-derivative operator to Ψ and taking the limit as Z_P tends to zero. Then the lifting surface integral is established in terms of acceleration potential jump as

$$D(\mathrm{W}(M_0)) = \oint\!\!\!\!\!\!\int_S [\Psi](M)F(|MM_0|)\mathrm{d}S_M, \tag{3.40}$$

where $[\Psi](M)$ is the jump of acceleration potential across S, and F is the kernel function

$$[\Psi](M) = \Psi(X_M, Y_M, 0^+) - \Psi(X_M, Y_M, 0^-), \tag{3.41}$$

$$F(|MM_0|) = \frac{1}{4\pi|MM_0|^3}. \tag{3.42}$$

Note that the integral must be taken over S only in Eq. (3.40) and not $S + \Sigma$ as in Eq. (1.65), because the jump of jump of acceleration potential is zero at the trailing edge and in the wake.

Once the solution of Eq. (3.40) is found, the aerodynamic load can be easily calculated. However, just like Eq. (1.65), there is not a general method to solve this Fredholm integral equation (3.40). Thus, we seek an asymptotic solution instead.

Now, we restrict the moving surface to be rectangular surface whose chord is aligned in the streamwise direction. The half-chord is L, and H is the half-span, hence, the aspect ratio is $A = H/L$. In order to facilitate the solving procedure, the following non-dimensional variables are defined:

$$\begin{aligned} x &= \frac{X_{M_0}}{L}, \quad \xi = \frac{X_M}{L}, \quad y = \frac{Y_{M_0}}{H}, \quad \eta = \frac{Y_M}{H}, \\ [\psi] &= \frac{[\Psi]}{U^2}, \quad \mathrm{w}^* = \frac{D(\mathrm{W})L}{U^2}, \quad t = \frac{TU}{L}, \quad \omega = \frac{\Omega L}{U}. \end{aligned} \tag{3.43}$$

Separating the chordwise integration and the spanwise integration in Eq. (3.40), we have

$$\mathrm{w}^*(x,y) = \frac{A}{4\pi} \fint_{-1}^{1} I(x,\epsilon)\mathrm{d}\eta, \tag{3.44}$$

with

$$I(x,\epsilon) = \fint_{l_{LE}^*}^{l_{TE}^*} \frac{[\psi](\xi,\eta)}{[(\xi-x)^2+\epsilon^2]^{3/2}}\mathrm{d}\xi, \tag{3.45}$$

where $\epsilon = A(\eta - y)$, $l_{LE}^* = -1$ and $l_{TE}^* = 1$ are the dimensionless leading edge and trailing edge of surface, respectively. Note that Eqs. (3.2,3.3) are very similar to Eqs. (3.44,3.45). Now, we will use similar methods as the ones used in section 3.1 to solve this inverse integral problem.

Assume $[\psi](\xi,\eta)$ is analytic with respect to ξ, it can be approximated by a Taylor series

$$[\psi](\xi,\eta) = [\psi](x,\eta) + \partial_x[\psi](x,\eta)(\xi - x) + \cdots \tag{3.46}$$

Applying it to Eq. (3.45) leads to

$$\begin{aligned} I(x,\epsilon) =& \frac{1}{\epsilon^2}\left(\frac{x - l_{LE}^*}{[(x-l_{LE}^*)^2+\epsilon^2]^{1/2}} + \frac{l_{TE}^* - x}{[(l_{TE}^*-x)^2+\epsilon^2]^{1/2}}\right)[\psi](x,\eta) \\ &+ \left(\frac{1}{[(x-l_{LE}^*)^2+\epsilon^2]^{1/2}} - \frac{1}{[(l_{TE}^*-x)^2+\epsilon^2]^{1/2}}\right)\partial_x[\psi](x,\eta) + \cdots \end{aligned} \tag{3.47}$$

Suppose the acceleration jump can be expressed by an asymptotic expansion

$$[\psi](\xi,\eta) = [\psi_0](x,\eta) + [\psi_1](x,\eta) + \cdots \tag{3.48}$$

where $[\psi_i](x,\eta)$ is asymptotically small compared to its previous term. Considering Eqs. (3.40), (3.47) and (3.48), we obtain a triangular system

$$\begin{aligned} \mathrm{w}_n^*(x,y) = \frac{1}{4\pi A} \fint_{-1}^{1} \frac{1}{(\eta-y)^2}\Bigg(&\frac{x - l_{LE}^*}{[(x-l_{LE}^*)^2 + A^2(\eta-y)^2]^{1/2}} \\ &+ \frac{l_{TE}^* - x}{[(l_{TE}^*-x)^2 + A^2(\eta-y)^2]^{1/2}}\Bigg)[\psi_n](x,\eta)\mathrm{d}\eta, \ n = 0,1,\cdots \end{aligned} \tag{3.49}$$

with

$$\begin{aligned}
\mathrm{w}_0^*(x,y) &= \mathrm{w}^*(x,y),\\
\mathrm{w}_1^*(x,y) &= -\frac{A}{4\pi}\fint_{-1}^{1}\left(\frac{1}{[(x-l_{LE}^*)^2+A^2(\eta-y)^2]^{1/2}}\right.\\
&\qquad\left.-\frac{1}{[(l_{TE}^*-x)^2+A^2(\eta-y)^2]^{1/2}}\right)\partial_x[\psi_0](x,\eta)\mathrm{d}\eta,\\
&\vdots
\end{aligned} \tag{3.50}$$

An integration by parts of Eq. (3.49) with respect to η yields

$$\mathrm{w}_n^*(x,y) = \frac{-1}{4\pi A}\frac{b}{\eta-y}[\psi_n](x,\eta)\Big|_{-1}^{1} + \frac{1}{4\pi A}\int_{-1}^{1}\frac{b}{\eta-y}\partial_\eta[\psi_n](x,\eta)\mathrm{d}\eta, \tag{3.51}$$

with

$$b = \frac{[(x-l_{LE}^*)^2+A^2(\eta-y)^2]^{1/2}}{x-l_{LE}^*} + \frac{[(l_{TE}^*-x)^2+A^2(\eta-y)^2]^{1/2}}{l_{TE}^*-x}. \tag{3.52}$$

Note that the pressure jump should be zero at the side edges

$$[\psi_n](x,-1) = [\psi_n](x,1) = 0. \tag{3.53}$$

Eq. (3.51) is consequently reduced to

$$\mathrm{w}_n^*(x,y) = \frac{1}{4\pi A}\int_{-1}^{1}\frac{b}{\eta-y}\partial_\eta[\psi_n](x,\eta)\mathrm{d}\eta. \tag{3.54}$$

Due to the factor b, Eq. (3.54) can not be solved with Carleman inversion formula (3.20). However, the improper integral in Eq. (3.54) is evaluated as Cauchy principal value, and it can be regarded as the signed area of the region that is bounded by $b\partial_\eta[\psi](x,\eta)/(\eta-y)$, the x-axis and the horizontal lines $\eta=-1$ and $\eta=-1$. Therefore, rewrite $\partial_\eta[\psi_n](x,\eta)$ as

$$\partial_\eta[\psi_n](x,\eta) = \partial_\eta[\psi_n^*](x,\eta)/b^*, \tag{3.55}$$

with

$$b^* = \frac{[(x-l_{LE}^*)^2+A^2/4]^{1/2}}{x-l_{LE}^*} + \frac{[(l_{TE}^*-x)^2+A^2/4]^{1/2}}{l_{TE}^*-x}, \tag{3.56}$$

where the factor $1/4$ is evaluated as the average of $(\eta-y)^2$ with respect to η and y. Since $b/b^* \simeq 1$ (especially when A is small), Eq. (3.54) reduces to

$$\mathrm{w}_n^*(x,y) \simeq \frac{1}{4\pi A}\int_{-1}^{1}\frac{1}{\eta-y}\partial_\eta[\psi_n^*](x,\eta)\mathrm{d}\eta. \tag{3.57}$$

The solution $\partial_\eta[\psi_n^*](x,\eta)$ of (3.57) can be easily found using Carleman inversion formula (3.20), then the dominant order solution can be obtained, and a higher order solution can be derived from the triangular system using the procedure introduced in section 3.1.

Now, let us consider a particular case: $\mathrm{w}^*(x,y)$ only depends on x. The zeroth order solution satisfying the condition (3.53) is

$$\partial_\eta[\psi](x,\eta) = \frac{4A\mathrm{w}^*(x)}{b^*}\frac{\eta}{\sqrt{1-\eta^2}}. \tag{3.58}$$

Therefore, the zeroth order acceleration potential should be

$$[\psi](x,\eta) = -\frac{4A\mathrm{w}^*(x)}{b^*}\sqrt{1-\eta^2}. \tag{3.59}$$

The corresponding dimensional order pressure jump is

$$[\Psi](X,Y) = -\frac{4D(\mathrm{W}(X))}{b^*}\sqrt{H^2-Y^2}. \tag{3.60}$$

where b^* should be expressed in dimensional coordinates X and Y. Accordingly, an integration of (3.60) from $-H$ to H gives the force per unit chord length in the Z direction

$$F_0^a(X) = \rho\frac{2\pi H^2}{b^*}D(W(X)). \tag{3.61}$$

It can be easily found that b^* is equal to 2 when A is asymptotic small and far from the leading and trailing edges (see Fig. 3.10). This implies that Eq. (3.60) is equivalent to the result of slender body theory for a slender rectangular surface. Thus, (3.61) can be regarded as Slender-body theory corrected for the effect of leading and trailing edges. Compared to the previous asymptotic methods, the asymptotic techniques in this section is much easier (due to the absence of 'Matched' procedure). Moreover, the locations of the leading edge and trailing edge appear in term $2/b^*$, it seems that Eq. (3.61) can include the influence of the surface geometry on the distribution of the pressure jump and the Z-direction force per unit length. Using (3.59) the fist order force can be found without any mathematical difficulty (noting that the factor $\frac{1}{4}$ may be used in (3.50)).

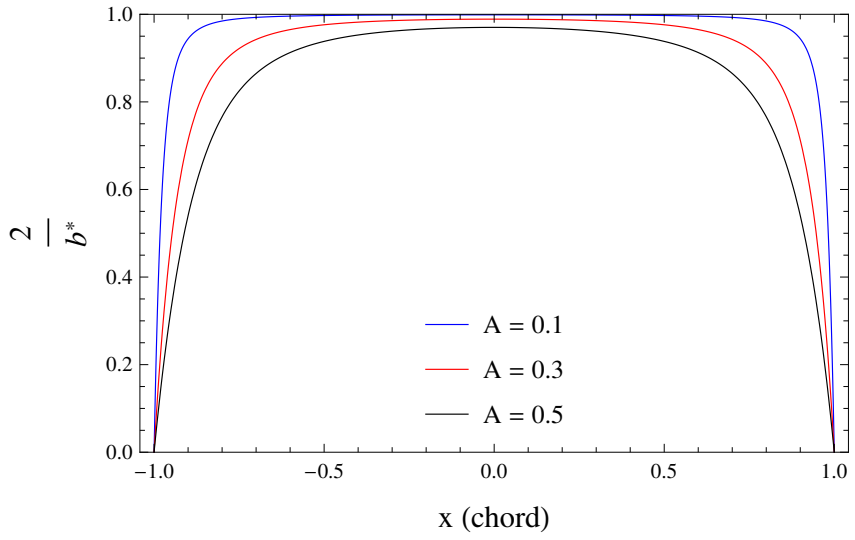

Figure 3.10 – The factor $2/b^*$ as a function of chordwise coordinate for various aspect ratio.

3.4 Results, comparisons and discussions

In order to show the performance of the result (3.61) obtained from the asymptotic solution by acceleration potential, we consider the same problem as introduced in section 3.2.

Firstly, the aspect ratio of the rectangular surface is $A = 0.3$, the surface is moving at the reduced frequency $k = 0.5$, the lateral displacement is imposed to be the first beam eigenmode in vacuo. The force per unit chord length is plotted with respect to the chordwise coordinate x in Fig. 3.11, the result given by (3.61) is denoted by 'Asymptotic Solution by Acceleration Potential'.

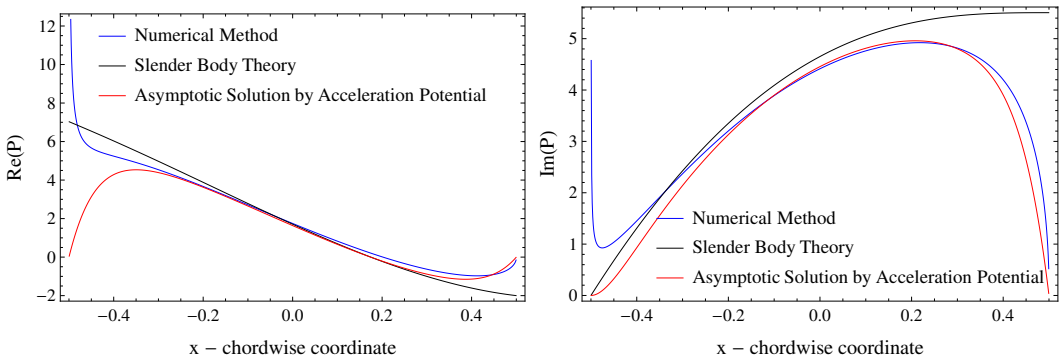

Figure 3.11 – Real and imaginary parts of the force per unit length, $A = 0.3$, $k = 0.5$, first beam eigenmode.

At mid-chord, the terms b^* gives approximately 2, the asymptotic solution by acceleration potential is therefore equivalent to Slender body theory, this explains the coincidence between the black curve and the red curve around $x = 0$. At the trailing edge, the Kutta condition is fulfilled by the asymptotic solution by acceleration potential, consequently in the posterior part of the chord, the red curve gives better result than the black one, and shows a good agreement with the numerical result. However, the term $2/b^*$ is symmetric about $x = 0$, this makes the force given by Eq. (3.61) tending to zero when approaching the leading edge. Thus, a discrepancy between the numerical result and the result of the asymptotic solution by acceleration potential appears in the anterior part of the chord. Since the formulation in section 3.3 does not impose any condition at the leading edge, this discrepancy can be regarded as the result from the leading edge singularity (which is associated to leading edge suction). It would be difficult and need more theoretical techniques to include the leading edge suction in (3.61), but a simple way to diminish this discrepancy is to set the leading edge l^*_{LE} at $-\infty$ in (3.56), we then have

$$b^*_m = 1 + \frac{[(l^*_{TE} - x)^2 + A^2/4]^{1/2}}{l^*_{TE} - x}. \tag{3.62}$$

The modified factor $2/b^*_m$ is plotted in Fig. 3.12. Replacing b^* by b^*_m in Eq.(3.61), we obtain the modified asymptotic solution by acceleration potential (ASAP). The corresponding result for the above case is shown in Fig. 3.13. To compare with the modified asymptotic solution by velocity potential, the result given by (3.35) is also plotted in this figure and marked by 'Modified ASVP'.

As expected, the modified asymptotic solution by acceleration potential gives the same result as Slender body theory near the leading edge, the discrepancy compared with the numerical result is therefore diminished and becomes acceptable. The modified ASAP gives almost the same result as the asymptotic solution by acceleration potential in the posterior part of the chord, and the Kutta condition is still satisfied at the trailing edge. Compared with the result of the modified ASVP, the result of the modified ASAP tends to zero less quickly, and shows a little better agreement with the numerical result.

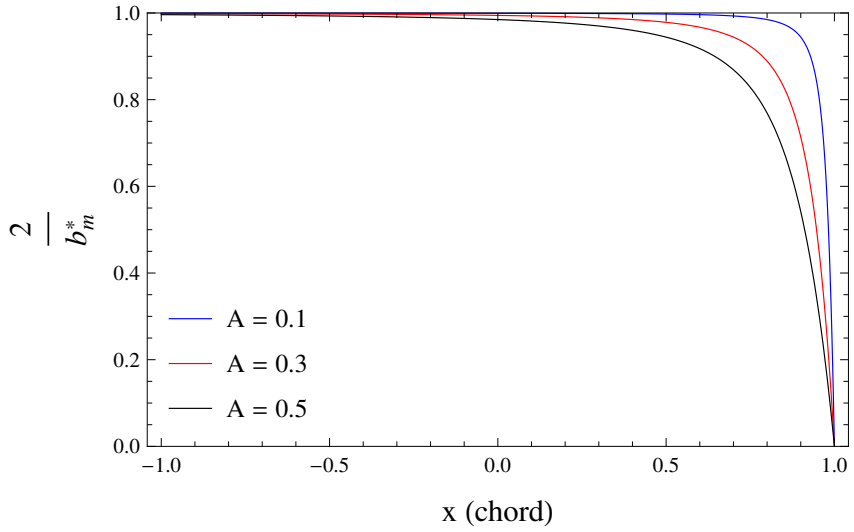

Figure 3.12 – The modified factor $2/b^*$ as a function of chordwise coordinate for various aspect ratio.

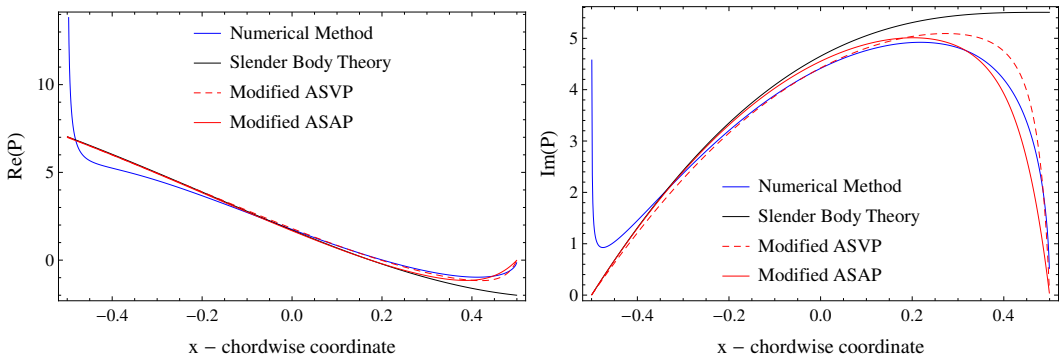

Figure 3.13 – Real and imaginary parts of the force per unit length, A=0.3, k=0.5, first beam eigenmode.

Secondly, the same surface moving at the larger reduced frequency $k = 50$ is considered. The force per unit chord length obtained from the numerical code, Slender body theory, modified ASVP, modified ASAP are plotted in Fig. 3.14.

From Fig. 3.14, it seems that the influence of the trailing edge on the distribution of the force becomes more important when the surface is moving at a larger reduced frequency. Then, the modified asymptotic solution by acceleration potential gives better result than the modified ASVP in the posterior part of the chord. Moreover, The modified ASAP, the modified ASVP, and Slender body theory gives almost the same results near the leading edge. This validates that the modified ASAP can model the flow around a surface at large reduced frequency.

Finally, we want to examine the applicability of the modified ASAP to model a surface moving with a different lateral deflection. The aspect ratio of surface remains unchanged $A = 0.3$, the surface moves with the second beam eigenmode in vacuo at reduced frequency $k = 0.5$. The corresponding results for this surface are plotted in Fig. 3.15.

Since the modified ASAP is the zeroth order solution, the modified ASVP gives more accurate result than the modified ASAP. This implies that a higher order modified asymptotic solution by acceleration is needed to model the dynamics of the fluid surrounding a surface with the lateral deflection of small wavelength.

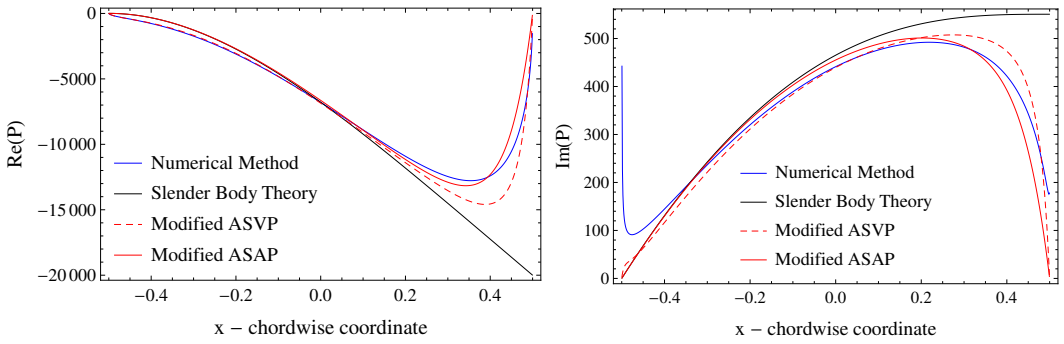

Figure 3.14 – Real and imaginary parts of the force per unit length, $A = 0.3$, $k = 50$, first beam eigenmode.

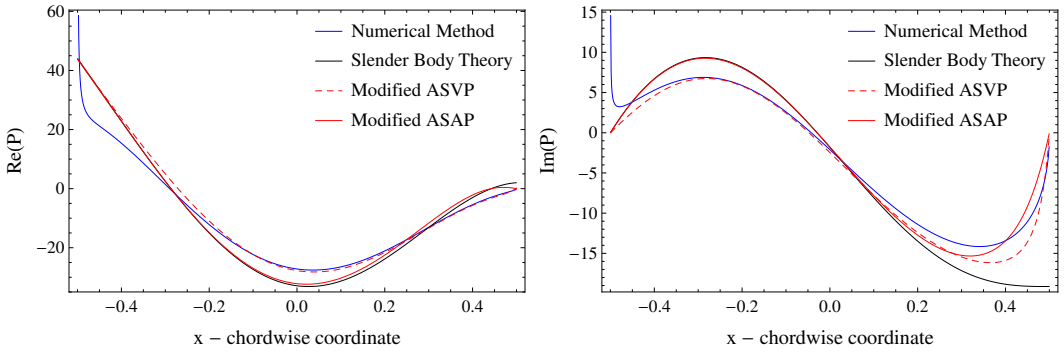

Figure 3.15 – Real and imaginary parts of the force per unit length, A=0.3, k=0.5, second beam eigenmode.

From the above applications, we can say that the modified asymptotic solution by acceleration gives almost the same result as the modified ASVP, it can include the surface with intermediate aspect ratio, and the Kutta condition is also satisfied. Moreover, it is a very simple theoretical model. All these advantages makes it suitable for the applications in various fluid structure interaction problems, as will be seen in the next chapter

Chapter 4

Application to the flag instability problem

4.1 Fluid structure interaction model

Consider a planar rectangular plate in the Cartesian coordinate system $(OXYZ)$. The geometry of plate is described by the aspect ratio $A = H/L$ (H being the span and L the chord). The leading edge is clamped at the Y axis, while the trailing edge is free. The plate is submerged in a flow which is assumed to be uniform, incompressible, irrotational outside the boundary layer and thin wake. The direction of flow is along the X-axis, and the flow is obviously three-dimensional (see Fig. 4.1). A three-dimensional fluid structure interaction model was proposed by Eloy et al. [27] (see [32, 56, 57] for older references), and it will be introduced with more details in this section.

Now two assumptions are made in order to derive a very simple fluid structure interaction model.

(i) The lateral deflection does not vary with respect to Y, hence it can be expressed by $Z(X,T)$;

(ii) The viscoelastic damping of the material and the tension due to the skin friction are neglected.

With the above assumptions, the linearized Euler-Bernoulli beam equation is capable to describe to dynamics of plate, with an external load equal to the average with respect to Y of the pressure difference distribution across the plate. Thus the equation governing the motion of the flexible plate is given by

$$\rho_p \frac{\partial^2 Z}{\partial T^2} + D\frac{\partial^4 Z}{\partial X^4} - \langle \Delta P \rangle_Y = 0, \tag{4.1}$$

where ρ_p is the mass per unit area of the plate, D is the flexural rigidity (given by $D = Eh_p^3/[12(1-\nu^2)]$, E is Young's modulus of plate, h_p is the plate thickness and ν the Poisson ratio), ΔP represents the pressure difference distribution across the plate, and $\langle\cdot\rangle_Y$ denotes the average along the span of plate. In order to facilitate the calculation and gain insight into the effect of various physical parameters, the following dimensionless variables are defined

$$x = \frac{X}{L}, \quad y = \frac{Y}{L}, \quad z = \frac{Z}{L}, \quad t = \frac{TU}{L}. \tag{4.2}$$

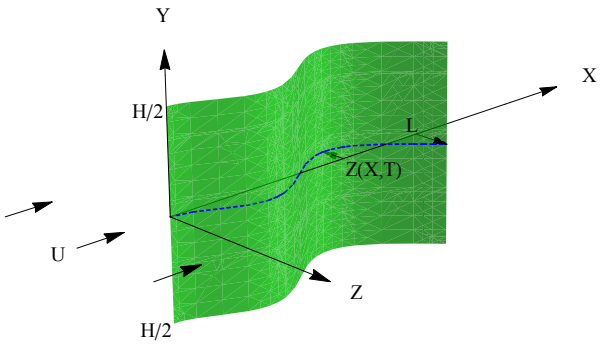

Figure 4.1 – Schematic of a plate with two-dimensional deflection $Z(X,T)$ submerged in an axial flow of velocity U.

An application of the above non-dimensional variables gives the dimensionless form of the governing equation

$$\frac{\partial^2 z}{\partial t^2} + \frac{1}{U^{*2}}\frac{\partial^4 z}{\partial x^4} - M^* \langle \Delta p \rangle_y = 0, \tag{4.3}$$

in which the dimensionless pressure difference $\langle \Delta p \rangle_y$, reduced flow velocity U^* and the dimensionless mass of the plate M^* are defined by

$$\langle \Delta p \rangle_y = \frac{\langle \Delta P \rangle_Y}{\rho_a U^2}, \quad U^* = \sqrt{\frac{\rho_p}{D}} LU, \quad M^* = \frac{\rho_a L}{\rho_p}, \tag{4.4}$$

where ρ_a is the density of the surrounding fluid (usually, air). Now, we can find that all the physical parameters are sorted by three dimensionless variables: A describing the geometry of plate, M^* representing the effect of mass, and U^* accounting for the influence of surrounding flow.

No doubt that the left hand side of governing equation (4.4) is linear with respect to z, and the linearity of $\langle \Delta p \rangle_y$ with respect to z can be ensured by the potential flow assumption. Hence, Eq. (4.4) is linear with respect to z.

If the lateral displacement $z(x,t)$ can be approximated by the Galerkin expansion

$$z(x,t) = \sum_{n=1}^{N} a_n z_n(x) e^{i\omega t}, \tag{4.5}$$

where N is a truncation integer for the Galerkin expansion and z_n are the beam eigenfunctions in vacuo satisfying the clamped boundary condition at the leading edge and the free boundary condition at the trailing edge [56, 57], the non-dimensional frequency ω is defined by $\omega = \Omega L/U$ (Ω is the complex angular frequency of plate).

Then, together with the lateral displacement $z(x,t)$, the pressure difference $\langle \Delta p \rangle_y(x,t)$ satisfying Eq. (4.4) can written as

$$\langle \Delta p \rangle_y(x,t) = \sum_{n=1}^{N} a_n p_n(x) e^{i\omega t}, \tag{4.6}$$

where $p_n(x)e^{i\omega t}$ is the average with respect to y of pressure difference due to the unsteady deflection $z_n(x)e^{i\omega t}$ of plate in the potential flow.

Note that the Galerkin modes satisfy the following relation

$$\frac{\mathrm{d}^4 z_n}{\mathrm{d}x^4} = k_n^4 z_n, \tag{4.7}$$

where the non-dimensional wave numbers k_n are defined by

$$\cos k_n \cosh k_n = 1, \tag{4.8}$$

then, we have $k_1 = 1.875104, k_2 = 4.69409$, etc. Injecting expressions (4.5 - 4.7) into Eq. (4.4) leads to

$$\sum_{n=1}^{N} \left(-\omega^2 z_n + \frac{1}{U^{*2}} k_n^4 z_n - M^* p_n \right) a_n = 0. \tag{4.9}$$

In addition, the orthogonality condition of Galerkin modes gives

$$z_m \otimes z_n = \int_0^1 z_m(x) z_n(x) \mathrm{d}x = \delta_m^n, \tag{4.10}$$

where δ_m^n is the Kronecker delta function, $\otimes$ is the standard scalar product. By multiplying Eq. (4.9) by the mode z_m ($m = 1, 2, \cdots, N$), the equation of motion becomes a system of linear equation with N unknowns (the coefficients a_n). The solvability condition of this linear system imposes

$$\det(\mathcal{M}(\omega)) = 0, \text{ with } \mathcal{M}(\omega) = -\omega^2 \mathcal{I} + \frac{1}{U^{*2}} \mathcal{I}^* - M^* \mathcal{P}, \tag{4.11}$$

where $\mathcal{I}$ is the identity matrix of size $N \times N$, $\mathcal{I}^*$ the diagonal matrix with k_n^4 in ascending order on the main diagonal, and the elements of square matrix $\mathcal{P}$ are given by

$$\mathcal{P}_{m,n} = z_m \otimes p_n. \tag{4.12}$$

The coefficients $\mathcal{P}_{m,n}$ are functions of ω due to the dependence of pressure jump distribution on the dimensionless angular frequency ω.

Now, the problem becomes an eigenvalue problem. That is, to determine the stability of a plate with mass ratio M^*, aspect ratio A (influencing the pressure jump term), and submerged in the flow with dimensionless velocity U^*, one needs to firstly calculate the matrix $\mathcal{P}$ with a suitable fluid model, then find the $2N$ solutions of Eq. (4.11) (note that if ω is a solution, then the negative conjugate $-\overline{\omega}$ is also a solution). If there is at least one solution ω_i whose corresponding grow rate (given by the negative imaginary part $-\Im(\omega_i)$) is positive, then this plate is unstable in the flow with non-dimensional velocity U^* and the flutter frequency is the real part of this solution $\Re(\omega_i)$.

4.2 Flutter modes with Slender body theory

As shown in the previous section, a proper fluid model should be firstly chosen to model the dynamics of the surrounding fluid. In this section, Slender body theory is applied to calculate the force exerted on the moving plate with small aspect ratio $A < 1$ by the surrounding fluid in this section.

As shown before, the force per unit chord length $L(x)$ on the plate can be calculated from Eq. (1.25), therefore, the average with respect to y of dimensionless pressure difference can be derived

$$\langle \Delta p \rangle_y(x) = \frac{L(x)}{H\rho_a U^2}. \tag{4.13}$$

Consequently, the matrix $\mathcal{P}$ can be determined by

$$\mathcal{P} = -\frac{\pi A}{4}(-\omega^2 \mathcal{I} + 2i\omega\mathcal{P}^1 + \mathcal{P}^2), \tag{4.14}$$

where the elements of matrix $\mathcal{P}^1$ and $\mathcal{P}^2$ are given by

$$\begin{aligned} \mathcal{P}^1_{m,n} &= z_m \otimes \frac{\mathrm{d}z_n}{\mathrm{d}x}, \\ \mathcal{P}^2_{m,n} &= z_m \otimes \frac{\mathrm{d}^2 z_n}{\mathrm{d}x^2}. \end{aligned} \tag{4.15}$$

Now, the dynamics of surrounding fluid is included through the matrix $\mathcal{P}$, one only needs to solve the solvability equation (4.11) to find the complex frequencies ω_i, and hence the growth rates $-\Im(\omega_i)$ and the frequencies $\Re(\omega_i)$ of flutter modes. Since the deflection is mainly modeled by the first and second eigenfunctions when the plate begins to flap, the first five eigenfucntions are chosen to approximate the deflection $z(x,t)$, accordingly the truncation integer is $N = 5$. As Eq. (4.11) is an explicit polynomial of ω, It can be easily solved numerically.

For a given plate with aspect ratio $A < 1$ and mass ratio M^*, the complex frequencies of this plate surrounded by the flow with dimensionless velocity U^* can be found by solving the solutions of Eq. (4.11), hence these flutter modes should be a function of dimensionless velocity U^*. The results are given in Fig. 4.2 for a clamped-free plate with aspect ratio $A = 0.1$ and mass ratio $M^* = 1$. The products $\Re(\omega)U^*$ and the growth rates $\sigma(\omega)$ of the first five flutter modes are given in the top figure and bottom figure, respectively. For the sake of simplicity, the flutter modes with negative dimensionless frequency $\Re(\omega)$ are not plotted, but can be obtained by the symmetry $\omega \to \bar{\omega}$.

When the dimensionless flow velocity is very low $U^* \ll 1$, the matrix $\mathcal{M}$ in Eq. (4.11) can be regarded as a diagonal matrix, the solvability condition (4.11) therefore becomes

$$\prod_{n=1}^{N}\left[-\omega^2 + \frac{k_n^4}{U^{*2}} + \frac{\pi A M^*}{4}(-\omega^2 + 2i\omega\mathcal{P}^1_{n,n} + \mathcal{P}^2_{n,n})\right] = 0. \tag{4.16}$$

Then, the complex solutions ω of the above equation are

$$\omega_n = i\frac{\pi A M^*}{4+\pi A M^*}\mathcal{P}^1_{n,n} \pm \sqrt{-\left(\frac{\pi A M^* \mathcal{P}^1_{n,n}}{4+\pi A M^*}\right)^2 + \frac{\pi A M^* \mathcal{P}^2_{n,n}}{4+\pi A M^*} + \frac{4}{4+\pi A M^*}\frac{k_n^4}{U^{*2}}},\ n = 1, 2, \cdots, N \tag{4.17}$$

Consequently, the frequencies and the growth rates of flutter modes for low dimensionless flow velocity can be approximately determined by

$$\begin{aligned} \Re(\omega_n)U^* &= \frac{k_n^2}{\sqrt{1+\pi AM^*/4}}, \\ \sigma(\omega_n) &= -\frac{\pi AM^*}{4+\pi AM^*}\mathcal{P}^1_{n,n}. \end{aligned} \tag{4.18}$$

Note that the plate under consideration has the aspect ratio $A = 0.1$ and mass ratio $M^* = 1$. A simple calculation for $\mathcal{P}^1$ gives that $\mathcal{P}^1_{n,n} = 2$ for all $n = 1, 2, \cdots, N$.

a. In the limit of vanishing U^*, the products $\Re(\omega)U^*$ and the growth rates $\sigma(\omega)$ of the first five flutter modes derived from Eq. (4.18) are

$$\begin{array}{c|cc} \text{Theoretical prediction} & \Re(\omega)U^* & = & 3.38564,\ 21.217,\ 59.4094,\ 116.419,\ 192.449 \\ U^* = 0 & \sigma(\omega) & = & -0.14557 \end{array} \tag{4.19}$$

While the direct solving of Eq. (4.11) gives the products $\Re(\omega)U^*$ and the growth rates $\sigma(\omega)$ of the first five flutter modes for $U^* = 0.01$

$$\begin{array}{c|cc} \text{Direct solving} & \Re(\omega)U^* & = & 3.38558,\ 21.217,\ 59.4083,\ 116.417,\ 192.445 \\ U^* = 0.01 & \sigma(\omega) & = & -0.14564 \end{array} \tag{4.20}$$

Thus, Eq. (4.18) perfectly predicts the products $\Re(\omega)U^*$ and the growth rates $\sigma(\omega)$ of the first five flutter modes at the origin of U^* in Fig. 4.2, and explains why the first five flutter modes share the same growth rate at the origin of U^* in Fig. 4.2 (due to the selected fluid model and $\mathcal{P}^1_{n,n} = 2$ for $n = 1, 2, \cdots, N$). The negative growth rate is consistent with the observations in daily life, since a plate in the flow with zero velocity should be always stable.

b. As the dimensionless flow velocity U^* increases from zero and up to a certain value U^*_h, the hypothesis of a diagonal matrix $\mathcal{M}$ is always valid, and hence Eq. (4.18) is still applicable. The products $\Re(\omega)U^*$ and the growth rates $\sigma(\omega)$ of all flutter modes derived from Eq.(4.18) are independent of the dimensionless flow velocity U^*, this explains why all the curves in Fig. 4.2 are almost horizontal lines for $U^* < U^*_h$.

The calculation of U^*_h depend on k_n, since the hypothesis of a diagonal matrix $\mathcal{M}$ requires k_n^2/U^* being sufficiently large compared to the non-diagonal elements of $\mathcal{M}$. Therefore, a minimum dimensionless wave number k_1 gives the minimum U^*_h, it explains why the first flutter mode forks firstly, then the fork of the second flutter mode arises, and so on, as U^* increases from zero.

c. As the dimensionless flow velocity U^* keeps increasing from U^*_h up to a not too large value compared to the used dimensionless wave numbers k_n, the fork of all the flutter modes arises.

For $U^* < 16.334$, all the growth rates are negative, it implies that all the flutter modes are stable. For $U^* > 16.334$, the second flutter mode becomes unstable, and for higher dimensionless flow velocity, the forth flutter mode eventually becomes unstable. The critical dimensionless flow velocity is denoted as U^*_c for which the first unstable flutter mode appears, then for the plate considered in this section the critical dimensionless flow velocity is $U^*_c = 16.334$.

In Fig. 4.2, the first flutter mode appears to be always stable. Particularly, when $25.5 < U^* < 33.2$, the curve of growth rate splits into two stable flutter modes (labeled as 1a and 1b) and the product $\Re(\omega)U^*$ becomes zero (labeled as 1a + 1b). However, if $U^* > U^*_c$ and U^* keeps increasing, the amplitude of deflection will become larger, and the hypothesis of

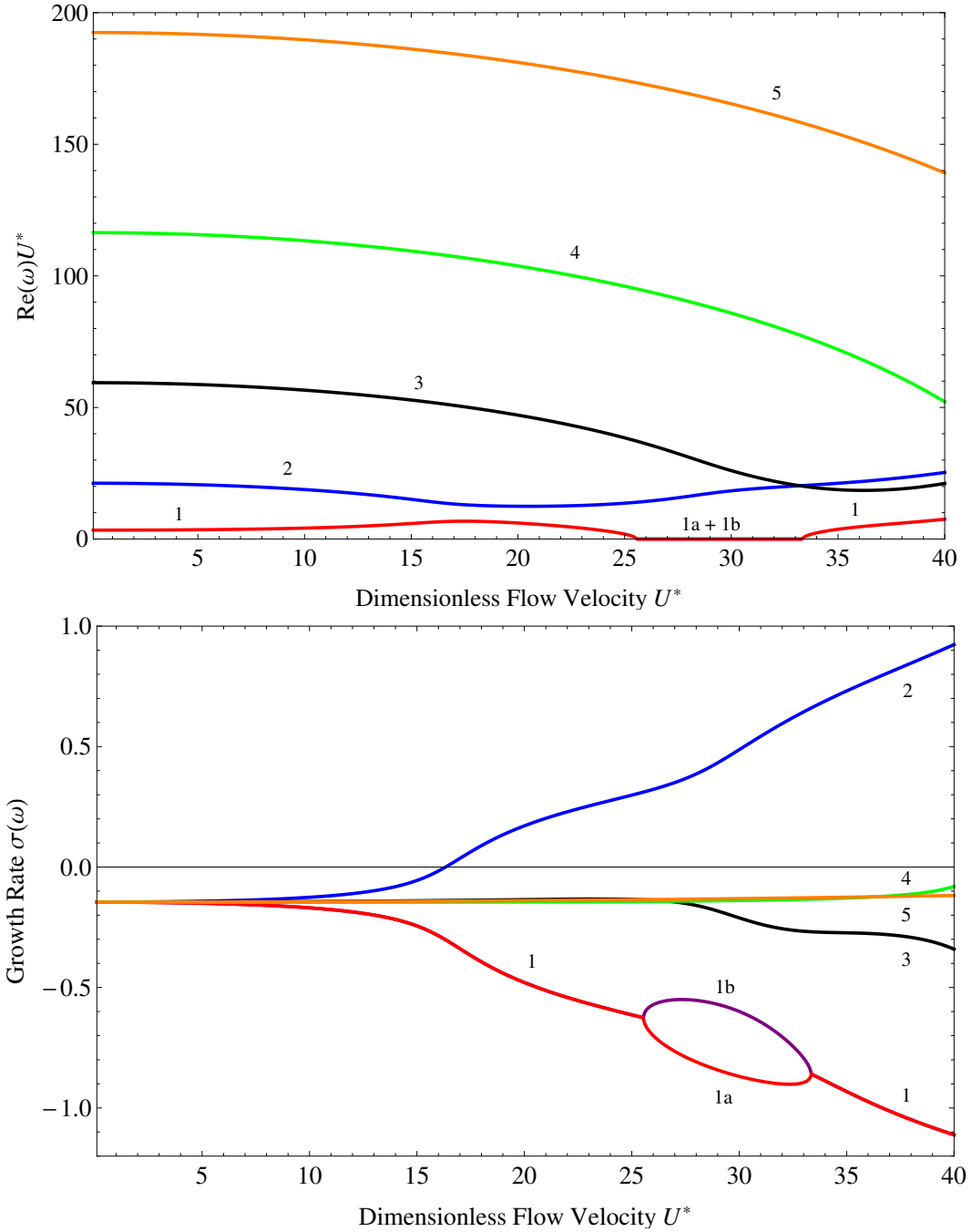

Figure 4.2 – Frequencies (top) and growth rate (bottom) of the first five flutter modes as a function of dimensionless flow velocity, results derived from Slender body theory. The mass ratio of the clamped-free plate is $M^* = 1$, the Aspect ratio $A = 0.1$. The number labels indicate different flutter modes in ascending order of dimensionless angular frequency.

small amplitude deflection in section 4.1 will not be valid, hence, the curves after U_c^* in Fig. 4.2 just shows the qualitative behavior of the plate.

d. When the dimensionless flow velocity U^* is sufficiently large compared to the used dimensionless wave numbers k_n, Eq. (4.11) turns to be independent of U^*. Therefore, the products $Re(\omega)U^*$ and the growth rates $\sigma(\omega)$ of the first five flutter modes should be constant with respect to U^* (not shown in Fig. 4.2). In this case, more eigenfunctions for $z(x,t)$ should be used to account for the behavior of plate in very high dimensionless flow velocity on condition that the selected fluid model can include the fluid surrounding the plate with a large and aperiodic deflection.

4.3 Flutter modes with the modified asymptotic solution by acceleration potential

We want to compare the results of the previous section using SBT with results obtained by modeling the flow with modified ASAP. The same plate is considered with aspect ratio $A = 0.1$ and mass ratio $M^* = 1$. As shown in section 3.4, the modified asymptotic solution by acceleration potential gives more accurate results than those of Slender body theory for a rectangular lifting surface by fulfilling the Kutta condition at trailing edge.

The average of the pressure difference across the plate with respect to y can be given by

$$\langle \Delta p \rangle_y(x) = -\frac{\pi A}{2 + \sqrt{4 + A^2/(1-x)^2}}(-\omega^2 z + 2i\omega \frac{\mathrm{d}z}{\mathrm{d}x} + \frac{\mathrm{d}^2 z}{\mathrm{d}x^2}). \tag{4.21}$$

Consequently, the matrix $\mathcal{P}$ becomes

$$\mathcal{P} = -\pi A(-\omega^2 \mathcal{P}^0 + 2i\omega \mathcal{P}^1 + \mathcal{P}^2), \tag{4.22}$$

where the elements of matrices $\mathcal{P}^0$, $\mathcal{P}^1$ and $\mathcal{P}^2$ are given by

$$\begin{aligned}
\mathcal{P}^0_{m,n} &= z_m \otimes \left(\frac{z_n}{2 + \sqrt{4 + A^2/(1-x)^2}} \right), \\
\mathcal{P}^1_{m,n} &= z_m \otimes \left(\frac{\mathrm{d}z_n/\mathrm{d}x}{2 + \sqrt{4 + A^2/(1-x)^2}} \right), \\
\mathcal{P}^2_{m,n} &= z_m \otimes \left(\frac{\mathrm{d}^2 z_n/\mathrm{d}x^2}{2 + \sqrt{4 + A^2/(1-x)^2}} \right).
\end{aligned} \tag{4.23}$$

Like in section 4.2, the lateral deflection $z(x,t)$ is approximated by five eigenfunctions. To determine the stability of the plate for a given dimensionless flow velocity U^*, One just needs to calculate the complex solutions ω of solvability condition (4.11), then the products $\Re(\omega)$ and the growth rates $\sigma(\omega)$ of all the flutter modes are found. If there is at least one flutter whose growth rate is positive, then the plate is unstable.

The products $\Re(\omega)U^*$ and the growth rates $\sigma(\omega)$ of the first five flutter modes are plotted as a function of dimensionless flow velocity U^* for a clamped-free plate with aspect ratio $A = 0.1$ and mass ratio $M^* = 1$ in Fig. 4.3.

When the dimensionless flow velocity is very low $U^* \ll 1$, the matrix $\mathcal{M}$ in Eq. (4.11) can be regarded as a diagonal matrix, the solvability condition (4.11) yields approximate values for ω around $U^* = 0$ (from a similar equation to (4.16))

$$\begin{aligned} \mathcal{R}e(\omega)U^* &= \frac{k_n^2}{\sqrt{1+\pi AM^*\mathcal{P}^0_{n,n}}}, \\ \sigma(\omega) &= -\frac{\pi AM^*\mathcal{P}^1_{n,n}}{1+\pi AM^*\mathcal{P}^0_{n,n}}. \end{aligned} \tag{4.24}$$

A simple computation gives the diagonal elements of $\mathcal{P}^0$ and $\mathcal{P}^1$

$$\begin{aligned} \mathcal{P}^0_{n,n} &= 0.222076,\ 0.228132,\ 0.231334,\ 0.233534,\ 0.235103. \\ \mathcal{P}^1_{n,n} &= 0.459047,\ 0.382890,\ 0.333162,\ 0.294657,\ 0.265152. \end{aligned} \tag{4.25}$$

Then the products $\Re(\omega)U^*$ and the growth rates $\sigma(\omega)$ of the first five flutter modes derived from Eq. (4.24) for $U^* = 0$ are

$$\begin{array}{rcccccc} \mathcal{R}e(\omega)U^* & = & 3.39295 & 21.2632 & 59.5377 & 116.67 & 192.864 \\ \sigma(\omega) & = & -0.134809 & -0.112244 & -0.097574 & -0.0862419 & -0.0775708 \end{array} \tag{4.26}$$

While the direct solving of Eq. (4.11) gives the products $\Re(\omega)U^*$ and the growth rates $\sigma(\omega)$ of the first five flutter modes for $U^* = 0.01$

$$\begin{array}{rcccccc} \mathcal{R}e(\omega)U^* & = & 3.39943 & 21.2854 & 59.5724 & 116.701 & 192.873 \\ \sigma(\omega) & = & -0.134759 & -0.113749 & -0.099873 & -0.0891127 & -0.0812197 \end{array} \tag{4.27}$$

Therefore the following observations and explanations can be made,

a. The products $\Re(\omega)U^*$ and the growth rates $\sigma(\omega)$ of the first five flutter modes at the origin of U^* in Fig. 4.3 are perfectly predicted by (4.24). The first five flutter modes don't share the same growth rate any more for $U^* = 0.01$.

b. The horizontal lines for low dimensionless flow velocity U^* in Fig. 4.3 are simply the consequence of the independence of $\Re(\omega)U^*$ and $\sigma(\omega)$ in (4.24) from the dimensionless flow velocity U^*. The forks of flutter modes arise in ascending order of k_n in Fig. 4.3, which is also the order of failure of hypothesis of a diagonal matrix $\mathcal{M}$ in Eq. (4.11) as U^* increases from zero.

c. When $U^* > 15.715$, the growth rate of the second flutter mode turns to be positive (while the growth rates of the rest four flutter modes remain negative in the meantime), thus the plate becomes unstable and the critical dimensionless flow velocity for this plate is $U_c^* = 15.715$. The two branches split from the first flutter mode for $26 < U^* < 33.4$ always stay stable. For a plate with infinite span, Eloy et al. [27] has pointed that these two divergence modes always remain stable, while Guo & Païdoussis [32] has shown that these two divergence modes can be unstable for different boundary conditions.

Although Slender body theory gives almost the accurate force on a plate with small aspect ratio (A = 0.1), the critical flow velocity calculated with the modified asymptotic solution by acceleration potential is slightly different form that derived with Slender body theory ($U_c^* = 16.334$ for SBT, $U_c^* = 15.715$ for MASVP). This implies the fluid model plays a very important role in the stability analysis of a plate, and it needs an accurate fluid model in order to exactly predict the critical flow velocity, especially for intermediate aspect ratios.

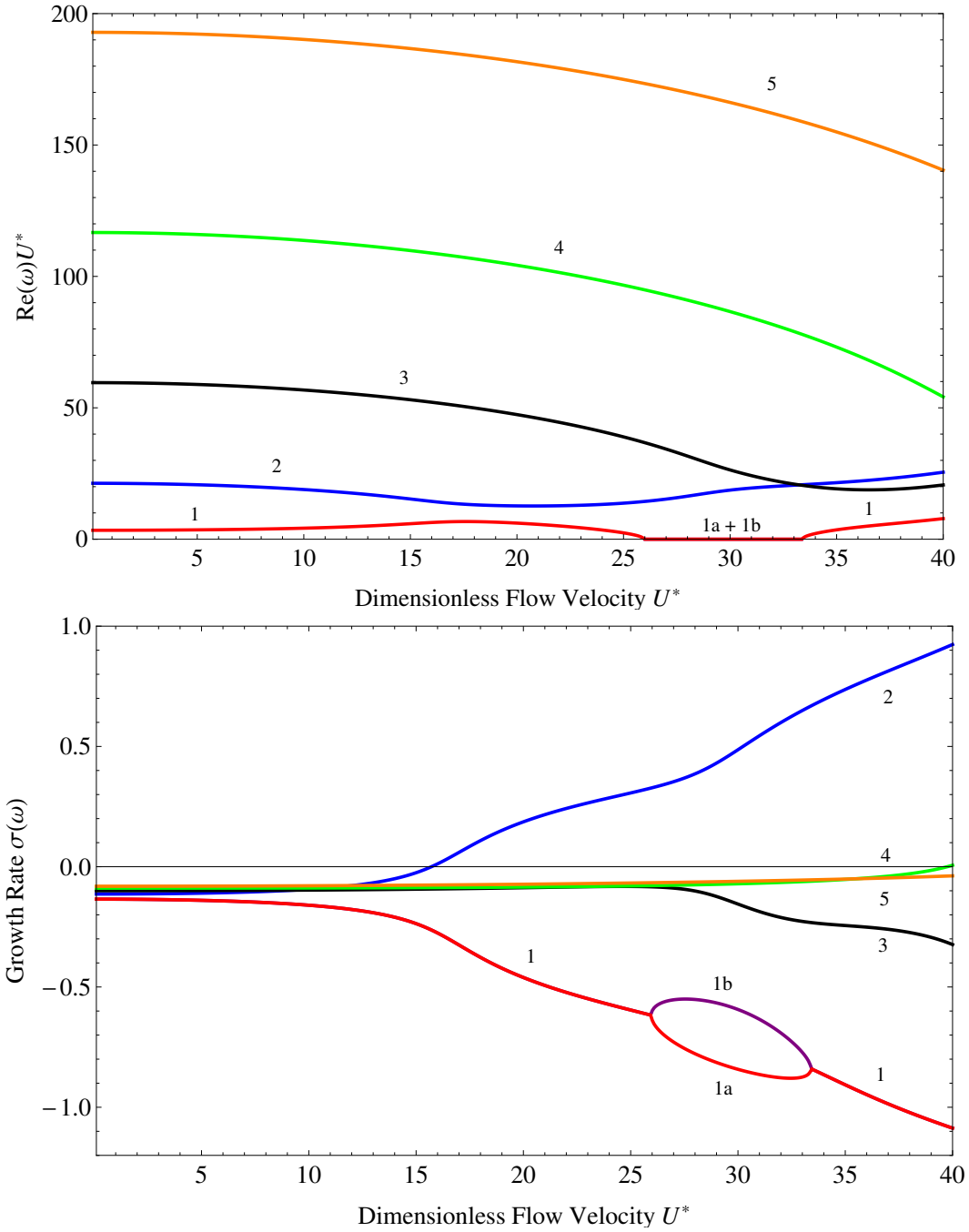

Figure 4.3 – Frequencies (top) and growth rate (bottom) of the first five modes as a function of dimensionless flow velocity, results derived from the modified asymptotic solution by acceleration potential. The mass ratio of the clamped-free plate is $M^* = 1$, the aspect ratio $A = 0.1$. The number labels indicate different flutter modes in the ascending order of dimensionless angular frequency.

4.4 Critical curves

In this section, the effects of varying the aspect ratio A and the mass ratio M^* on the critical flow velocity are studied.

The critical flow velocities U_c^* are plotted with respect to the aspect ratio A for a plate with mass ratio $M^* = 1$ in Fig. 4.4. The crosses are the results of Eloy et al. [27]. The black curve and the red one are the results obtained with the Slender body theory and the Asymptotic solution by acceleration potential, respectively.

We find that the critical flow velocity U_c^* is a monotonically decreasing function of A for a single flutter mode. The results with Slender body theory fails as the aspect ratio increases, since Slender body theory can not give accurate pressure difference, especially when $A > 0.3$. The good agreement between the crosses and the red curve ($A < 0.7$) shows the applicability of the modified asymptotic solution by acceleration potential to the instability analysis of a plate with intermediate aspect ratio. The discontinuities of U_c^* in Fig. 4.4 (when $A = 0.54$ for the black curve, $A = 0.98$ for the red one) are always accompanied by the shift from the second flutter mode to the third flutter mode.

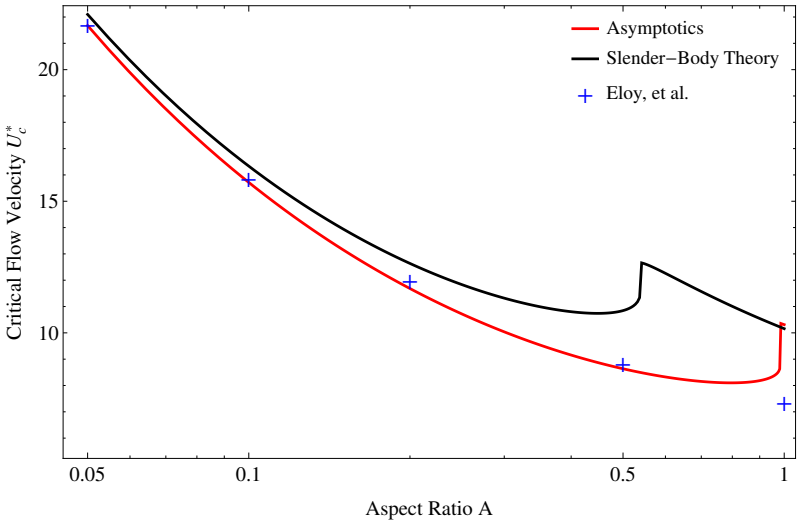

Figure 4.4 – Critical flow velocity as a function of aspect ratio A for a clamped free plate with mass ratio $M^* = 1$. Crosses are the results from Eloy et al. [27]. The black curve and the red one are the results derived from Slender body theory and modified asymptotic solution by acceleration potential, respectively.

Now, the effect of the mass ratio M^* on the critical flow velocity U_c^* for a clamped free plate with various aspect ratios ($A = 0.2, 0.9, 1$) is shown in Fig. 4.5.

From Fig. 4.5, it can be seen that the red curve shows a very good agreement with the blue one for the clamped free plate with aspect ratio $A = 0.2$ and low mass ratio ($M^* < 3$). When the aspect ratio of the plate is no longer small ($A = 0.9$), the red curve still gives reasonable results (comparing with the blue curve for $A = 1$) for low mass ratio ($M^* < 1$). Noting the results in Fig. 4.4, we can conclude that the modified asymptotic solution by acceleration potential can be applied to the instability analysis of a clamped free plate with intermediate aspect ratio (typically $A < 0.7$) and low mass ratio ($M^* < M_l^*$, M_l^* being dependent on A).

As already shown in Fig. 4.4, the discontinuities of the critical flow velocity of blue curves in Fig. 4.5 imply a shift of the unstable mode. For $A = 0.2$ and $M^* < 3$, the fist unstable modes of the blue curve or the red one is the second flutter mode, while it is the third flutter mode when $A = 0.2$ and $M^* > 3$. The shift can also causes a peculiar behavior:

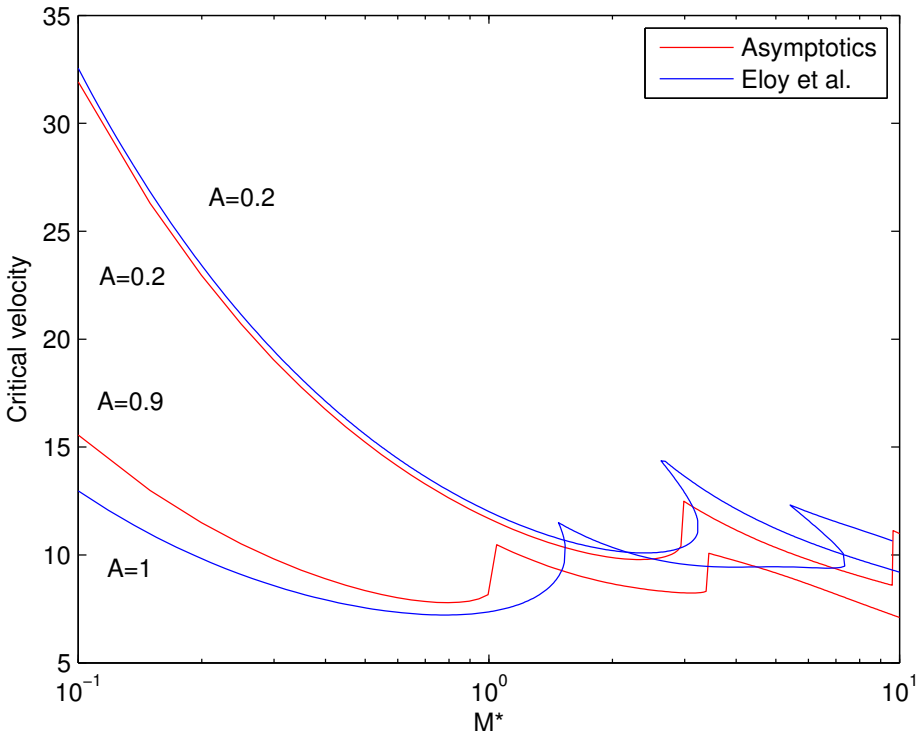

Figure 4.5 – Critical flow velocity as a function of mass ratio M^* for a clamped free plate with different aspect ratios. The red curves are the results obtained with modified asymptotic solution by acceleration potential, while the blue ones are the results of Eloy et al. [27].

Eloy et al. [27] has pointed out that for $M^* = 1.5$ and $A = 1$, the plate is unstable (shown by the blue curve for $A = 1$ in Fig. 4.5) for $9.2 < U^* < 11.2$, then becomes stable when $11.2 < U^* < 11.4$, and finally turns to be unstable for $11.4 < U^*$. This peculiar phenomena has also been reported by Lemaitre et al. [43] in the case of very small aspect ratio. It is also found when deriving the red curves (but not shown in Fig. 4.5, since it has little physical meaning or experimental evidence).

Finally, we can say that the modified asymptotic solution by acceleration potential is a very simple model to take into account the three-dimensional effect of the fluid surrounding a plate with the intermediate aspect ratio. It is therefore easy to applied to the stability analysis of the plate, the given critical flow velocity is trustful, and the effect of aspect ratio can be included.

Chapter 5

Application to the fish swimming problem

5.1 Fluid structure interaction model

We consider a three dimensional fish characterized by its body length L, tail height D and body width B. The aspect ratio of fish is defined as $AR = D/L$.The cross section of fish is an ellipse with its two axes along the y-axis and z-axis. The length of major axis is the local height $d(x)$, while the length of minor axis is the local width $b(x)$ (see Fig. 5.1). The area of cross section is $A(x)$, and the wetted surface of the fish is denoted by S. For the sake of simplicity, the fish is assumed to be neutrally buoyant, hence the uniform body density ρ is equal to the density of the surrounding flow. The major effect of the additional appendages (pectoral, dorsal, and anal fins) is to improve the agility of swimming which is not considered in this section, the appendages on the body will be therefore neglected.

To avoid blunt leading and trailing edge, the local height and width should satisfy

$$d(0) = b(0) = b(L) = 0. \tag{5.1}$$

The mass of body per unit length is

$$m_b(x) = \rho\pi\frac{d(x)b(x)}{4} = \rho A, \tag{5.2}$$

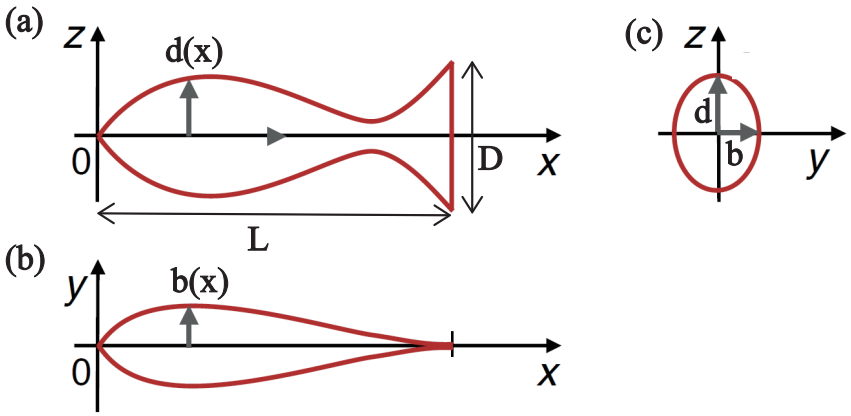

Figure 5.1 – Geometry of the fish. (a) side view, (b) top view, (c) cross section

while the added mass of fluid per unit length due to the motion of fish's cross section at x is

$$m_a(x) = \rho\pi\frac{[d(x)]^2}{4}. \tag{5.3}$$

The undulatory motion of the fish is defined as the displacement between the backbone and the neutral backbone, then it can be written as

$$h^*(x,t) = f(x)e^{i\left(\omega t - \frac{2\pi x}{\lambda}\right)}, \tag{5.4}$$

where ω is the angular frequency of tail-beat (with tail-beat period $T = 2\pi/\omega$), $f(s)$ is the envelope of the motion and λ is the wavelength of the fish undulation. We assume $b(x)$, $d(x)$, h^* to be small compared with L such that a linearized fluid structure interaction model can be applied.

The fish swims in the negative x-direction at the velocity U through the fluid at rest. The corresponding Reynolds number is defined as

$$Re = \frac{UL}{\nu}, \tag{5.5}$$

where ν is the kinematic viscosity of water. The Reynolds number is supposed to be high so that potential flow theory can be applied to model the surrounding fluid.

The pressure distribution on the swimming body gives rise to a forward thrust F_T powering the forward motion, and a lateral force (lift) $F_L(x,t)$ which causes an additional lateral motion known as recoil. If the imposed motion $h^*(x,t)$ and the recoil are small compared with L, the total deflection $h(x,t)$ can written in a linear form

$$h(x,t) = h^*(x,t) + y_0e^{i\omega t} + x\theta e^{i\omega t}, \tag{5.6}$$

where $y_0e^{i\omega t}$ is the lateral recoil and $\theta(t)e^{i\omega t}$ angular recoil.

The dynamics of a swimming fish is defined by its equations of motion [46, 69] which can be written as

$$\begin{aligned}\int_0^L m_b(x)\frac{\partial^2 h(x,t)}{\partial t^2}\mathrm{d}x &= \int_0^L F_L(x,t)\mathrm{d}x,\\ \int_0^L xm_b(x)\frac{\partial^2 h(x,t)}{\partial t^2}\mathrm{d}x &= \int_0^L xF_L(x,t)\mathrm{d}x,\end{aligned} \tag{5.7}$$

in which $m_b(x)$ represents the mass of body per unit length, the first equation corresponds to the momentum equation in y-direction, the second one to the angular momentum equation, the lateral force $F_L(x,t)$ can be obtained from Slender-body theory as exposed in (1.25).

The x-direction momentum equation describes the equilibrium between the thrust and the drag for a fish swimming at a sustained velocity U. For the sake of simplicity, it is usually expressed as the equality between the time-average thrust $\overline{F_T}$ and the the time-average drag $\overline{F_D}$ [26, 46, 75]

$$\overline{F_T} = \overline{F_D}. \tag{5.8}$$

The time-average thrust $\overline{F_T}$ can be calculated from Lighthill's Slender body model [46]

$$\overline{F_T} = \frac{1}{2}m_a(L)\left\{\overline{\left(\frac{\partial h}{\partial t}\right)^2} - U^2\overline{\left(\frac{\partial h}{\partial x}\right)^2}\right\}_{x=L}. \tag{5.9}$$

The time-average drag can be evaluated by

$$\overline{F_D} = \frac{1}{2}\rho U^2 S C_D, \tag{5.10}$$

where the drag coefficient C_D around a swimming body can be modeled empirically as the friction coefficient of a flat plate C_f corrected for the thickness effects [75], that is

$$C_D = C_f(1 + 1.5D_L^{1.5} + 7D_L^3) \tag{5.11}$$

in which D_L is the maximum lateral dimension of the body normalised by body length L, C_f is given by

$$C_f = \begin{cases} 1.33Re^{-0.5}, & Re \leq 5 \times 10^5 \\ 0.072Re^{-0.2}, & Re > 5 \times 10^5 \end{cases} \tag{5.12}$$

A discontinuity of C_f occurs at $Re = 5 \times 10^5$ due to the transition from laminar to turbulent regime. Now, it can be seen that the problem is governed by 5 equations (Eq. (5.8), real and imaginary parts of (5.7)) connecting non-linearly 5 unknowns(U, real and imaginary parts of y_0 and θ)

5.2 The thrust from the modified asymptotic solution by acceleration potential

Although the result (3.61) in section 3.3 is only valid for a rectangular surface, comparing to Slender body theory [46] we define the lift per unit length acting on an arbitrary lifting-surface as

$$F_L(x,t) = -\frac{2}{b_m^*}\mathcal{D}(m_a(x)V(x,t)), \quad \text{with} \quad \mathcal{D} = \frac{\partial}{\partial t} + U\frac{\partial}{\partial x}, \tag{5.13}$$

in which

$$\begin{aligned} V(x,t) &= \mathcal{D}h(x,t), \\ b_m^* &= 1 + \frac{\sqrt{(L-x)^2 + D^2/16}}{L-x}. \end{aligned} \tag{5.14}$$

Thus, Eq. (5.13) can be regarded as the lift derived from Slender body theory corrected for the effect of aspect ratio. From this equation, we want to calculate the corresponding thrust using the method introduced in Slender body potential flow model [46]. The rate of work done by the fish through the lift acting on the lateral deflection $h(x,t)$ can be evaluated as

$$P = -\int_0^L \frac{\partial h}{\partial t} F_L(x,t)\mathrm{d}x = \int_0^L \frac{\partial h}{\partial t}\frac{2}{b_m^*}\mathcal{D}\{m_a(x)V(x,t)\}\mathrm{d}x \tag{5.15}$$

Applying the product rule of $\mathcal{D}$-operator and sorting the terms, we have

$$\begin{aligned} P &= \int_0^L \mathcal{D}\left\{\frac{\partial h}{\partial t}\frac{2}{b_m^*}m_a(x)V(x,t)\right\}\mathrm{d}x - \int_0^L m_a(x)V(x,t)\mathcal{D}\left\{\frac{\partial h}{\partial t}\frac{2}{b_m^*}\right\}\mathrm{d}x \\ &= \frac{\partial}{\partial t}\int_0^L \left\{\frac{\partial h}{\partial t}\frac{2}{b_m^*}m_a(x)V(x,t)\mathrm{d}x - \frac{V^2 m_a(x)}{b_m^*}\right\}\mathrm{d}x \\ &\qquad + U\frac{\partial h}{\partial t}\frac{2}{b_m^*}m_a(x)V(x,t)\Big|_0^L - U\int_0^L \frac{\partial h}{\partial t}\frac{\partial}{\partial x}\left(\frac{2}{b_m^*}\right)m_a(x)V(x,t)\mathrm{d}x. \end{aligned} \tag{5.16}$$

The time average of the first term of (5.16) is obviously zero. The non blunt leading edge leads to $m_a(0) = 0$, while the term $2/b_m^*$ gives zero at $x = L$, then the second term of (5.16) is also zero. The mean rate of work done by fish is therefore obtained

$$\begin{aligned} \overline{P} &= -\frac{U}{T}\int_0^T\int_0^L \frac{\partial h}{\partial t}\frac{\partial}{\partial x}\left(\frac{2}{b_m^*}\right)m_a(x)V(x,t)\mathrm{d}x\mathrm{d}t \\ &= -U\int_0^L m_a(x)\frac{\partial}{\partial x}\left(\frac{2}{b_m^*}\right)\overline{\frac{\partial h}{\partial t}V(x,t)}\mathrm{d}x. \end{aligned} \tag{5.17}$$

Note that the rate of shedding of kinetic energy of lateral motions can written as $\{\frac{1}{2}m_a(L)V^2(L,t)\}U$, subtracting the mean of this term from (5.17) gives the power available for producing the mean thrust $\overline{F_T}$, we then have

$$\overline{F_T}U = \overline{P} - \frac{1}{2}m_a(L)\overline{V^2(L,t)}U. \tag{5.18}$$

The mean thrust is therefore obtained

$$\overline{F_T} = -\int_0^L m_a(x)\frac{\partial}{\partial x}\left(\frac{2}{b_m^*}\right)\overline{\frac{\partial h}{\partial t}V(x,t)}\mathrm{d}x - \frac{1}{2}m_a(L)\overline{V^2(L,t)}. \tag{5.19}$$

It can be inferred that a drag is generated if the above subtraction is negative, which also means that more energy is shed in to the wake than the work done by the fish. In this case, the fish will be decelerated until the balance between the thrust and the drag is established.

Lighthill [46] has pointed out that only the lateral motion at the trailing edge affects the mean thrust for a slender body, while Eq. (5.19) is consistent with this conclusion, but states it in a general way. In fact, when the aspect ratio of fish AR is small, the term $2/b_m^*$ in (5.19) is always equal to 1, except near the trailing edge. Thus, using $m_a(L)\overline{\{\frac{\partial h}{\partial t}V(x,t)\}}_{x=L}$ to approximate $m_a(x)\overline{\frac{\partial h}{\partial t}V(x,t)}$ in (5.17), we have

$$\begin{aligned} \frac{\overline{P}}{U} &= -m_a(L)\overline{\left\{\frac{\partial h}{\partial t}V(x,t)\right\}}_{x=L}\int_0^L \frac{\partial}{\partial x}\left(\frac{2}{b_m^*}\right)\mathrm{d}x \\ &= -m_a(L)\overline{\left\{\frac{\partial h}{\partial t}V(x,t)\right\}}_{x=L}\frac{2}{b_m^*}\Big|_0^L \\ &= m_a(L)\overline{\left\{\frac{\partial h}{\partial t}V(x,t)\right\}}_{x=L}\frac{2}{1+\sqrt{1+AR^2/16}} \end{aligned} \tag{5.20}$$

Noting that the factor $\frac{2}{1+\sqrt{1+AR^2/16}}$ is equal to 1 when AR is small, the above expression reduces to

$$\frac{\overline{P}}{\overline{U}} = m_a(L)\overline{\left\{\frac{\partial h}{\partial t}V(x,t)\right\}}_{x=L}. \tag{5.21}$$

Injecting this expression into (5.18) yields the same mean thrust as Slender body potential flow model [46]. Now, it can be concluded that the mean thrust (5.19) depends on the lateral motion *near* the tailing edge rather than that only *at* the trailing edge, the result (5.9) is the limit case of (5.19) when AR tends to zero.

5.3 Conditions for maximum Froude efficiency

The efficiency of the fish swimming can be defined by the 'Froude efficiency'

$$\eta_F = \frac{\overline{F}_T U}{\overline{P}} = \frac{\overline{P} - \frac{1}{2}m_a(L)\overline{V^2(L,t)}U}{\overline{P}}. \tag{5.22}$$

It simply expresses the ratio of the mean thrust power to the rate of mechanical work done by the fish. For a fish with a specific geometry (described by $d(x)$ and $b(x)$) and moving with the lateral deflection $h^*(x,t)$, the sustained forward velocity U and the resulting lateral displacement $h(x,t)$ can be obtained by solving Eqs. (5.7 - 5.8). Then we can calculate the Froude efficiency. For a fish moving with the lateral deflection

$$h^*(x,t) = f(x)\cos(\omega t - \frac{x}{c}), \tag{5.23}$$

where c is the inverse of wave number. We assume that the lateral and angular recoil is zero (then, $h(x,t) = h^*(x,t)$), and the sustained swimming velocity is U. Now, to calculate the rate of total mechanical work done by the fish, we define

$$w(x,t) = m_a(x)\frac{\partial h}{\partial t}V(x,t). \tag{5.24}$$

Using a Taylor series to approximate the above expression, we obtain

$$w(x,t) = w(L,t) + \frac{\partial w}{\partial x}\Big|_{x=L}(x-L). \tag{5.25}$$

An injection of this implicit expression into (5.17) gives

$$\overline{P} = U\left\{\frac{4(\sqrt{16+A^2}-4)}{A^2}\frac{\omega(-U+c\omega)}{c}m_a(L)[f(L)]^2 \right.$$
$$\left. + \frac{A^3+(32-A^2)\sqrt{16+A^2}-128}{6A^2}\frac{L\omega(U-c\omega)}{2c}f(L)[2m_a(L)f'(L)+m_a'(L)f(L)]\right\}, \tag{5.26}$$

Expanding (5.26) about $A=0$ up to first order, we have

$$\overline{P} = U\frac{\omega(-U+c\omega)}{2c}\left\{m_a(L)[f(L)]^2 - \frac{Df(L)}{6}[2m_a(L)f'(L)+m_a'(L)f(L)]\right\} \tag{5.27}$$

The rate of the energy shed into the wake is

$$\frac{1}{2}m_a(L)\overline{V^2(L,t)}U = \frac{m_a(L)}{4c^2}U\{(U-c\omega)^2[f(L)]^2 + c^2U^2[f'(L)]^2\} \tag{5.28}$$

Now, it can be seen that a non-zero value of $f'(L)$ will increase the rate of energy shed into the wake without altering the rate of total mechanical work, since $f'(L)$ only appears in the second (minor) term of (5.27). Then, to achieve a maximum Froude efficiency, we assume that $f'(L) = 0$. Substituting the zeroth order term in (5.27) and (5.28) into (5.22), we have

$$\eta_F = \frac{1}{2}\left(1 + \frac{U}{c\omega}\right) \tag{5.29}$$

This result has already been found by Lighthill [46] for $\omega = 1$, and he pointed out that $c\omega$ must be bigger than U to generate a positive forward mean thrust.

Injecting the expressions (5.27) and (5.28) into (5.22), we obtain

$$\begin{aligned}\eta_F &= 1 - \frac{1}{2}\left(1 - \frac{U}{c\omega}\right)\frac{6m_a(L)}{6m_a(L) - Dm_a'(L)},\\ &= 1 - \frac{1}{2}\left(1 - \frac{U}{c\omega}\right)\frac{3d(L)}{3d(L) - Dd'(L)}.\end{aligned} \tag{5.30}$$

Now, we can see that the result (5.29) of Lighthill is only the zeroth order result, while the next order result is shown in (5.30). The ratio of energy shed into the wake to the total mechanical work is represented by the second term in (5.30), a positive value of this ratio requires

$$\begin{cases} U < c\omega, & d'(L) < 3d(L)/D \\ U > c\omega, & d'(L) > 3d(L)/D \end{cases} \tag{5.31}$$

and it must be smaller than 1

$$\frac{1}{2}\left(1 - \frac{U}{c\omega}\right)\frac{3d(L)}{3d(L) - Dd'(L)} < 1. \tag{5.32}$$

Usually, the height of caudal fin increases when approaching the trailing edge, but the slope is not too large. Thus, it is the first case in (5.31) that corresponds to the fish swimming in nature. To reach a high Froude efficiency, for example, $\eta_F = 0.9$, it needs that $c\omega = 1.25U$ from (5.29) [46]. This Froude efficiency can also be achieved by $c\omega = 1.2U$ and $d'(L) = 0.5d(L)/D$. The conditions (5.31,5.32) allow to model the fish swimming in a more general way.

The body width of anguilliform swimmers does not vary much along the body length. Thus, the condition $d'(L) = 0$ must be imposed for anguilliform swimmers. Together with the condition $f'(L) = 0$, the first order term in (5.27) is vanished, (5.30) then reduces to the zeroth order result (5.29). To find the Froude efficiency at next order in A^2, we perform the previous calculation (Eqs. 5.25 - 5.27, 5.30) with the terms up to second order. Assuming $d'(L) = 0$, $f'(L) = 0$, $d''(L) = 0$ and $f''(L) = 0$, the Froude efficiency for anguilliform swimmers can be obtained

$$\eta_F = 1 - \frac{1}{2}\left(1 - \frac{U}{c\omega}\right)\frac{64}{64 - A^2}. \tag{5.33}$$

From this expression, we can find that small aspect ratio makes η_F bigger. This maybe explain why the bodies of anguilliform swimmers are always so slender. Noting that the drag is not considered in present analysis, we then conclude that the morphology of anguilliform swimmers can be regarded as a compromise between the maximum thrust (requiring aspect ratio to be small) and minimum drag (requiring body shape to be streamlined).

An simple application of (5.19) in this section gives a more general and precise result about the fish swimming. This implies that a good fluid model (like the model introduced in section 3.1 and 3.3) gives more details about the force acting on the fish, and thus provides more parameters and aspects to describe and define the fish swimming. Note that this work is still in progress, more work need to be done to enrich the study of fish swimming.

Chapter 6

Conclusions and perspectives

6.1 Conclusions

In this thesis, we consider two fully-coupled fluid-structure interaction problems: the flapping flag instability and fish swimming. They can be both modeled as the interaction of a flexible plate and a high Reynolds number flow. The literature study shows that: originated from the general theory of oscillation wings, the 2D unsteady airfoil theory [77] can be applied to calculate the pressure load on a waving plate with large aspect ratio; while based on the concept of 'added mass', Slender-Body Theory[46] is widely used to calculate force exerted on a surface with small aspect ratio. These two theoretical model gives very good results in these perspective limit of aspect ratio, but can not accurately model the flow around a lifting surface with intermediate aspect ratio. Thus, the thesis aims to derive a theoretical model which can model the fluid around a surface with intermediate aspect ratio.

Based on the numerical lifting-surface method (panel method), a fixed-frequency lifting surface method is proposed by placing the body and wake vortices on the fixed reference plane, carefully defining the circulations of vorticity in the wake, and fulfilling the impermeability condition on the reference plane instead of the actual moving surface. This numerical method can be used to model the flow around a surface moving with small displacement. The advantage of this method is that the computation needs to be performed only one time, and it therefore reduces much computation costs. The numerical method shows a good convergence when the number of body vortices is large enough. Moreover, to compare with the theoretical results, the numerical method is applied to calculate the pressure difference across a rectangular surface imposed by the clamped-free lateral motion. Firstly, a slender surface with aspect ratio $A = 0.1$ is considered, the numerical computations are performed for various reduced frequency and different displacement mode. The contour figures of the circulation of vorticity and the pressure jump distribution across this slender surface are shown. The figures of the spanwise average of pressure jump shows a good agreement between the numerical results and the results of Slender-Body Theory. A Similar study is carried out for a large surface with aspect ratio $A = 10$, the good coincidences between the numerical results and the results of 2D unsteady airfoil theory are also found. The correctness of numerical method has been validated by all these comparisons. Since the fixed frequency lifting method has no specific constraints on the lifting surface geometry or the lateral displacement, it can be used to include the surface with an arbitrary geometry and an arbitrary small lateral displacement. Then, it will be used as the reference for the following studies.

In fact, the flow around a moving surface is governed by the Laplace equation with Neumann boundary condition. By means of Green function, the problem reduces to a Fredholm integral equation which relates the unknown potential jump to the downwash. The numerical solving has already been shown in the previous numerical study, and now we want to

use analytic techniques to solve this integral equation. Applying the Matched Asymptotic Expansion technique, the integral equation is approximated by an asymptotic series. The potential jump can be obtained using the Carleman inversion formula, and the pressure jump distribution can also be derived by applying the unsteady linearized Bernoulli law. The zeroth order result is equivalent to Slender-Body Theory, while the corrective first force make it possible to give more accurate results and include the surface with intermediate surface. However, by comparing with the numerical results, the analytic results does not seem satisfactory. Thus, a modified asymptotic solution by velocity potential (ASVP) is proposed by smoothing the divergence at the leading edge and satisfying the Kutta condition at the trailing edge. The good agreement between the numerical results and the results obtained from the modified asymptotic solution by velocity potential are found for a rectangular surface with the intermediate aspect ratio $A = 0.3$. The modified ASVP gives almost the same results as Slender-Body Theory in the anterior part of chord, but more accurate results in the posterior part of chord by fulfilling the Kutta condition at the trailing edge. Inspired by the asymptotic solving in this theoretical model, we re-formulate the problem in terms of acceleration potential, and propose a different approximation way to derive the asymptotic series of integral equation. By applying the Carleman inversion formula, the acceleration potential jump and corresponding forces are obtained. Noting the unsatisfied results given by this new model near the leading edge, the modified asymptotic solution by acceleration potential (ASAP) is therefore proposed. The results of the modified ASAP is similar to those of the modified ASVP (for the surface with aspect ratio $A = 0.3$), but the advantage is its simplicity and fulfillment of the Kutta condition at zeroth order. Although the modified ASAP is valid only for rectangular surfaces, it provides a new technique to solve Fredholm integral equation, to satisfy the Kutta condition, and consequently gives accurate pressure forces acting on a surface with intermediate aspect ratio.

To study the effect of aspect ratio on flapping flag instability, the modified asymptotic solution by acceleration potential is coupled with the linear fluid-structure model originally proposed by Eloy et al. [27]. For the plate with aspect ratio $A = 0.1$, the first five flutter modes obtained with the modified ASAP are similar to those obtained with Slender body theory, but the critical flow velocity is quantitatively different. This shows the importance of fluid model on the flag instability analysis. Moreover, the effect of aspect ratio on the critical flow velocity is studied for the plate with mass ratio $M^* = 1$, the result obtained with modified ASAP shows a very good agreement with the results of Eloy et al. [27] for $A < 0.7$. The decreasing trend implies that a plate with more slender span is more stable. Finally, the influence of mass ratio is studied for the plate with several aspect ratio ($A = 0.2$, $A = 0.9$, $A = 1$). It can be found that the critical flow velocity obtained with the modified ASAP coincides well to the results of Eloy et al. [27] for aspect ratio $A = 0.2$ and low mass ratio $M^* < 3$. Even for the plate of aspect ratio $A = 0.9$, the results obtained with the modified ASAP still seem quantitatively reasonable for low mass ratio $M^* < 1$. All above results validates the good applicability of the modified ASAP to the instability analysis of a plate, especially with intermediate aspect ratio.

A simple linear hydrodynamic model [46, 69] governing the motion of a swimming fish is first introduced. The resulting lateral motion and the sustained swimming speed can be obtained using this model. Comparing with Slender Body Theory [46], the modified ASAP is rewritten to include the lifting surface with variable span (instead of rectangular shape). Although this new formula may not be overwhelmingly convincing, the mean thrust derived from this formula seems logical, because the zeroth order term of this thrust is equivalent to the thrust obtained by Lighthill [46]. A further application of this new mean thrust gives a more general form of Froude efficiency whose zeroth order term also corresponds to the result of Lighthill [46]. The advantage of this new mean thrust is that the aspect ratio of fish is explicitly included, it thus allows to perform the optimization of fish swimming in terms of aspect ratio. Since this work is still in progress, more work need to be done to enrich the study of fish swimming with modified ASAP.

6.2 Perspectives

The main future work is obviously to implement numerically the modified asymptotic solution of acceleration potential in fish swimming, that is validating the correctness of the new thrust formula, then studying the effect of aspect ratio on the fish swimming.

Although the modified asymptotic solution of acceleration potential gives more accurate results, but the leading edge singularity is not included. Based on the new approximation technique in section 3.3, can leading edge effect can be included? does this technique can be generalized, or be applied in other situation.

The experimental results of Zhang et al. [80] show that the vortices exist all along a rigid filament of flag-like shape in Fig. 1.2e. This seems that for a given flow velocity, the flag will flap in a way that the least vortices are generated or the flow is the least disturbed (comparing to the incoming flow). If this conjecture is correct, the flapping flag instability problem can be modeled as an optimization problem (the flow should be least disturbed, or other optimal conditions). Maybe this could bring a new insight into this phenomenon.

Bibliography

[1] E. Albano and W. P. Rodden. A doublet-lattice method for calculating lift distributions on oscillating surfaces in subsonic flows. *AIAA journal*, 7(2):279–285, 1969.

[2] M. Alexandre, M. Alexander, and G. Goldspink. Swimming. *Mechanics and energetics of animal locomotion. New York: Wiley & Sons*, pages 222–254, 1977.

[3] J. Allen and A. Smits. Energy harvesting eel. *Journal of fluids and structures*, 15(3):629–640, 2001.

[4] M. Argentina and L. Mahadevan. Fluid-flow-induced flutter of a flag. *Proceedings of the National academy of Sciences of the United States of America*, 102(6):1829–1834, 2005.

[5] B. Audoly and Y. Pomeau. *Elasticity and geometry: from hair curls to the non-linear response of shells*. Oxford University Press, 2010.

[6] R. Bainbridge. The speed of swimming of fish as related to size and to the frequency and amplitude of the tail beat. *Journal of experimental biology*, 35(1):109–133, 1958.

[7] R. Bainbridge. Caudal fin and body movement in the propulsion of some fish. *Journal of Experimental Biology*, 40(1):23–56, 1963.

[8] R. W. Blake. *Fish locomotion*. Cambridge University Press, 1983.

[9] R. W. Blake. Fish functional design and swimming performance. *Journal of Fish Biology*, 65(5):1193–1222, 2004.

[10] R. D. Blevins. Flow-induced vibration. 1990.

[11] M. P. Brandao. Improper integrals in theoretical aerodynamics - The problem revisited. *AIAA Journal*, 25(9):1258–1260, sep 1987.

[12] C. Brennen. A review of added mass and fluid inertial forces. Technical report, DTIC Document, 1982.

[13] T. Carleman. *Sur la résolution de certaines équations intégrales*. Almqvist & Wiksells, 1922.

[14] J.-Y. Cheng, L.-X. Zhuang, and B.-G. Tong. Analysis of swimming three-dimensional waving plates. *Journal of Fluid Mechanics*, 232:341–355, 11 1991.

[15] F. Chouly, A. V. Hirtum, P.-Y. Lagrée, X. Pelorson, and Y. Payan. Numerical and experimental study of expiratory flow in the case of major upper airway obstructions with fluid–structure interaction. *Journal of Fluids and Structures*, 24(2):250 – 269, 2008.

[16] T. L. Daniel. Mechanics and energetics of medusan jet propulsion. *Canadian Journal of Zoology*, 61(6):1406–1420, 1983.

[17] S. Datta and W. Gottenberg. Instability of an elastic strip hanging in an airstream. *Journal of Applied Mechanics*, 42(1):195–198, 1975.

[18] E. De Langre, M. P. Païdoussis, O. Doaré, and Y. Modarres-Sadeghi. Flutter of long flexible cylinders in axial flow. *Journal of Fluid Mechanics*, 571:371–389, 1 2007.

[19] E. H. Dowell and K. C. Hall. Modeling of fluid-structure interaction. *Annual Review of Fluid Mechanics*, 33(1):445–490, 2001.

[20] G. Düring, C. Josserand, and S. Rica. Weak turbulence for a vibrating plate: Can one hear a kolmogorov spectrum? *Phys. Rev. Lett.*, 97:025503, Jul 2006.

[21] M. V. Dyke. *Perturbation methods in fluid mechanics*. The Parabolic Press, 1975.

[22] C. Eloy. On the best design for undulatory swimming. *Journal of Fluid Mechanics*, 717:48–89, 2013.

[23] C. Eloy, O. Doaré, L. Duchemin, and L. Schouveiler. A unified introduction to fluid mechanics of flying and swimming at high reynolds number. *Experimental Mechanics*, 50(9):1361–1366, 2010.

[24] C. Eloy, N. Kofman, and L. Schouveiler. The origin of hysteresis in the flag instability. *Journal of Fluid Mechanics*, 691:583–593, 2012.

[25] C. Eloy, R. Lagrange, C. Souilliez, and L. Schouveiler. Aeroelastic instability of cantilevered flexible plates in uniform flow. *Journal of Fluid Mechanics*, 611:97–106, 9 2008.

[26] C. Eloy and L. Schouveiler. Optimisation of two-dimensional undulatory swimming at high reynolds number. *International Journal of Non-Linear Mechanics*, 46(4):568 – 576, 2011. Special issue on non-linear mechanics of biological structures.

[27] C. Eloy, C. Souilliez, and L. Schouveiler. Flutter of a rectangular plate. *Journal of Fluids and Structures*, 23(6):904 – 919, 2007.

[28] R. Estrada and R. P. Kanwal. The carleman type singular integral equations. *SIAM Review*, 29(2):263–290, 1987.

[29] J. Gray. Studies in animal locomotion. *Journal of Experimental Biology*, 10(1):88–104, 1933.

[30] J. Gray. *Animal locomotion*. Weidenfeld & Nicolson London, 1968.

[31] L. Guermond, Jean. A systematic formula for the asymptotic expansion of singular integrals. *Zeitschrift für angewandte Mathematik und Physik ZAMP*, 38(5):717–729, 1987.

[32] C. Q. Guo and M. P. Paidoussis. Stability of rectangular plates with free side-edges in two-dimensional inviscid channel flow. *Journal of Applied Mechanics*, 67:171 – 176, 2000.

[33] J. Hadamard. *Lectures on Cauchy's problem in linear partial differential equations*. New Haven Yale University Press, 1923.

[34] L. Huang. Flutter of cantilevered plates in axial flow. *Journal of Fluids and Structures*, 9(2):127 – 147, 1995.

[35] R. P. Kanwal. *Linear Integral Equations: Theory and Technique*. Academic Press, 1971.

[36] J. Katz and A. Plotkin. *Low-speed aerodynamics*. Cambridge University Press, 2001.

[37] T. Kida and Y. Miyai. An alternative treatment of lifting-line theory as a perturbation problem. *Zeitschrift für angewandte Mathematik und Physik ZAMP*, 29(4):591–607, jul 1978.

[38] P. Konstadinopoulos, D. Thrasher, D. Mook, A. Nayfeh, and L. Watson. A vortex-lattice method for general, unsteady aerodynamics. *Journal of aircraft*, 22(1):43–49, 1985.

[39] A. Kornecki, E. Dowell, and J. O'brien. On the aeroelastic instability of two-dimensional panels in uniform incompressible flow. *Journal of Sound and Vibration*, 47(2):163–178, 1976.

[40] H. G. Küssner and I. Schwartz. The oscillating wing with aerodynamically balanced elevator. *Luftfahrtforschung*, 17(11/12):337–354, 1940. (English Translation: 1941, NACA TM 991).

[41] G. V. Lauder and E. D. Tytell. Hydrodynamics of undulatory propulsion. *Fish biomechanics*, 23:425–462, 2005.

[42] E. Lauga and T. R. Powers. The hydrodynamics of swimming microorganisms. *Reports on Progress in Physics*, 72(9):096601, 2009.

[43] C. Lemaitre, P. Hémon, and E. de Langre. Instability of a long ribbon hanging in axial air flow. *Journal of Fluids and Structures*, 20(7):913 – 925, 2005. Fluid-Plate InteractionsFluid-Plate Interactions.

[44] G.-j. Li, Z. Luodin, and X.-y. LU. Numerical studies on locomotion perfromance of fish-like tail fins. *Journal of Hydrodynamics, Ser. B*, 24(4):488–495, 2012.

[45] M. Lighthill. Hydromechanics of aquatic animal propulsion. *Annual review of fluid mechanics*, 1(1):413–446, 1969.

[46] M. J. Lighthill. Note on the swimming of slender fish. *Journal of Fluid Mechanics*, 9:305–317, 10 1960.

[47] M. J. Lighthill. Aquatic animal propulsion of high hydromechanical efficiency. *Journal of Fluid Mechanics*, 44:265–301, 11 1970.

[48] M. J. Lighthill. Large-amplitude elongated-body theory of fish locomotion. *Proceedings of the Royal Society of London B*, 179(1055):125–138, 1971.

[49] C. C. Lindsey. Form, function, and locomotory habits in fish. In *Fish Physiology*, volume 7. Academic Press, 1978.

[50] A. Lucey and P. Carpenter. The hydroelastic stability of three-dimensional disturbances of a finite compliant wall. *Journal of Sound and Vibration*, 165(3):527–552, 1993.

[51] K. Mangler. Improper integrals in theoretical aerodynamics. Technical report, British Aeronautical Research Council, 1951.

[52] S. Michelin and O. Doaré. Energy harvesting efficiency of piezoelectric flags in axial flows. *Journal of Fluid Mechanics*, 714:489–504, 2013.

[53] P. M. Morse and H. Feshbach. *Methods of theoretical physics*. McGraw-Hill, 1953.

[54] M. M. Munk. The aerodynamic forces on airship hulls. Technical Report NACA-TR-184, National Advisory Committee for Aeronautics; Washington, DC, United States, January 1924.

[55] M. M. Munk. Remarks on the pressure distribution over the surface of an ellipsoid, moving translationally through a perfect fluid. Technical Report NACA-TN-196, National Advisory Committee for Aeronautics; Washington, DC, United States, January 1924.

[56] M. P. Paidoussis. *Fluid-Structure Interactions: Slender Structures and Axial Flow*, volume 1. Academic press, 1998.

[57] M. P. Paidoussis. *Fluid-Structure Interactions: Slender Structures and Axial Flow*, volume 2. Academic Press, 2004.

[58] M. P. Païdoussis, S. J. Price, and E. De Langre. *Fluid-structure interactions: cross-flow-induced instabilities*. Cambridge University Press, 2010.

[59] W. P. Rodden, P. F. Taylor, and S. C. McIntosh. Further refinement of the subsonic doublet-lattice method. *Journal of Aircraft*, 35(5):720–727, 1998.

[60] M. Sfakiotakis, D. M. Lane, and J. B. C. Davies. Review of fish swimming modes for aquatic locomotion. *Oceanic Engineering, IEEE Journal of*, 24(2):237–252, 1999.

[61] L. Shayo. The stability of cantilever panels in uniform incompressible flow. *Journal of Sound and Vibration*, 68(3):341–350, 1980.

[62] M. Shelley, N. Vandenberghe, and J. Zhang. Heavy flags undergo spontaneous oscillations in flowing water. *Physical review letters*, 94(9):094302, 2005.

[63] M. J. Shelley and J. Zhang. Flapping and bending bodies interacting with fluid flows. *Annual Review of Fluid Mechanics*, 43:449–465, 2011.

[64] L. Shen, X. Zhang, D. K. Yue, and M. S. Triantafyllou. Turbulent flow over a flexible wall undergoing a streamwise travelling wave motion. *Journal of Fluid Mechanics*, 484:197–221, 2003.

[65] K. Singh, S. Michelin, and E. De Langre. Energy harvesting from axial fluid-elastic instabilities of a cylinder. *Journal of Fluids and Structures*, 30:159–172, 2012.

[66] C. Souilliez, C. Eloy, and L. Schouveiler. An experimental study of flag flutter. In *ASME 2006 Pressure Vessels and Piping/ICPVT-11 Conference*, pages 465–472. American Society of Mechanical Engineers, 2006.

[67] S. Taneda. Waving motions of flags. *Journal of the Physical Society of Japan*, 24(2):392–401, 1968.

[68] T. Theodorsen and W. Mutchler. General theory of aerodynamic instability and the mechanism of flutter. Technical Report NACA-TR-496, National Advisory Committee for Aeronautics Hampton, 1935.

[69] G. Tokić and D. K. P. Yue. Optimal shape and motion of undulatory swimming organisms. *Proceedings of the Royal Society of London B: Biological Sciences*, 279(1740):3065–3074, 2012.

[70] M. Triantafyllou, G. Triantafyllou, and D. Yue. Hydrodynamics of fishlike swimming. *Annual review of fluid mechanics*, 32(1):33–53, 2000.

[71] E. O. Tuck. Some accurate solutions of the lifting surface integral equation. *The ANZIAM Journal*, 35:127–144, 10 1993.

[72] J. F. van Weerden, D. A. P. Reid, and C. K. Hemelrijk. A meta-analysis of steady undulatory swimming. *Fish and Fisheries*, 15(3):397–409, 2014.

[73] J. J. Videler. *Fish swimming*, volume 10. Chapman & Hall, 1993.

[74] Y. Watanabe, S. Suzuki, M. Sugihara, and Y. Sueoka. An experimental study of paper flutter. *Journal of Fluids and Structures*, 16(4):529–542, 2002.

[75] P. W. Webb et al. *Hydrodynamics and energetics of fish propulsion.* Dept. of the Environment, Fisheries and Marine Service, 1975.

[76] T. Y. Wu. Fish swimming and bird/insect flight. *Annual Review of Fluid Mechanics*, 43:25–58, 2011.

[77] T. Y.-T. Wu. Swimming of a waving plate. *Journal of Fluid Mechanics*, 10:321–344, 5 1961.

[78] N. Yamaguchi, T. Sekiguchi, K. Yokota, and Y. Tsujimoto. Flutter limits and behavior of a flexible thin sheet in high-speed flow—ii: experimental results and predicted behaviors for low mass ratios. *Journal of fluids engineering*, 122(1):74–83, 2000.

[79] T. S. Yu, E. Lauga, and A. E. Hosoi. Experimental investigations of elastic tail propulsion at low reynolds number. *Physics of Fluids*, 18(9), 2006.

[80] J. Zhang, S. Childress, A. Libchaber, and M. Shelley. Flexible filaments in a flowing soap film as a model for one-dimensional flags in a two-dimensional wind. *Nature*, 408(6814):835–839, 2000.